Spectroscopic investigations of photon-induced reactions in tin-oxo cage photoresists

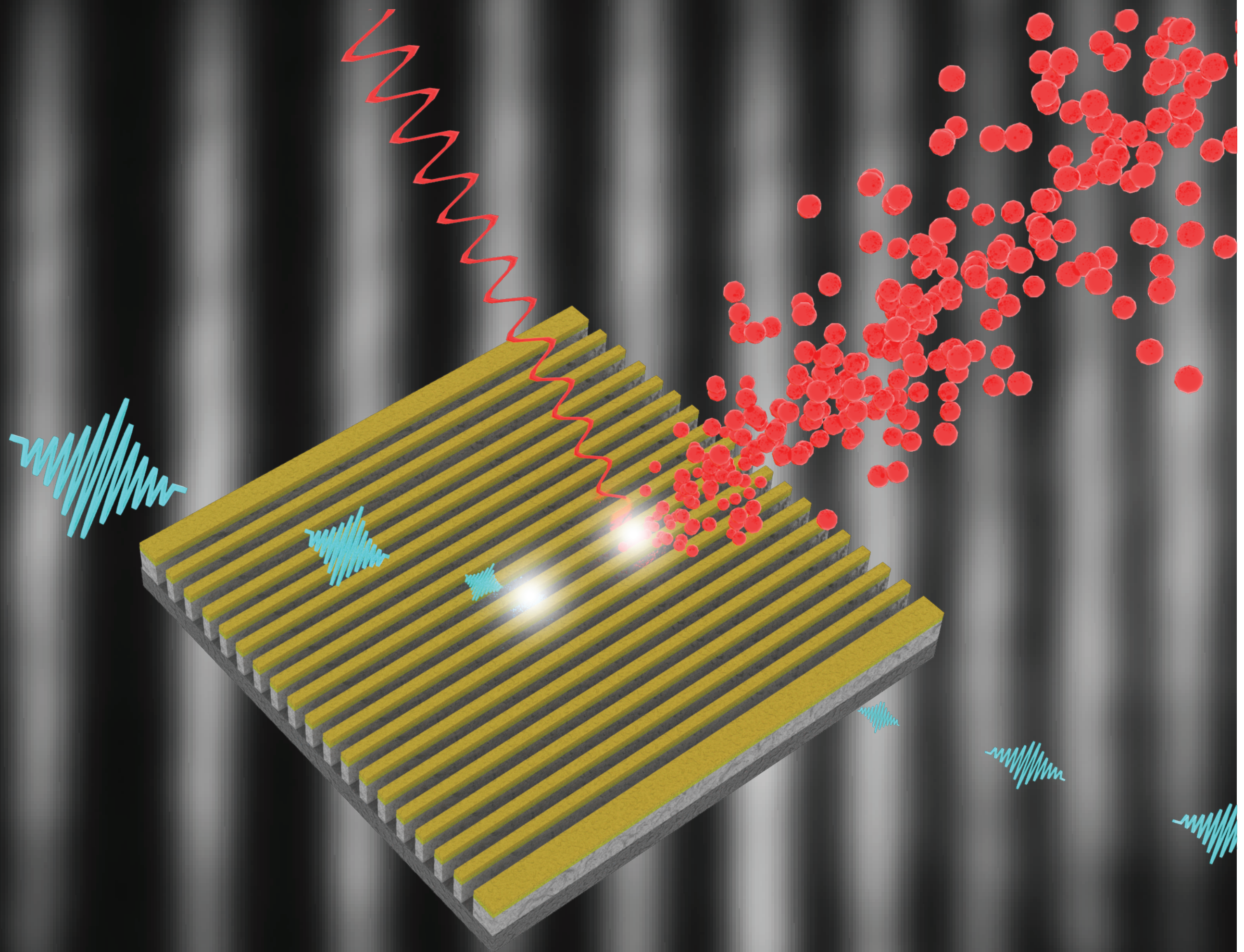

Najmeh Sadegh

Spectroscopic investigations of photon-induced reactions in tin-oxo cage photoresists

Cover design by: Ricardo Struik

ISBN: 978-94-6419-906-2

Full color version of this thesis and the electronic supplementary information are available at: http://dare.uva.nl/en

Printed by: Gildeprint

Spectroscopic investigations of photon-induced reactions in tin-oxo cage photoresists

ACADEMISCH PROEFSCHRIFT

ter verkrijging van de graad van doctor
aan de Universiteit van Amsterdam
op gezag van de Rector Magnificus
prof. dr. ir. P.P.C.C. Verbeek
ten overstaan van een door het College voor Promoties ingestelde commissie,
in het openbaar te verdedigen in de Agnietenkapel
op woensdag 20 september 2023, te 16.00 uur

door Najmeh Sadegh

geboren te Shiraz

Promotiecommissie

Promotor:

prof. dr. A.M. Brouwer	*Universiteit van Amsterdam*

Copromotor:

dr. P.M. Kraus	*Vrije Universiteit Amsterdam*

Overige leden:

prof. dr. W.J. Buma	*Universiteit van Amsterdam*
prof. dr. J.W.M. Frenken	*Universiteit van Amsterdam*
prof. dr. O. Ingólfsson	*University of Iceland*
dr. R. Bliem	*Universiteit van Amsterdam*
dr. S. Castellanos Ortega	*Inpria*

Faculteit der Natuurwetenschappen, Wiskunde en Informatica
Van 't Hoff Institute for Molecular Sciences
Advanced Research Center for Nanolithography (ARCNL)

The research described in this thesis was carried out at the Advanced Research Center for Nanolithography (ARCNL), a public-private partnership of University of Amsterdam (UvA), the Dutch Research Council (NWO) and the semiconductor equipment manufacturer ASML.

This project contributes to the ELENA (Low energy ELEctron driven chemistry for the advantage of emerging NAno-fabrication method) European training network and it has received funding from the European Union’s Horizon 2020 research and Innovation program under the Marie Skłodowska- Curie grant agreement No 722149.

Contents

1 Introduction 1

1.1 EUV lithography 4

1.2 EUV photoresists 6

1.3 Tin containing EUV photoresist 11

1.4 High-harmonic generation 14

1.4.1 Microscopic picture of high-harmonic generation 14

1.4.2 Phase matching conditions 18

1.5 Aims and outline of this thesis 20

2 Experimental setups and methods 23

2.1 High-harmonic absorption spectroscopy 24

2.1.1 Experimental setup for high-harmonic generation and extreme-ultraviolet absorption measurements 24

2.1.2 XUV induced bleaching measurements 28

2.1.3 Methodology for performing measurements 29

2.1.4 Data processing 30

2.1.5 CCD calibration 32

2.2 X-ray photoemission spectroscopy of EUV photoresists 38

2.2.1 Total Electron Yield: Theory and definition 38

2.2.2 X-Ray Photoelectron Spectroscopy: Theory and definition 39

2.2.3 TEY and XPS instrumentation 41

2.2.4 TEY experiments 44

2.3 Ellipsometry 50

3 XUV induced bleaching of a tin-oxo cage photoresist studied by high harmonic absorption spectroscopy 57

3.1 Introduction 58

3.2 Experimental 59

3.2.1 Sample preparation 59

3.2.2 Experimental set-up and methodology 59

3.3 Results 60

3.4 Discussion 62

3.5 Conclusion 66

4 High harmonic absorption spectroscopy of tin-oxo cage acetate with XUV photons up to 70 eV 67

4.1 Introduction 68

4.2 Results 69
4.2.1 Tin-oxo cage absorption spectra in XUV energy range 69
4.2.2 XUV induced bleaching of tin-oxo cage acetate 71
4.3 Discussion 75
4.3.1 XUV absorption spectra of tin-oxo cage acetate 75
4.3.2 XUV induced photobleaching 76
4.3.3 XUV versus EUV Dill parameters 77
4.4 Conclusion 79
5 Soft X-ray photoelectron spectroscopy of tin-oxo cage EUV photoresists 81
5.1 Introduction 82
5.2 Results 84
5.2.1 TEY measurement on Si 84
5.2.2 TEY measurement on Au 86
5.2.3 TEY measurement on tin-oxo cages 89
5.2.4 Total electron yield evolution with exposure 91
5.3 X-ray photoelectron spectroscopy of tin-oxo cage 93
5.4 Discussion 97
5.5 Conclusion 99
6 Photoconversion of tin-oxo cages at 92 eV 101
6.1 Introduction 102
6.2 Materials and methodologies 103
6.2.1 Sample preparation 103
6.2.2 RGA measurements: methodology and instrumentation 103
6.3 Results 107
6.3.1 Mass spectrometry of the tin-oxo cage outgassing products 107
6.3.2 Fast acquisition RGA of selected outgassing materials 111
6.3.3 Film thickness evolution as a function of exposure dose 113
6.4 Discussion 116
6.5 Conclusion 119
References 121
Summary 135
Samenvatting 139
Publication list 143
Acknowledgement 145

Chapter 1

Introduction

Throughout the evolution of IC manufacturing industry over the past decades, photolithography has been the key technology for the fabrication of transistors and microchips [1-4]. The lithography process includes several steps, shown in Figure 1.1, to image the patterns from a photomask to a semiconductor layer such as silicon. A photosensitive material, known as a photoresist, is used to transfer the radiation pattern into a physical pattern on the substrate. The work described in this thesis is focused on the physics and chemistry of the first step of the photolithography process: the radiation induced change in the properties of a photoresist film.

In the first step of IC manufacturing, the photoresist is spin-coated to form a thin film (typically tens of nanometers) on top of the semiconductor layer. Then, soft baking is applied to the resist to solidify the resist's film and remove the residual solvents. The light pattern created by the photomask is used to locally expose the photoresist. The absorbed photons drive chemical changes in the resists. When the resist becomes insoluble due to these chemical reactions, the resist is called negative tone. In contrast, a photoresist of positive tone can be washed away through the development step, while the unexposed layer stays behind. Therefore, the solubility switch of the resist plays a crucial role in transferring the pattern to the substrate. After quality inspection of the patterns, the pattern on the resists needs to be transferred to the silicon substrate. This is achieved through the etching process (mainly chemical or plasma), during which the resist protects the area below it against etching. Finally, the resist is stripped away, and in this way, it leaves a pattern on the semiconductor substrate. For designing a chip on a silicon wafer, the described lithography process is repeated many times to make a 3D structure by building layers on top of each other [4-6].

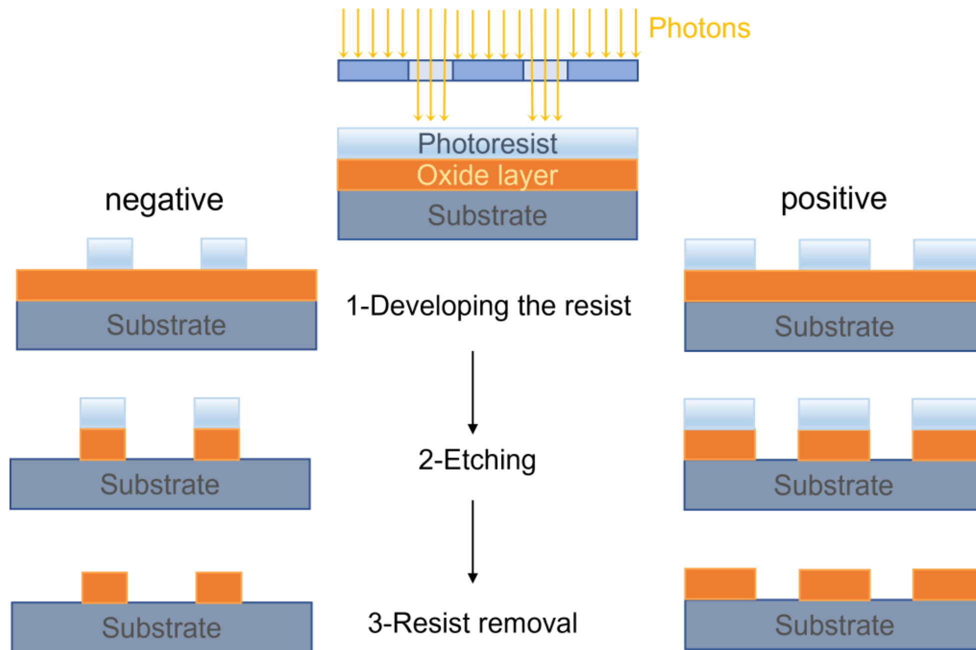

Figure 1.1. Schematic presentation of main steps in the photolithography process (source of graph: ASML).

One key parameter in the performance of the lithography process is the resolution of the pattern. This is defined as the minimum feature's dimension printed on the substrate and it is called critical dimension (CD) in the lithography community.

In imaging lithography, the light pattern on the mask is projected on the resist surface while it is scaled down to a few nm on the resist surface by a set of imaging optics in the exposure system.

In an optical projection system, the resolution or CD can be estimated using equation (1.1), which is directly linked to Abbe diffraction limit:

$$CD = k_1 \frac{\lambda}{NA} \tag{1.1}$$

λ is the wavelength of the used light, and *NA* is the numerical aperture of the focusing optic as can be seen from the sample surface. k_1 depends on the imaging processes to enhance the resolution and cannot be reduced below 0.25 in practice in a single exposure lithographic process step. Working close to this limit requires very elaborate resolution enhancement techniques. In immersion lithography, a liquid with a refractive index $n > 1$ is used to fill the air space between the last optical focusing element and the surface of the resist. This increases the acceptance angle of the optical element, and the optical element can accommodate optical rays at higher spatial frequencies, which permits the printing of smaller features [7,

8]. By coupling water in the 193i DUV (ArFi) lithography scanners, *NA* values up to 1.35 are now in operation [9-11].

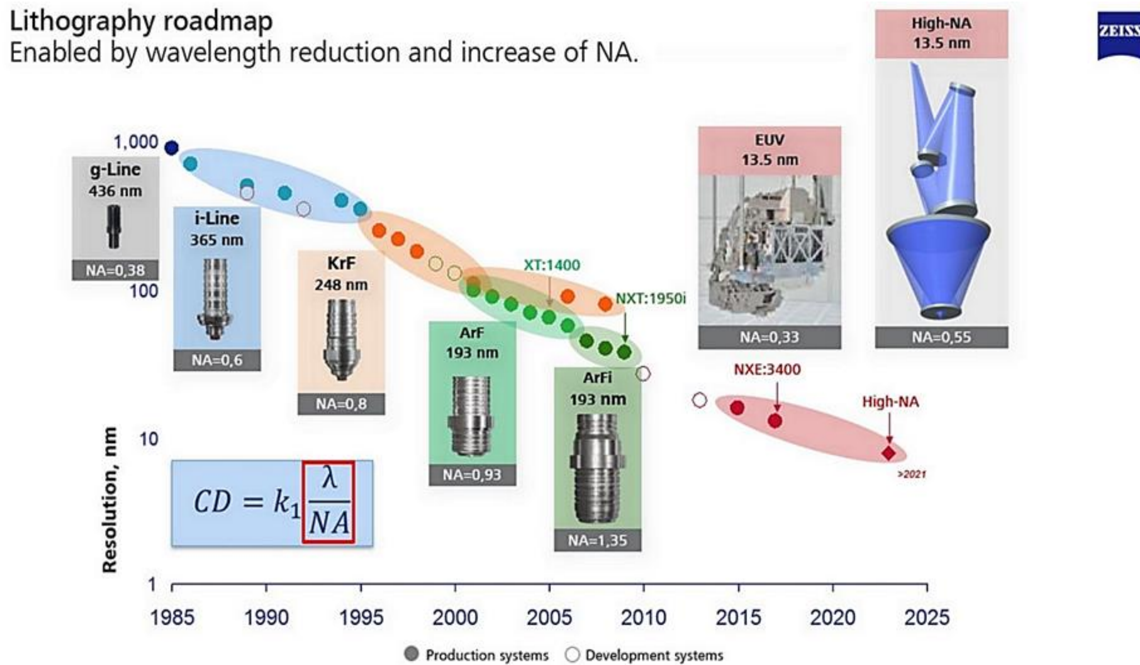

Figure 1.2. This figure shows the roadmap of the main changes in the lithography scanners' history achieved by shrinking the source light's wavelength. ArFi lithography was developed as the extension of ArF scanners based on immersion lithography. The picture is courtesy of ZEISS [12].

So far, the greatest breakthroughs in the lithography industry have occurred by reducing the wavelength of the incident light to increase the resolution of the features. The roadmap in Figure 1.2 summarizes the result of this strive for some of the produced scanners [12]. Different spectral lines of the mercury (Hg) lamp such as g-line (436 nm), h-line (405 nm), and i-line (365) were used in lithography until 1990. Then the development of KrF laser-based systems (248 nm) enabled writing features down to 250 nm. The resolution came down to 65 nm by the integration of the ArF lasers (193 nm) into Deep UV scanners.

After 193 nm lithography reached its physical limit (~35 nm CD), multi-patterning techniques were applied to allow the DUV lithography to produce features below 20 nm. The patterns are transferred to the substrate one by one in sequential exposures. Although the 193 nm lithography frontiers can be pushed to sub10 nm nodes [13-15] using multiple patterning, this technique takes a lot more processing steps that reduces the number of wafers printable in a given time, and therefore, the industry has been on the quest for other viable solutions.

In the early 2000's, the first generations of the Extreme UltraViolet scanners were developed by ASML as the most up to date solution to enable further shrinkage of transistors and increase the density in microchips further. EUV lithography uses 13.5 nm wavelength light as the patterning wavelength, and so far, ASML has been the only manufacturer of this technology [3, 16, 17].

1.1 EUV lithography

Early research on EUV lithography took place in the 1980s using soft-X-ray light in the range of 4 to 40 nm. Later the development of multilayer coating optics for the reflection of soft X-ray beams opened up the path for the investigation of optical projection lithography at such short wavelengths. Later in 1993, (soft) X-ray projection lithography explicitly changed its name to EUVL lithography [3]. Over time, practical limitations such as the bandwidth of the multilayer coatings, source throughput, resolution, depth of focus and resist performance narrowed down the range of the applicable exposure wavelength, and finally, the EUV lithography scanners were implemented at 13.5 nm [3, 18]. Nowadays, one of the latest versions of ASML NXT scanners (NXE:3400C) can support high-volume manufacturing of 7 and 5 nm logic nodes with 170 (300-mm) wafers per hour at a dose of 20 mJ cm^{-2} [19].

In the current commercially used DUV lithography systems, the lithography source is based on laser systems, for example, excimer lasers such as KrF for 248 nm and ArF for 193 nm DUV lithography. But the EUV light is generated through a laser-produced plasma (LPP), driven by a CO2 laser at 10.6 μm. A schematic of the exposure system inside one of the ASML EUV lithography machines is shown in Figure 1.3. In a LPP, a high-power pulsed CO2 laser is focused on a stream of molten tin droplets at the foci of the elliptical mirror. EUV light is generated by a sequence of two pulses. A first less intense pre-pulse deforms the droplet to a flat sheet, reminiscent of a pizza, and a second more intense pulse (the main pulse) then stimulates the production of a LPP that emits EUV. The intense electric field of the main pulse creates a highly ionized and dense tin plasma, which emits a range of wavelengths, including 13.5 nm. The elliptical mirror is known as the collector. This mirror has a silicon/molybdenum multilayer coating which collects a portion of narrow bandwidth light around 13.5 nm selectively and refocuses the light at the other (the further focal point) of the collector [20-22]. Light generation, beam delivery, and exposure are all performed inside vacuum since the 13.5 nm beam is highly absorbed in ambient air. The beam is directed and imaged on the resists using multilayer reflective aspheric mirrors (Bragg reflectors) to avoid light loss

inside the material, while the imaging in DUV lithography scanners is done using refractive optics such as optical lenses.

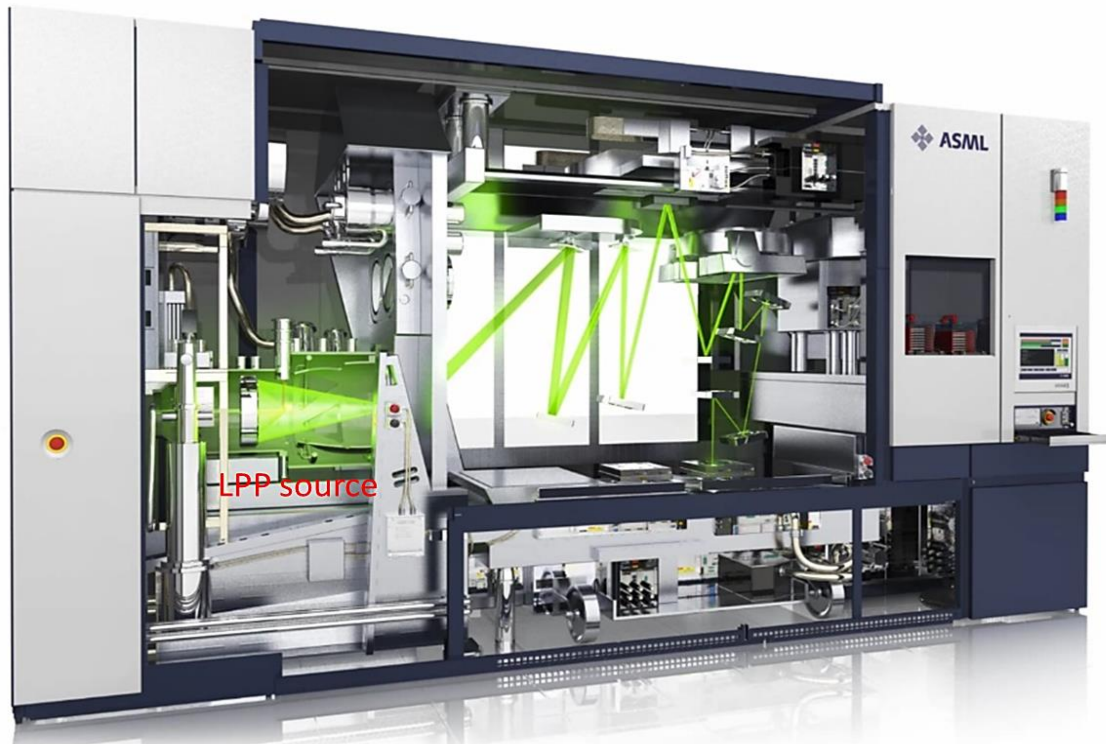

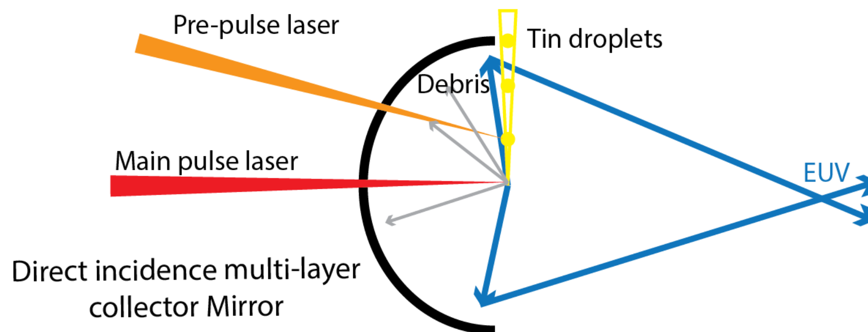

Figure 1.3. Top figure: a view from the EUV ASML scanner containing the LPP source and the imaging system with 10 reflective optics (courtesy of ASML). Bottom figure: schematic presentation of the LPP inside the collector [23].

The reduction of wavelength from 193 nm to 13.5 nm provides a higher imaging resolution. For a given CD, EUV can work with a smaller *NA* (initially 0.25) and, therefore, a larger depth of focus [5, 24]. For printing a sub 20 nm feature, the smaller *NA* alleviates the need for projection optics with hyper *NA* (>1) in DUV lithography, and the larger depth of focus allows using thicker photoresist films. But for putting a EUV scanner into the commercial application, increase of *NA* will provide higher spatial

resolution at the expense of depth of focus. Many challenges must be addressed, on the instrumental side, but also on the photoresist, which will need to be applied in even thinner films.

For example, the short wavelength of 13.5 nm requires the use of multiple mirrors inside the EUV scanner to achieve the required imaging magnification on the resist surface. Therefore, the loss of EUV photons in each reflection from the multilayer mirrors creates the necessity for a high power EUV source that could economically deliver sufficient throughput for high-volume production. The reliability of the source to operate stably, in the long run, is also challenging since the generated debris, and tin droplets on the collector mirror reduce the lifetime of the source [25-27]. In 2017, ASML sent out NXE:3400B generation of its EUV scanners with sources that could reach 200-250 W (upgradeable to 300 W), supporting the throughput of 125 wafers per hour [28, 29].

Another complexity in EUV scanners is the shadowing effects caused by the off-axis illumination of the mask since the mask must be used in reflective mode [30, 31].

The metrology systems and inspection tools need to work at a better resolution than the printed features. The extreme short wavelength imposes high-quality criteria on the design of surfaces and layers; EUV light reflection from a multilayer mirror is the sum of all reflections from each interface inside that mirror. Therefore, any buried defects inside the multilayer coating and surface roughness can shift the wavefront and amplitude of the EUV light, deteriorating the imaging quality, and high-resolution inspection tools are required to detect such microscopic scale buried defects [32, 33].

As discussed above, there is a prerequisite for having high-power sources for EUV light due to EUV photon losses. On the other side, a minimum dose (usually expressed as mJ cm^{-2}) of impinging photons is needed to initiate the solubility switch in the photoresists. But for a particular dose value, approximately 14 times fewer EUV photons are available than 193 nm-photons due to the higher energy per photon. Therefore, the switch to EUV radiation demands a new generation of resists with higher sensitivity and absorption than the traditional DUV resists.

1.2 EUV photoresists

Photoresist performance is evaluated based on three parameters abbreviated as RLS: resolution, line edge roughness (LER), and sensitivity. These parameters are correlated, and usually, the improvement of two of these factors comes at the expense of the other, the so-called the RLS trade-off [34, 35].

The resist sensitivity is defined as the minimum required energy to render a well-defined feature on the photoresists. The resist sensitivity is approximately proportional to throughout of a lithography machine and is measured in mJ cm^{-2}. Line edge (width) roughness is the variation in the width of a printed feature from a straight line [34-36].

To understand the developments of EUV photoresists, first we need to obtain a generic view on the reaction mechanism of chemically amplified resists (CARs) as the most common class of photoresists in DUV lithography. A typical CAR resist is composed of two main parts: a polymer matrix, a photoacid generator (PAG) as the active photo site of the resist, and sometimes a CAR contains a (photo-destroyable) quencher.

The polymer (such as polyhydroxystyrene (PHS) in 248 nm lithography) is soluble in the developer (ammonium hydroxide in water) due to the weakly acidic hydroxyl groups. Some hydroxyl sites (usually 20 %) are blocked by adding hydrophobic groups called inhibitors (such as t-butoxycarbonyl group (t-BOC)) as they inhibit the dissolution of the polymer in positive resists. In negative tone resist crosslinking agents are used instead of inhibitors [4, 37]. The aromatic poly(hydroxystyrene) (PHS) resists strongly absorb at 193 nm, not allowing the light to penetrate the entire film. This required the switch to more transparent polymer backbones such as methacrylates [37, 38] (Figure 1.4).

a) tBOC protected PHS

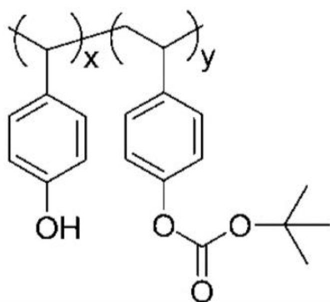

b) Methacrylate

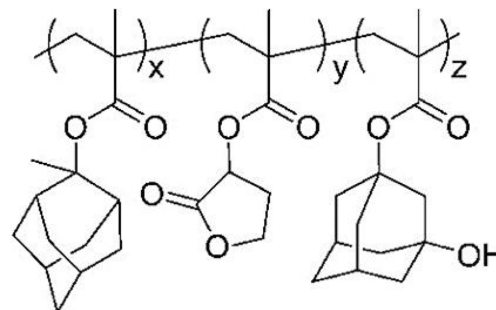

Figure 1.4. Example of a typical chemically amplified positive-tone photoresists for DUV lithography. a) for 248 nm platform, b) for 193 nm platform.

The PAG generates acid after exposure to DUV light which deblocks (deprotects) the polymer. The acid catalyzes the deprotection of multiple dissolution inhibitors during the post-exposure baking. The extent of this chemical amplification needs to be controlled since the diffusion of the acid into the unexposed part of the resist can lead to higher LER and reduced resolution. Therefore, a balance between sensitivity and resolution is required for optimum resist performance. Sometimes base quenchers are

added to improve the LER and the contrast; their function is to neutralize low levels of acid that might diffuse into the unexposed parts [4, 6].

The introduction of the EUV-lithography technique in the semiconductor industry has pushed the research community to either improve the properties of the traditional CARs or to find a new generation of resist with enhanced LSR at EUV wavelength. For example, one related concern is the development of resists with high sensitivity and absorption at EUV wavelength to compensate for the lower photon flux of the EUV light source, while in DUV lithography, the abundance of photons gives more room for improvement of the other two LSR parameters [39, 40]. The current target for the sensitivity of EUV resists is around 15 $mJ\ cm^{-2}$, and the desired LER for patterns below 20 nm is ~1-2 nm and below, depending on the feature size [41].

Since the EUV photons are very energetic, they initiate reaction mechanisms inside resists that differ from those caused by DUV photons. The energy of 92 eV photons is well above the ionization threshold of the valence electrons of molecules, and depending on the elements present, also the highest core energy levels can be excited. In this energy range the absorption properties of the resist are related to the atomic composition rather than to its molecular properties. The ionization of the core and valence electrons in the resist leads to the formation of photoelectrons with kinetic energies that are high enough to cause further ionization and generation of low energy electrons. The holes and electrons initiate reactions that lead to dissociation of chemical bonds in the resists. Hence, understanding the low-energy electrons plays a significant role in designing efficient EUV resists. However, since the emitted photoelectrons contain a broad kinetic energy distribution, they can lead to different reaction pathways in the resist [39].This has made understanding the induced chemical events complicated, and little information is so far at hand.

Traditional DUV CARs consist mainly of carbon, oxygen, and hydrogen, which are not the most absorbing elements for 13.5 nm. Therefore, to increase the sensitivity of the traditional CARs, one needs to increase the electron yield of the resist which means the number of generated electrons per absorbed EUV photon. The low-energy electrons convert the PAG to acids for deprotection of the polymer matrix.

One way that scientists used to improve this class of resists was to enhance their electron yield by increasing the ratio of oxygen and nitrogen to carbon due to the higher absorption cross-section of oxygen at EUV wavelength. Adding halogens to the composition of the conventional resists was another strategy. One study in Imec measured the total electron yield of F and I- sensitizers used in the polymer and PAG of the resists. The iodinated compounds showed higher electron yield and on a level comparable with

some metal based resists (structures not disclosed) [42] due to the EUV photons exciting electrons from the 4d orbitals at 92 eV. Also, fluorinated PAGs such as fluorinated aryl sulfonates were introduced [43, 44].

The quest for better resolution and lower LER at 13.5 nm-based lithography, diverts the attention to using molecular resists with small molecular sizes and more isotropic structures to increase the resolution and bring down the LER. As an example of organic EUV molecular resists, we can point to the synthesis of MGR110P molecular resists by Echigo et al.[45], Noria molecules with different moieties in Kudo's work [46, 47], and various low-molecular-weight molecular glass resists with calixarene cores developed by Dow electronics [48].

So far, one of the most promising approaches with most embedded novelties has been the development of inorganic EUV resists with the incorporation of metals in the resist structures such as Sn, Hf, Zn, In, Ti, and Zr that provide a high absorption cross-section at EUV wavelength (Figure 1.5). In this direction, various hybrid systems have been synthesized using metal oxide nanoparticles and molecular oxo cages using metals or semi-metals with relatively many electrons in high-lying core orbitals to enhance the cross sections in the EUV [49, 50]. Nevertheless, most research in this area focuses on demonstrating the patterning capabilities of their designed resist at EUV wavelength, with little information disclosed about the resist's structure.

Metal oxo clusters have a core-shell structure; the metal oxide core usually guarantees a high electron yield, and the organic shell is responsible for the radiation solubility switch. They usually hold a well-defined structure which is considered a favorable aspect when comparing with nanoparticle resists. The latter are produced through sol-gel reactions, which can lead to a distribution of different sizes and shapes [51, 52].

Ober et al. worked on developing the metal oxide nanoparticles ZrO_2 and HfO_2 with different organic ligands with controlled nanoparticle size below 3 nm in favor of the higher resolution. They showed high sensitivity below 5 mJ cm^{-2}, high etch, and chemical stability but roughness was poor. They also published the line patterns of 26 nm spacing using ZrMAA (zirconium oxide nanoparticle stabilized with methacrylic acid ligands) photoresists with a PAG additive.

Li and his group studied the effect of three different acid-based organic ligands on the sensitivity and LER of the Hf-based hybrid photoresist and the induced change in nanoparticle size during exposure and its subsequent influence on the solubility and patterning properties of the resists [53].

Passarelli et al. introduced organometallic carboxylate compounds incorporating antimony, bismuth, tin, and tellurium, and amongst them, the highest sensitivity was reported for antimony-containing resists [54].

Inpria corporation was the first to develop a commercial EUV inorganic resist. Their Y-series metal oxide photoresists (structure not disclosed) achieved 13 nm half-pitch at 35 mJ cm^{-2} using the NXE:3300B ASML scanners and 11 nm half-pitch with 1.7 nm LER in EUV interference lithography. The resists have a high etch resistance and absorbance (~20 μm^{-1}) with reduced photon shot noise [55].

An extensive part of the photoresist-oriented research tries to elucidate the complicated reaction pathways leading to the solubility switch of the resist using various techniques. Bypassing this complexity, Hinsberg and Meyers put forward a basic model from the reactivity of the negative tone inorganic resist, which includes two main steps: activation and condensation. Cleavage of what they call the ligands leads to the formation of active sites. These active sites form metal-oxo bonds in the condensation step creating a network structure that renders the material insoluble [56].

Ti-Zr-Hf- molecular oxo clusters with methacrylate (MA) ligands were used by Castellanos and her team as EUV photoresists. They provide more insight into these compounds' photoreactivity using FTIR, UV-vis and photoelectron spectroscopy. A cationic form of the oxo cluster is formed as a result of ionization with photoelectrons leading to the crosslinking of the MA ligands in the resist upon EUV irradiation [10, 51].

In another work from Castellanos’s team a Zn-based metal oxo cluster (Zn(MA)(TFA)) was developed with a denser metal oxo core. Besides the methacrylate ligands, Trifluoroacetate (TFA) was added to the organic shell to enhance the absorption of the resist. They printed features of 30 nm with a sensitivity of 20 mJ cm^{-2} and LER < 3 nm and based on their results they suggested a reaction model for the resist [57, 58].

Considering all the efforts to increase the sensitivity of the resist due to the limitation of EUV photons, we should keep in mind that high levels of secondary electron yield are not always favourable. Electrons with low kinetic energy have a relatively long mean free path. They can travel several nanometers inside the resist before ultimately losing their energy. The electron diffusion would degrade the aerial image (known as secondary electron blur) and result in high LER and added roughness due to electron stochastics [59, 60]. Accordingly, the resist's functionality can be optimized only with controlled yields of electrons

and the reaction kinetics, which gets increasingly important as the logic node size shrinks to sub 10 nm, putting extra weight on the significance of comprehending the photo electron-induced reactions.

1.3 Tin containing EUV photoresist

Molecular inorganic photoresists are now the top candidates for EUV photoresists due to the high absorption of metallic elements at EUV wavelength, higher etch resistance, and a well-defined structure.

Amongst this class of resists, most research has been devoted to the tin-based EUV resist, as they have been considered most attractive for industrial application. For example, Inpria has published several patents on tin-based resists for the EUV integration market [61-63].

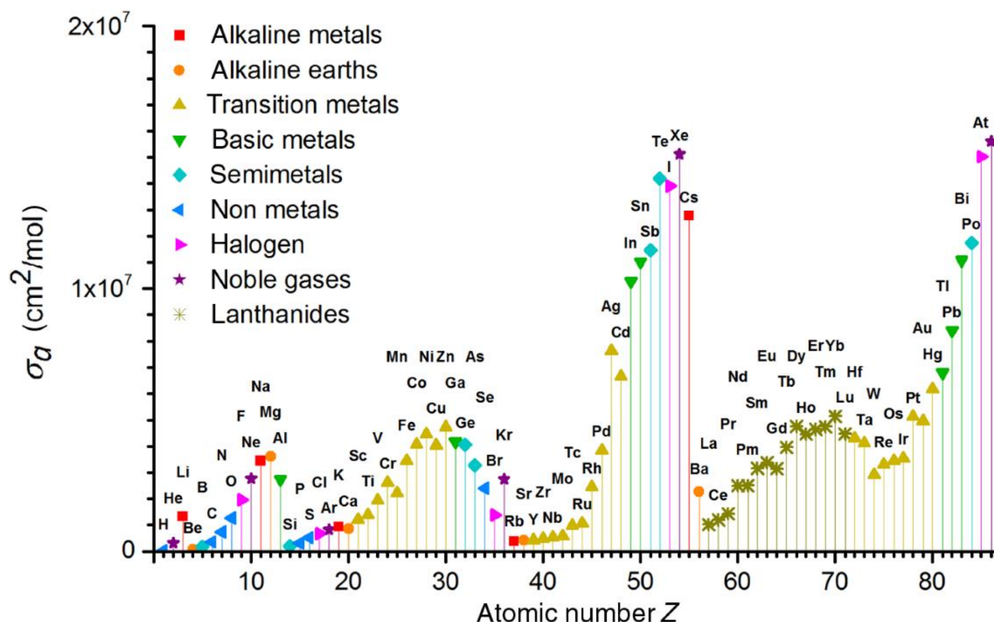

Figure 1.5. Atomic absorption cross-sections of elements with atomic number z=1 to 86 at 13.5 nm. The graph is taken from ref [64].

Tin provides a higher EUV cross-section than many other elements (Figure 1.5). The tin-based resists containing tin-carbon bonds are called organotin resists. The Sn-C has a bond energy of ~2.2 eV, and it is a stronger bond than the common coordination bonds to ligands in transition metal complexes. Therefore, organotin compounds provide more chemical stability and are thus more favorable for the manufacturing processes. In addition, the versatility of the possible organotin molecular systems and the charge distribution are other attractive points for the EUV resist researchers.

Various organotin chemistries have been developed and tested as potential EUV photoresists, such as butyltin oxo hydroxo cluster (BuSnOOH) [65] (hexameric) carboxylate tin compounds ($R_2Sn(O_2CR')_2$) [63], a β-$NaSn_{13}$ [64] and tin-oxo cages (or tin-oxo clusters) [66].

Brainard et al. investigated the patterning functionality of 21 organotin carboxylate compounds of the type $R_2Sn(O_2CR')_2$ with R= butyl, phenyl and benzyl. They were able to pattern 22 nm features with a very low LER (1.4 nm) but at a very poor sensitivity[67].

The butyl variants of organotin have shown higher absorption at EUV, and the chemistry of the Sn_{12}-based oxo cages has been notably more attractive [68, 69]. The pattering capability of tin-oxo cages has been experimentally demonstrated, with sensitivities lower than 15 mJ cm^{-2} [70]. Cardineau et al.[66] were the first to introduce and evaluate the lithographic properties of eight tin-oxo cages as EUV photoresists. They found a correlation between the sensitivity of the resist to the strength of the Sn-C bonds, indicating homolytic fission of Sn-C as the initial driving mechanism [71].

Fallica et al.[72] measured the absorption cross-section of the two EUV tin-oxo cage photoresists versus a number of organic ones. The two tin-based resists belong to Inpria corporation Y-series which were put in 2015 in fab operations (their exact structure not disclosed) [55]. Absorption cross-sections of almost 15 μm^{-1} and 20 μm^{-1} were measured for the two tin materials versus 5 μm^{-1} for several organic ones.

The work of this thesis addresses the tin-oxo cages with the structure shown in Figure 1.6; its dense cage with 12 tin and 24 oxygen atoms renders a high optical density at 13.5 nm. The absorption cross-sections of a number of tin-oxo cages were measured to be 11 to 15 μm^{-1}[49, 64].

The Highest Occupied Molecular Orbital is located mainly on the Sn-C bonds of the six-coordinated Sn atoms, and the Lowest Unoccupied Molecular Orbital is composed predominantly of d-orbitals on Sn atoms and σ* orbitals on the Sn-C bonds [68, 73, 74]. The synthesis of the tin-oxo cage is relatively straightforward, and different counterions add to the tunability of the resist properties. Its well-defined molecular structure with a small size of ~1.5 nm potentially promises higher resolution and lower LER. Tin-oxo cages generally act as negative tone resists, but in previous work, the positive tone was observed at very low EUV beam and E-beam exposure doses [75].

In previous work, our team used electron irradiation to mimic the interaction of low energy electrons (0 – 40 eV) with the tin-oxo cage sample. It was shown that electrons with energy as low as 1.2 eV can cause the cleavage of the ligands through the electron attachment mechanism, and more energetic electrons trigger the photoreactions through ionization. Electrons with energy >2 eV can lead to a full condensation and a solubility switch of the resist as described in two sequential steps: carbon loss with partial cross-linking and then the formation of the denser product because of the maximum possible aggregation of the SnOx inorganic fragments [76].

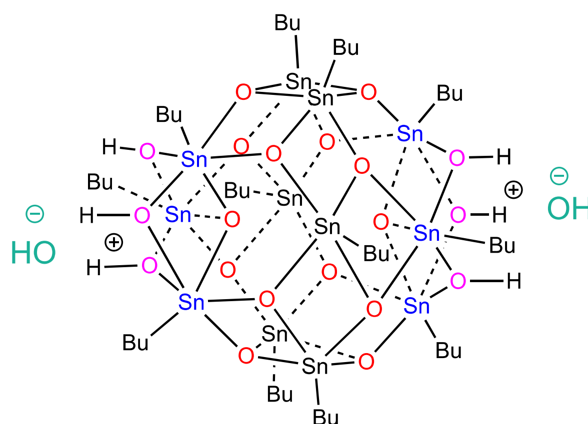

Figure 1.6. Tin-oxo cage with hydroxide counter ions (TinOH): $[(SnBu)_{12}O_{14}(OH)_6](OH)_2$. The counter ions can be swapped with other anions.

Different technologies were utilized to study the patterning potential of the tin resist and, importantly, to gain better insight into the EUV-induced chemistry of the tin-oxo cage as a model resist.

Despite the efforts made in the cited studies, the obtained understanding of the photoreactivity of the tin-oxo cages is very vague, and therefore, this thesis tries to unravel some of the unanswered questions using various excitation sources and different metrology and spectroscopy techniques. Chapters 3 and 4 describe the study of tin-oxo cage under exposure to broadband XUV pulses from a high-harmonic generation source in the ranges 25 – 40 eV and 45 – 70 eV. Throughout this thesis, we use XUV to refer to photon energies up to 150 eV, while EUV explicitly points to 13.5 nm (92 eV), the wavelength of the LPP Sn source for nanolithography. The development and the details of the HHG setup are presented in experimental setups and methods in Chapter 2.

1.4 High-harmonic generation

High-harmonic generation (HHG) is the fundamental process for generating broadband, coherent optical pulses on femtosecond and attosecond time scales. These pulses are commonly used as a light source in the soft-X-ray region. One great advantage of HHG-based light sources is the coherence of the pulses, which provides the opportunity for metrology applications in atto- or femtosecond time scale. High-harmonic generation enables the study of the ultrafast chemical dynamics such as the lifetime of highly excited states, internal conversions, structural changes, and charge migration in molecules [77, 78].

High-harmonic generation occurs due to the nonlinear response of irradiated atoms with highly intense laser pulses. Typically, reaching such high intensities involves amplified femtosecond laser pulses. Pulses with lower energies but high repetition rates are generated inside the laser oscillators. The pulse energy is enhanced via chirped pulse amplification (CPA). Here the laser pulse energy is increased after temporally stretching the pulses while preserving the pulse's spectral bandwidth, which allows subsequent temporal compression back to femtosecond pulse durations (Figure 1.7) [79, 80].

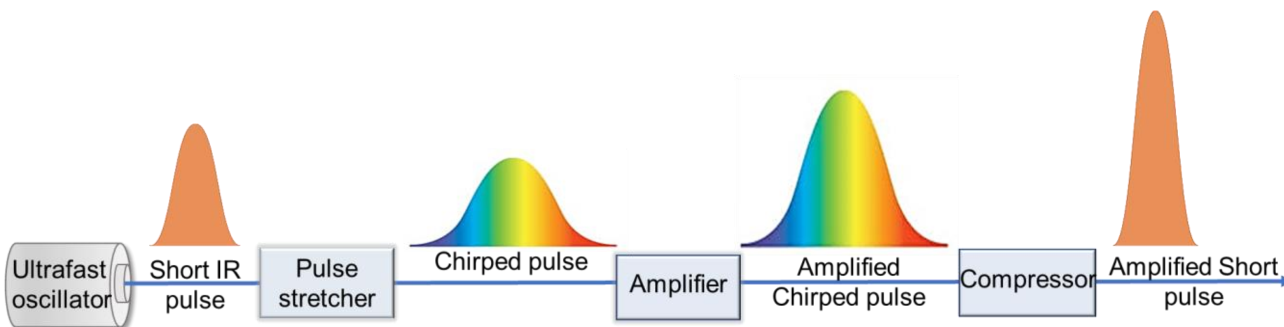

Figure 1.7. The schematic from CPA principals for the generation of high-power optical pulses.

The high-power pulses are then focused loosely into a medium (gas, liquid, solid) where HHG occurs. The HHG in this thesis is based on the interaction of femtosecond laser pulse with gas atoms.

1.4.1 Microscopic picture of high-harmonic generation

The HHG process has to take into account the microscopic level that explains the attosecond pulse generation on a pulse's subcycle time scale; and also the phase-matching conditions at the macroscopic level, which describe how the coherent addition of the emission from many atoms builds up across the interaction length between gas and laser and is thus important for the overall XUV generation efficiency.

Several approaches have been developed to model the fundamental events on the subcycle level; here we focus on the quasiclassical three-step model [81, 82].

Keldysh introduced a theory for ionization in strong laser fields. The Keldysh parameter in equation (1.2) is often used to classify the ionization process [83, 84] .

$$\gamma = \sqrt{\frac{I_p}{2U_p}} \tag{1.2}$$

I_p is the ionization potential, and U_p is the electron's ponderomotive energy or the gained mean energy of a free electron during acceleration in continuum in one optical cycle of laser field:

$$U_p = \frac{e^2 E_0^2}{4m_e \omega_0^2} \propto \lambda_0^2 I_0 \tag{1.3}$$

ω_0 and E_0 are the central frequency and the amplitude of the laser [84, 85]. I_0 is the peak intensity of the laser.

In general, if γ<<1, it is called the quasi-static regime where the possibility of tunnel ionization dominates over the multiphoton ionization (γ >>1). The electromagnetic field intensity of around 10^{14} W/cm^2 falls in the regime of tunnel ionization [83].

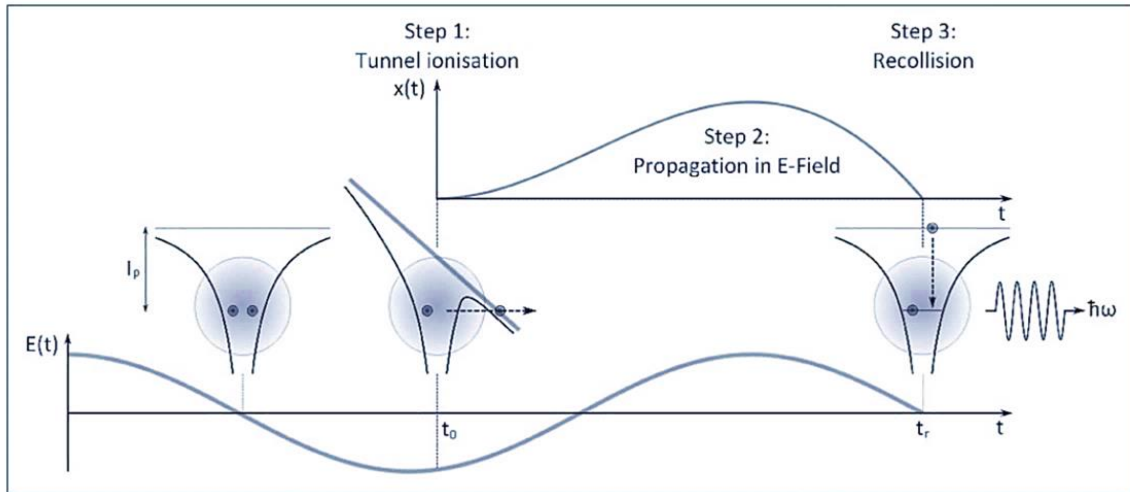

Figure 1.8. Three step model representation of high harmonic generation, the image is taken from ref [78].

The quasiclassical three-step model is schematically shown in Figure 1.8. As shown, when the oscillating electric field satisfies the condition of γ<<1, it can perturb the atom's Coulomb potential and create a finite potential well. Then the electron has the chance to escape the potential well, which is known

as tunnel ionization. Since the magnitude of the electric field maximizes in each half cycle, the electron escape can occur twice per cycle. Electrons leaving the parent atoms follow trajectories whose spatial excursion amplitude depends on the ionization time and the driving laser frequency [84, 86, 87].

The laser field in the time domain can be described with equation (1.4) in which ω_0 is the central frequency of the laser field.

$$E(t) = E_0 sin\,(\omega_0 t) \tag{1.4}$$

Considering the spatial origin of ionization at x=0 and the assumption that electrons leave the atom with zero velocity (v=0), the spatial excursion amplitude of the electrons becomes:

$$x(t) = \frac{eE_0}{m{\omega_0}^2}[sin(\omega t) - sin(\omega_0 t_i) - \omega_0(t - t_i)cos\,(\omega_0 t_i)] \tag{1.5}$$

t_i is the ionization time. During this travel, electrons gain acceleration and therefore energy under the influence of the laser field. This is the second step in the three-step model, called the acceleration step.

The third step is recombination. The free electron may return to its parent ion and release the accumulated energy during the excursion by emitting photons upon recombination at time t_r. The relationship between ionization time and recombination time can be found from the zeros of Eq. 1.5, i.e., by requiring the electron to return to the location where it was ionized from. The photon energy is the ionization potential plus the kinetic energy of the electron acquired during the excursion:

$$E_{ph} = I_p + \frac{1}{2}m_e v^2(t_r) = I_p + 2U_p[sin(\omega_0 t_r) - sin\,(\omega_0 t_i)]^2 \tag{1.6}$$

In equation (1.6), the maximum of the time dependent term is equal to $3.17U_p$.Therefore, it can be rewritten as equation (1.7) , where the maximum energy is called cutoff energy.

$$E_{ph} \leq I_p + 3.17U_p \tag{1.7}$$

Comparing equations (1.3) and (1.7), harmonics can be extended to higher cutoff energies by increasing the wavelength and the intensity of the laser beam. A higher cutoff also can be reached using gases with higher ionization potential. However, there is a restriction on the maximum applied field. Too intense fields can fully ionize the atoms in the medium. High degrees of ionization could lead to defocusing of the laser beam and general issues with phase matching due to an imbalance of dispersion

created by pulse propagation in the plasma. Also, the depletion of the medium could occur before the arrival of the pulse peak, particularly in the case of long wavelengths.

The HHG steps happen at each half cycle of the laser field in the time domain. The half-cycle periodicity ($T_C/2$) in the time domain means a periodicity of twice the laser field's frequency in the frequency domain at odd digits of the fundamental frequency, called odd harmonics. Thus, the HHG process leads to the emission of odd harmonics ($q\omega_0, q = 1,3,5, \ldots$) equally spaced at twice the energy of the fundamental beam (Figure 1.9a).

The absence of light in the spacing between the harmonics is not desirable in spectroscopy applications. Different techniques are used to address this issue and provide more light coverage in the measurements. The full coverage can be achieved with continuum generation based on self-phase modulation of few-cycle laser pulses in strongly nonlinear media such as hollow-core fibers filled with gas atoms [88].

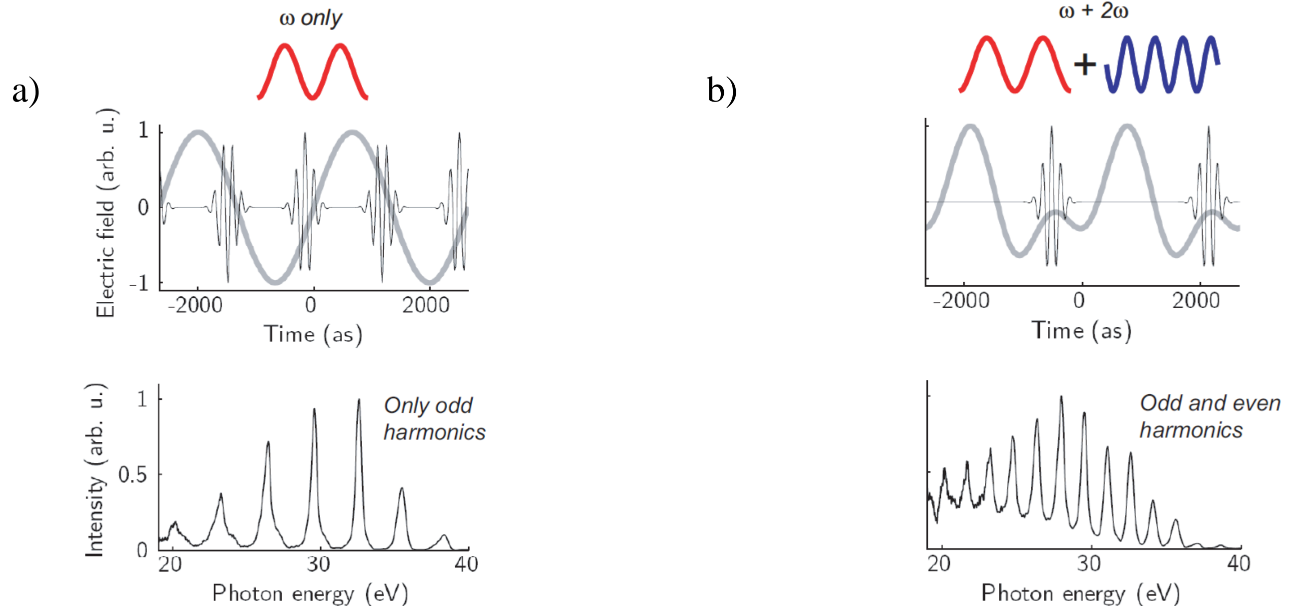

Figure 1.9. a) Using the IR beam at the fundamental frequency of ω_0 leads to the emission of odd harmonics with the spacing of $2\omega_0$. b) Adding the second harmonic of the fundamental beam to the generation processes results in the emission of both even and odd harmonics spaced with ω_0. The graph is taken from ref [89] .

One relatively straightforward approach to further reduce the spacing is to break the $T_C/2$ periodicity by adding the fundamental beam's second harmonic to the generation processes. This makes the emission of even harmonics possible, and the generation occurs at each fundamental frequency [89], as shown in Figure 1.9b. This approach is used in this thesis for the high harmonic absorption spectroscopy of tin-oxo

cages in Chapters 3 and 4, and the details of the HHG setup based on two-color generation are explained in Chapter 2.

1.4.2 Phase matching conditions

The HHG photons are emitted by different atoms across the interaction area between the gas jet and the beam. The total generated signal is the coherent sum over all emitters in the nonlinear interaction medium. Therefore, any accumulated phase mismatch between the emissions at different spatial regions can reduce the efficiency (flux) of HHG on the macroscopic scale [85, 90]. The phase mismatch between the harmonic order of q at a frequency of $q\omega_0$ and the fundamental beam (ω_0) is represented by:

$$\Delta k(i) = qk_0 - k_q \tag{1.8}$$

Where k is the wavevector of the q_{th} harmonic and k_0 is the wavevector of the fundamental beam. Figure 1.10 illustrates the effect of phase mismatch on XUV generation efficiency.

$a) \rightarrow \Delta k \neq 0$

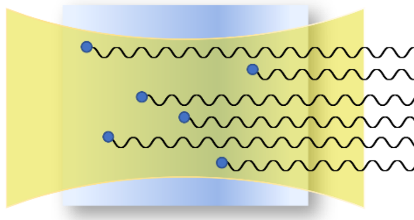

$b) \rightarrow \Delta k = 0$

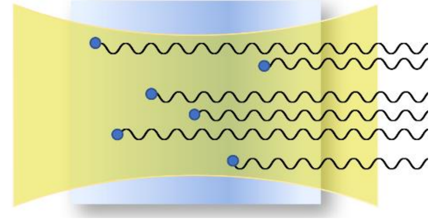

Figure 1.10. Schematic presentation of the phase-matching condition. a) The phase mismatch between harmonic emitters at different locations leads to the destructive buildup of the HHG. b) Harmonics are emitted in phase, leading to the constructive interference between different XUV photons. In this case, maximum HHG efficiency can be achieved.

In general, there are four main factors leading to the total phase mismatch with positive or negative contribution (signs) as shown in equation (1.9):

$$\Delta k(i) = qk_0 - k_q = \underbrace{\Delta k_{Gouy}}_{<0} + \underbrace{\Delta k_{neutral}}_{>0} + \underbrace{\Delta k_{plasma}}_{<0} + \underbrace{\Delta k_{dipole}}_{<0 \text{ or } >0} \tag{1.9}$$

One term is the geometrical phase mismatch mainly resulting from the Gouy phase shift, $\zeta(Z)$ in equation (1.10) , of laser beam at focus. A Gaussian beam passing through the focus undergoes a phase shift which is different from a plane wave with the same frequency. The maximum Gouy phase shift is equal to -π for

propagation from the far field before the focus to the far field after the focus. For example, Gouy phase can be controlled by placing the beam focus at a different position relative to the gas medium.

$$\zeta(Z) = -tan^{-1}\frac{Z}{Z_R} \tag{1.10}$$

In equation (1.10), Z_R is the Rayleigh length of a Gaussian beam and $Z= 0$ corresponds to the position of the beam waist. Therefore, the induced phase mismatch can be written as shown in equation (1.11) which is always negative.

$$\Delta k_{Gouy} = qk_{0,G} - k_{q,G}\; qk_{0,G}\;,$$
$$qk_{0,G} = q\left(\frac{d\zeta}{dZ}\right) = -q\left(\frac{d\left(tan^{-1}\frac{Z}{Z_R}\right)}{dZ}\right) < 0 \tag{1.11}$$

The second term is due to dispersion caused in a neutral medium as the refractive index of the medium for the fundamental and harmonics are different. Since in general, the refractive index of the medium, is lower for XUV wavelengths than for the fundamental beam, $n_q < n_f$, the neutral dispersion term is positive. The refractive index is proportional to the gas pressure and the neutral (not-ionized) fraction of gas atoms in the generation medium and therefore, for example, can be controlled by tuning the gas pressure and modifying the laser intensity.

$$\Delta k_{neutral} = qk_f - k_q = q\frac{\omega}{c}\left(n_f - n_q\right) > 0 \tag{1.12}$$

The third factor that could disturb the constructive interference of the harmonics is plasma dispersion. The high intense laser can lead to emission of free electrons and the formation of plasma. The plasma refractive index depends on the electron density and the laser frequency. The plasma refractive index, n_p, experienced by a given frequency (ω) is given in equation (1.13). Since the plasma refractive index is larger at higher frequencies ($n_q > n_f$), the plasma dispersion contribution is negative.

$$n_p(\omega) = \sqrt{1 - \frac{\omega_p^2}{\omega^2}} \tag{1.13}$$

$$\omega_p = e\sqrt{\frac{N_e}{\varepsilon_o m_e}} \tag{1.14}$$

In equations (1.13) and (1.14), ω_p is the plasma frequency, N_e is the density of free electrons and ε_o is the vacuum permittivity.

The last term is the atomic (intrinsic) dipole phase mismatch. An electron during its travel trajectory until recombination accumulates a phase, ϕ_d, which is intrinsic to the HHG process. The dipole phase varies linearly with the intensity of the light: $\phi_d \propto I(x, y, z)$ [91]. Thus, the radial and longitudinal changes in the intensity profile can cause the spatial dipole phase variations in the generation medium and it could have a negative or positive contribution depending on spatial gradient of the phase (equation (1.15)).

$$\Delta k_{dipole} \propto \frac{\partial I(x, y, z)}{\partial z} \tag{1.15}$$

Therefore, by balancing out the parameters influencing the different contributions to phase mismatch in equation (1.9) it is possible to minimize the Δk and boost the coherent buildup of the XUV photons and the generation yield over the nonlinear medium. In practice, the beam intensity, Rayleigh length, gas pressure, the size of the gas cell, beam spot size and its spatial and temporal profile, and the beam focus position relative to the gas jet are examples of the parameters to be tuned to improve the generation [85, 92].

1.5 Aims and outline of this thesis

This thesis mainly focuses on studying Tin-oxo cage material as a potential candidate for EUV photoresist and understanding the driven photoreactions inside the resist upon exposure to light. In this thesis, we gained a better insight into the resist's photochemistry, utilizing various metrology techniques and exposing the resist to different light sources, such as monochromatic and broadband beams with wavelengths within the soft-X-ray regime.

Chapter 2 is devoted to the experimental section in which we provide a detailed explanation of the home-made HHG setup and BEAR beam line in the Elettra synchrotron. Then we discuss the approaches used to analyze the obtained data from the measurements run via the mentioned setups. Furthermore, this chapter gives a general summary of resist’s thin film preparation on silicon nitride membranes and the thickness measurement using ellipsometry.

In **chapter 3**, the photochemistry of the tin cage resist with OH counterions (TinOH) is studied by performing XUV broadband (HHG) absorption spectroscopy on the resist. A home-built HHG setup is used as the exposure source, delivering XUV broadband pulses in the range of 25 – 40 eV. The induced changes in the resist's absorption during the exposure time are used to understand the resist's reaction mechanisms and to obtain the Dill parameters of the resist over the 25 – 40 energy range.

Chapter 4 presents the result of XUV absorption spectroscopy after improving the HHG setup and extending the measurement energy range up to 70 eV using the Ne harmonics. The induced absorption changes in 21 – 40 eV and 42 – 70 eV, from Ar and Ne harmonics, are compared, and the resist's Dill parameters are extended to 70 eV.

In **chapter 5**, we study the electron yield of the resist and its changes with exposure time over the energy range 5 – 150 eV using the monochromatic radiation of the synchrotron, and the secondary electron yield of the resist is estimated. The photoelectron spectra of the resist are also investigated at a few selected energies from 35 to 120 eV, and the results are compared with the predicted ionization cross-section of the resist.

In **chapter 6,** the photochemistry of the resist is studied from another view. Under exposure to a EUV beam (92 eV) source, the resist's outgassing species are recorded, analyzed and connected to the possible induced reactions rendering the detected products. Besides, this chapter studies the resist's sensitivity and thickness change as a function of exposure at 92 eV.

Chapter 2

Experimental setups and methods

Chapter 2 describes the setups and the methodology used throughout this thesis to perform different measurements on the EUV photoresist of interest, tin-oxo cage compounds, and the procedures used to analyze the resultant data.

Section 2.1 is devoted to a detailed description of the home-built high-harmonic generation (HHG) setup developed during the project, which has been used to generate extreme ultraviolet (XUV) photons in the range 25 to 70 eV from a fundamental IR (800 nm) femtosecond laser beam. The broadband XUV photons are used as the irradiation source for conducting the high-harmonic absorption spectroscopy of the tin-oxo cage resists, as discussed in Chapters 3 and 4. This section also contains the method for implementing the HHG based absorption measurements, sample preparation and the various data analysis procedures.

Two photoelectron spectroscopy techniques are used to investigate the tin-oxo cage resists utilizing the Elettra synchrotron radiation. They are total electron yield (TEY) measurement and X-ray photo electron spectroscopy (XPS), which are the main topics of Chapter 5. Section 2.2 briefly introduces these two methods, the beamline configuration used for the measurements and the corresponding sample preparation. The TEY data analysis is not very straightforward, and therefore I describe, in detail, how to convert the measured current from the sample as raw data to the number of electrons per incident photon on the sample as the final results in a TEY measurement.

High-harmonic absorption spectroscopy is only feasible by spin coating thin films of the resist on thin transparent substrates due to the short attenuation lengths in the XUV spectral range. However, the thickness measurement of the prepared thin films is challenging. AFM cannot be applied due to the fragility of the substrate, and ellipsometry data can suffer from noise due to the low reflection from the

transparent substrates. In section 2.3 of this chapter we provide examples of the ellipsometry results on the resist films and describe the models used to fit the ellipsometry data to obtain the thickness.

2.1 High-harmonic absorption spectroscopy

2.1.1 Experimental setup for high-harmonic generation and extreme-ultraviolet absorption measurements

We developed a tabletop high-harmonic generation (HHG) setup that can generate (broadband) XUV pulses from fundamental 800 nm laser pulses. The laser is a Solstice Ti:sapphire Amplifier system from Spectra-Physics, that delivers 800 nm, 35 fs pulses at a repetition rate of 2 kHz. The overall output of the laser is 3.5 mJ per pulse, of which 2.2 mJ is sent to the beamline for high-harmonic generation and the rest is used to pump an optical parametric amplifier (OPA) system (TOPAS-Prime, Light Conversion). The OPA system delivers pulses between 230 nm and 2500 nm wavelengths with 10 µJ per pulse in the UV and up to 300 µJ/pulse in the IR range.

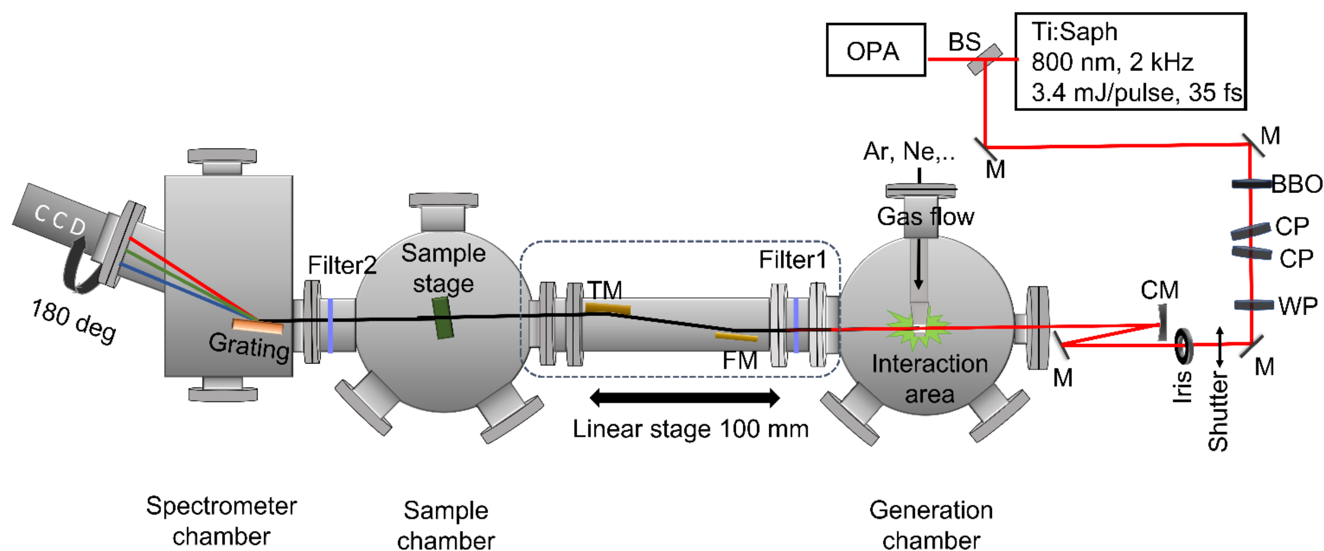

Figure 2.1. Schematic layout of the high harmonic generation beamline. M: mirror, WP: wave plate, CP: calcite plate, CM: concave mirror, FM: flat mirror, TM: toroidal mirror. Filter 1 and filter 2 are 200 nm and 100 thick Al filters.

Figure 2.1 shows the general layout of the setup used to generate XUV harmonics. We can divide the setup design into two main parts. The first one is the part of the beam path outside the vacuum. The second

part is the beam path inside the vacuum chambers designed for the generation of XUV pulses and performing measurements with these pulses on samples.

The beam path outside the vacuum contains all the optics used to direct the laser beam to the vacuum systems or modify the beam properties to optimize the high-harmonic generation process. In a collinear geometry, a BBO crystal doubles the frequency of the IR beam to obtain 400 nm pulses. The thickness of the BBO is 0.1 mm to limit the stretching of such short pulses. The intensity ratio of the generated 400 nm to the IR was measured to be 12%. The 400 nm pulse modifies the intense electromagnetic field of the 800 nm beam to break the symmetry of the generation process. The use of this two-color field in high-harmonic generation provides more spectral coverage by generating both even and odd harmonics, which is favorable for spectroscopic applications [93, 94].

The group velocities of the two beams in the BBO crystal are different, which causes a relative delay of the two pulses. Therefore, we use two calcite plates to compensate for this group delay. Then a wave-plate rotates the polarization of 800 nm by 90 degrees so that both 800 and 400 nm beams have the same polarizations. We use S polarization due to higher reflectivity of the optics, which is especially true for the gold-coated mirrors reflecting XUV pulses inside the vacuum chambers. A silver concave mirror (CM) of 500 mm focal length focuses the light into the gas jet inside the first vacuum chamber, where XUV photons are generated. The CM mirror is placed on a translation stage to adjust the focus position relative to the gas jet. The last flat mirror before the CM minimizes the incident angle of the beam relative to the concave mirror's normal, which reduces the aberrations and ensures a decent Gaussian profile at the focus. The spatial and temporal focus profiles are inspected using a CMOS camera and by recording Frequency-resolved optical gating (FROG) traces. A shutter located in the beam path is triggered by the software to control the sample's exposure time and avoid the streaking effect in the CCD.

When the iris, shown in Figure 2.1, is fully open, we get an FWHM of 55 μm at the focus for the IR pulse. A peak power density of more than 3×10^{14} W/cm^2 was estimated from the measured cutoff frequency of harmonics in argon. As HHG is most efficient out of focus, the peak power density in focus was higher.

Since XUV light is absorbed in air, the generation and measurements are performed inside vacuum. There are three main chambers marked in the drawing as the generation, sample and spectrometer chambers interconnected with different bellows and hoses. Two molecular turbopumps (Edwards, 48K rpm) are connected to the generation and sample chamber and a Pfeiffer 90K rpm turbo pump to the

spectrometer chamber. Two scroll pumps back the turbo pumps up to the pressure of 10^{-2} mbar. The entire system can reach approximately 10^{-7} mbar pressure.

The generation chamber contains the gas nozzle, and different gases can be injected into the nozzle. A mass flow controller (IN-FLOW, Bronckhorst) guarantees a constant pressure of the gas inside the nozzle. The nozzle can move in x, y-direction, which provides further tunability relative to the beam's focus for optimizing the phase-matching condition for HHG.

As already explained in the introduction section 1.4.1, the energy range or the cutoff of the harmonics can be extended to higher energies using gases with a higher ionization potential, though at the expense of a lower generation efficiency. Our experiments used argon and neon as the generation media, which yields conversion efficiencies, on the order of 10^{-6} and 10^{-8} in Ar and Ne, respectively.

The conversion of fundamental photons into the XUV beam occurs in the interaction area between the intense light at focus and the gas jet. We need to optimize the phase-matching condition in the interaction area to maximize the constructive build-up of the generated XUV photons. This optimization is fulfilled by adjusting the iris opening, temporal compression of the beam, tuning the relative position of the beam's focus to the gas jet and adjusting the gas pressure.

The XUV photons pass through a 200 nm thick metallic filter (Al or Zr from Luxel) which suppresses the remaining fundamental beams. A gold-coated toroidal mirror with a focal length of 420 mm (estimated from the tangential and sagittal curvatures) and 10 degrees of grazing incidence angle reimages the harmonics with a demagnification factor of 1.2 into the sample chamber where the samples are mounted. The distance between the nozzle at the generation chamber and the center of sample chamber is around 1.3 meters. The flat mirror (FM) before the toroidal ensures the incident grazing incidence relative to the surface of the toroidal. These two mirrors are mounted inside an edge welded bellow, specified by the dashed area in Figure 2.1, which can move forward and backward along the beam propagation path on a 100 mm translation stage. This design helps us to adjust the beam spot size on the sample and therefore the incident XUV power density on the sample.

The beam's spot size at the sample position is measured using the knife-edge measurement method or by exposing the photoresist at the given position. In the latter case, the photoresist undergoes a distinct change at the exposed area, and then the FWHM of the exposed area can be measured under an optical microscope or using AFM (Figure 2.2).

A sample holder is designed to accommodate the samples within the sample chamber. The holder is mounted on a SmarAct positioning stage, providing movements along the x, y, z and rotatory axes (Figure 2.4b).

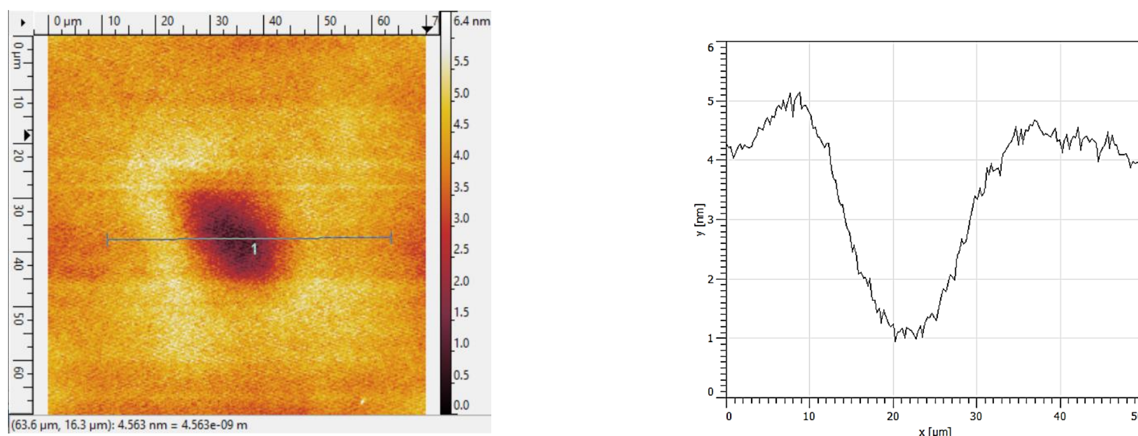

Figure 2.2. AFM image from the exposed spot resist in one high-harmonic absorption spectroscopy measurement using the argon harmonics. The color scale indicates the thickness change at the exposed spot in resist after 13.3 seconds exposure (at estimated dose of ~137 mJ cm^{-2}) representing ~3 nm thickness reduction.

The transmitted XUV photons from the sample then proceed toward the spectrometer chamber, and another filter (Al, 100 nm thick) prevents more of the fundamental and stray light from reaching the spectrometer and detector.

A gold-coated, flat-field concave grating from Hitachi disperses and focuses different wavelengths onto the focal plane 235.3 mm away, where the detector is located. The grating is also used in grazing incidence angles as most other optics in the X-ray range.

The detection system is a soft-X-ray sensitized charge-coupled device (CCD) camera (GE 2048 512 BI UV1, GreatEyes), and its detection plane is located at the focal plane of the grating. The CCD is installed on an in-vacuum rotatable flange able to rotate the CCD by 180 degrees to capture different energy ranges from the spectrally dispersed broadband light on the focal plane of the grating. If the grating is at the right incidence angle, the CCD captures light within energies from 22 to 45 eV in the low energy position and from 45 to 100 eV in the high energy position after rotation by 180 degrees.

The typical high harmonics spectra generated in argon are plotted in Figure 2.3a. The red curve shows the odd harmonics when only 800 nm is used as the fundamental beam for the high-harmonic generation. The spectrum in blue color is the result of the generation of both odd and even harmonics when the fundamental 800 nm beam is modified with the electromagnetic field of its doubled frequency, 400 nm. Usually, a pressure of around 20 mbar is used for generation in argon. The generation of both odd and even

harmonics provides more spectral coverage for the absorption measurements. Figure 2.3b shows the high harmonic spectra using neon as the generation medium and setting 40 mbar for the pressure.

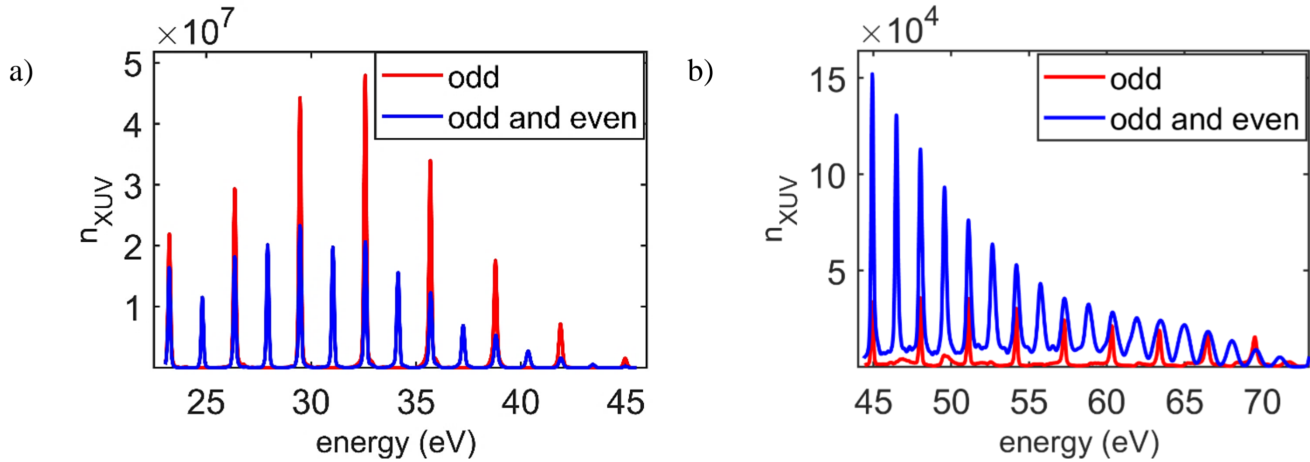

Figure 2.3: High-harmonic spectra for the generated odd harmonics of 800 nm plotted in red, odd plus even harmonics in blue color. a) using argon as generating medium and integration time of 45 ms, b) using neon and integration time of 200 ms. n_{XUV} refers to the number of XUV photons.

2.1.2 XUV induced bleaching measurements

Thin films of the tin-oxo cage EUV photoresist were prepared by spin-coating solutions of the resists in toluene on 30 nm thick silicon nitride membranes. The silicon nitride window measures 3 mm × 3 mm, centered on a square 500 µm thick silicon frame with 7.5 mm × 7.5 mm dimensions.

The solution's concentration depends on the desired thickness of the film. For example, the tin cage resist has much higher absorption in the XUV range of 25 – 45 eV generated in argon than in the range of 45 to 70 eV generated in neon.

The tin-oxo cage was synthesized according to the recipe reported in the previous works [73, 95]. A speed of 2500 rpm, an acceleration of 750 rpm/s was used for spin coating of the tin-oxo cage resist's solution on the membranes, which then followed by a one-minute post-baking of thin films at 90 degrees. A home-made chuck was used to hold the silicon frames of the membranes during the spin coating to avoid breaking the silicon nitride windows while applying the vacuum. The thicknesses of the films were measured by using ellipsometry or by comparing the absorption spectrum of the resist measured in the HHG setup with the one from the CXRO database [96] over the same energy range (Chapters 3 and 4).

2.1.3 Methodology for performing measurements

Figure 2.4a depicts the general process of the absorption measurement. We expose the sample to XUV broadband harmonics, and the CCD simultaneously records the transmitted broadband spectrum. Therefore, we monitor the induced changes in the optical properties of the material as a function of exposure time, which later is connected to the possible photoinduced chemical changes in the resist upon exposure.

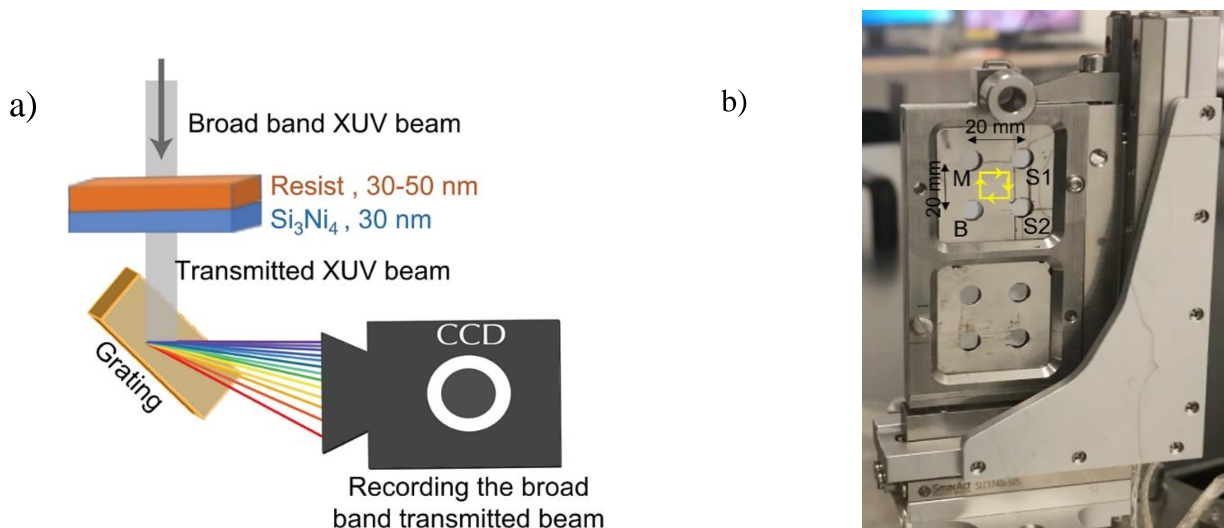

Figure 2.4. a) Pictorial illustration of the HHG absorption measurement. b) Picture of the sample holder representing how the samples are mounted for a HHG absorption measurement. S1 and S2: thin films of the resist (I_s). M: membrane (I_{mem}), B: incident beam is sent through an empty spot (I_0). The yellow arrows indicate the movement between membrane, samples (S_1 and S_2) and beam out positions in a measurement cycle.

Since the sample is coated on a silicon nitride membrane, we need to exclude the contribution of the silicon nitride membrane to the recorded transmission spectrum. Therefore, we mount a similar silicon nitride window on the same sample holder to measure the amount of transmitted light after the membrane. As shown in Figure 2.4, the light passing through the empty position (I_0) and transmitted after the membrane (I_{mem}) and sample (I_S) are recorded continuously in a cycle. The shutter opening and closing time, the stage movements and the CCD operation time are all synchronized by a homemade software. Therefore, during the stage's movement in a cycle from one spot on the resist to one on the membrane, the shutter is closed and hence no exposure occurs on the samples.

To elaborate more on the measurement scheme, we move onto a spot on the resist thin film and record images from the transmitted light at that spot by exposing the sample for the exposure time *t*. The usual

setting for t is in order of a few hundred milliseconds. The stage then moves to the spot on the membrane, and we expose it and record images simultaneously for the same exposure time t. We repeat this movement between the same spots on the sample and membrane for n cycles until we reach the desired exposure time: $t_{\exp} = n \times t$.

The timing of t and the continued movement between the sample and membrane during the measurement allow us to trace the changes in the optical properties of the resist over the exposure time more precisely by taking into account the photon flux fluctuations in the HHG beamline.

2.1.4 Data processing

2.1.4.1 Spectrally resolved absorption spectrum

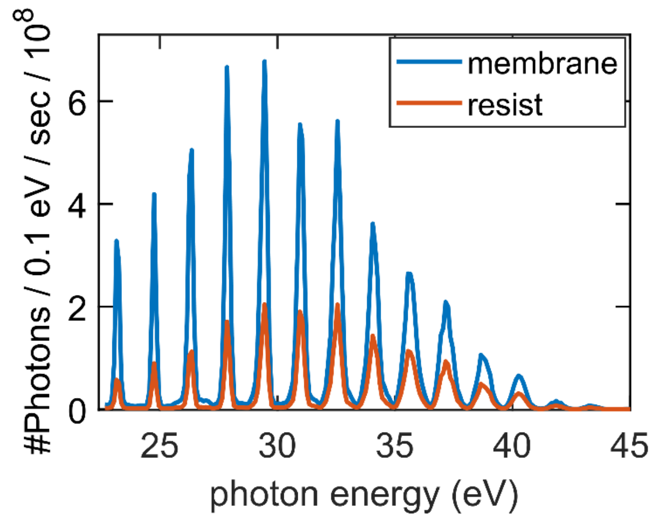

Figure 2.5. Representative high harmonic transmitted spectra after the resist thin film and neat membrane.

Following the measurement's methodology specified in section 2.1.3, we can obtain the resist's transmission spectrum, $T(E)_i$, per exposure cycle i and as a function of the photon energy over the exposure time of t_i according to equation (2.1).

$$T(E)_i = \frac{I(E)_{t_i,S}}{I(E)_{t_i,mem}} \tag{2.1}$$

In equation (2.1), E and T represent photon energy and the transmission, respectively, and S refers to the resist, *mem* to the blank SiN membrane. The dark current of the CCD is subtracted from the recorded signals for both membrane and sample before calculating the transmission. Throughout the thesis, we use

the natural logarithm to calculate the absorbance of the resist from the transmission data, as is common in the community of X-ray users, equation (2.2).

$$A(E)_i = -ln(T(E)_i) \tag{2.2}$$

Figure 2.5 exemplifies the recorded spectra after the resist thin film and the membrane for one measurement cycle with t_i = 100 ms, in red and blue colors, respectively. We divide the spectrum of the resist by that of the membrane using equation (2.1) to obtain the raw absorption spectrum shown in Figure 2.6 in black color.

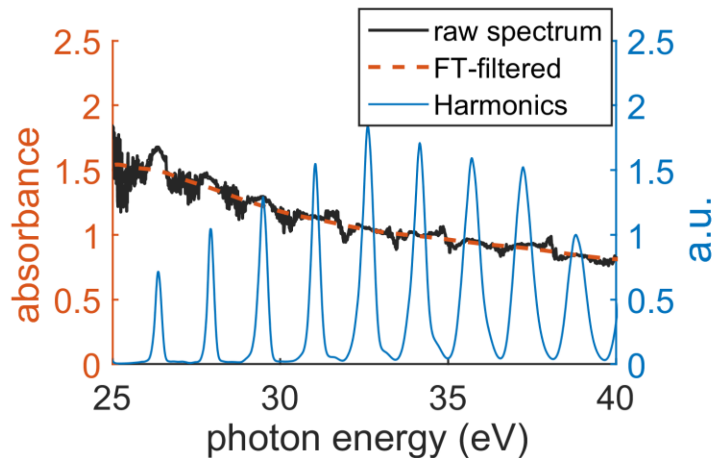

Figure 2.6. Black curve: raw absorbance of TinOAc sample obtained using equations (2.1) and (2.2). Red: resultant transmission spectrum after Fourier filtering. Blue: the high harmonic spectrum (from Figure 2.5) plotted in arbitrary units (a.u.) to make the visualization of harmonics versus absorbance possible.

As we see in Figure 2.5, there is a spacing between the harmonics where we have minimal light along the energy axis. Including these energy ranges in equation (2.1) leads to a poor signal to noise ratio in the raw transmission data. The raw absorbance (solid black line) in Figure 2.6 was obtained by dividing the harmonic spectrum transmitted through the sample by the spectrum transmitted through the membrane according to equations (2.1) and (2.2). The harmonic spectrum after the sample (blue curve) is added to the graph for qualitative comparison. As we see, the spacing between the harmonics results in lower transmission values while they suffer from a high noise level. Therefore, the raw data transmission needs further processing to get the final transmission (absorption) spectrum.

In one approach, we can apply a fast Fourier filtering method with a Gaussian lowpass filter due to the periodicity of the harmonics in the energy space to disentangle the noise from the data. The red plot in Figure 2.6 presents the result of implementing the filter to the raw recorded transmission spectrum. As another data analysis approach, in equation (2.1), we can consider a part of the spectrum I(E), that does

not fall in the spacing between the harmonics, by considering only the data points in which the intensity of each harmonic peak is greater than half its maximum. In an even simpler approach, we consider only the harmonics peaks as data points. The latter was used in data analysis of results presented in Chapter 4.

2.1.5 CCD calibration

2.1.5.1 Energy axis calibration

One method to calibrate the energy axis is using the diffraction equation of the grating in the wavelength domain, which gives a linear relationship between pixel and wavelength for a small-angle approximation. The energies of the harmonic orders, which are multiples of the fundamental frequency, appear at unique positions on the CCD and thus allow for a direct calibration of the CCD. As the harmonics can be subject to plasma-induced frequency shifts, this method is limited in accuracy to about 200 meV.

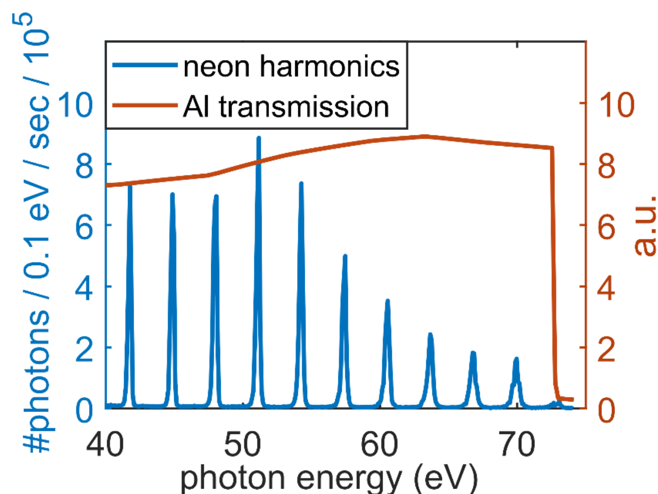

Figure 2.7. Comparing neon-generated harmonics with the Al transmission spectrum for calibrating the energy axis of the spectrum. For visualization purpose, Ne transmission spectra is normalized to the maximum of the Ne harmonics in this graph and plotted in arbitrary units (a.u.).

An alternative way is using the absorption edges of the Al or Zr filters in the beamline to calibrate the CCD camera. As illustration Figure 2.7 shows the strong absorption edge of Al filter at 72 eV, resulting in an abrupt reduction in the intensity of the harmonic spectrum at this energy which is used for the calibration of energy axis.

For energy ranges where sharp absorption edges of metal filters are unavailable, we can use the sharp autoionization (AI) lines of the noble gases, which fall in the range of 22 to 45 eV on the low energy side of the camera or between 45 and 140 eV for calibrating the high energy side of the camera.

AI states are highly excited discrete states of the atom or molecule, known as Rydberg states, which overlap with the ionization continuum of the ionized atom above the lowest ionization threshold of the atom, as shown in Figure 2.8 for argon [97, 98].

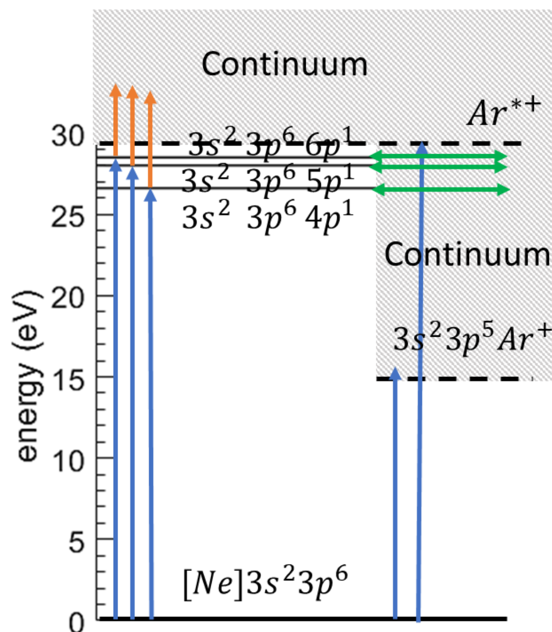

Figure 2.8. Schematic of autoionization (AI) states for argon. Blue arrows represent the promotion of electrons to the Rydberg orbitals by XUV photons and the green arrows show the interaction between the Rydberg states and the states of the argon ion [97]. The red arrows show the created transition channels to the excited continuum states in the presence of IR field at temporal overlap with XUV photons.

XUV light can excite a 3*s* electron from the ground state of an argon atom into one of the Rydberg states (*np*, *n*=4, 5, 6,…; blue arrows in Figure 2.8), which lie energetically above the ground state of the argon ion with a [Ne]$3s^2 3p^5$ configuration. Configuration interaction couples the excited Rydberg states to the continuum of the argon ion (green arrows in Figure 2.8), which results in spontaneous ionization of the atom (therefore the term autoionization), while the excess energy is released as kinetic energy of the electron. The interference between the decaying electron and the direct ionization of the argon atom leads to an asymmetric absorption profile known as the Fano profile [99-101].

A gas cell with a length of 5 mm and diameter of 500 μm is installed on the positioning stage located at the focus of the XUV pulses inside the sample chamber (Figure 2.1), which enables recording transmission spectra of XUV through gases. The energies and bandwidths of the AI lines are accurately known and precisely studied, and they can be used as benchmarks to calibrate the energy axis of the CCD and estimate the spectrometer's resolution [100-103]. The well-known wavelength (energy) values for AI lines are used

as the reference benchmarks. A linear fit is then used to interpolate between measured AI lines and absorption edges in the wavelength domain to generate an accurate calibration.

The red plot in Figure 2.9 is an example of the transmitted spectrum recorded after the gas cell filled with Ar. We can observe a strong peak with a narrow bandwidth at 26.6 eV and a smaller peak at 28 eV for the AI lines in the argon spectrum, which result from exciting the 3s $3p^6$ 4p and 3s $3p^6$ 5p states, respectively, and the interaction with the first ionization state in argon [100]. The energy axis in this graph is calibrated using the two observed AI lines.

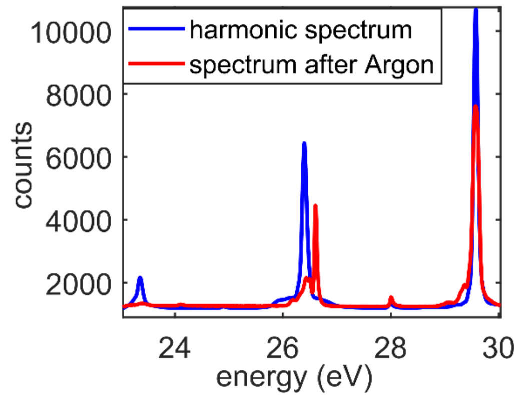

Figure 2.9. Autoionization of argon. Blue: HHG spectrum generated in argon as the excitation source. Red: HHG spectrum transmitted through argon gas in the sample chamber.

The bandwidths of the AI lines, $\sigma_{AI}(E)$, at 26.6 and 28 eV are reported in the literature to be 80 and 28.2 meV, respectively [97, 103, 104]. The spectrometer response function, $G_{spec}(E)$, can be assumed to have a Gaussian profile. We used a Gaussian function, to fit the experimentally measured peaks in our setup at 26.6 eV and 28 eV, $G_{fit}(E)$, which can be written as the convolution of the two functions according to equation (2.3), in which $\sigma_{AI}(E)$ indicates the profile function for the two AI lines, and $G_{spec}(E)$ is the spectrometer response function. Γ_{AI} refers to the bandwidth of the AI lines from literature, measured using narrowband synchrotron radiation [103]. Therefore, the square root of the variance between the bandwidth of the AI line known from literature, Γ_{AI} , and the Gaussian fit to the measured peak, Γ_{fit}, gives the spectrometer resolution at specific energy (equation (2.4)).

$$G_{fit}(E) = \sigma_{AI}(E) * G_{spec}(E) \tag{2.3}$$

$$\Gamma_{spec} = \sqrt{\Gamma_{fit}^2 - \Gamma_{AI}^2} \tag{2.4}$$

Using equation (2.4) determines the resolution of 80 meV and 40 meV for the spectrometer at the energies of 26.6 and 28.0 eV, respectively. Since the grating in the spectrometer of the HHG setup is designed to work optimally for the energies in the range 60-120 eV, higher resolution is expected at higher energies.

2.1.5.2 CCD intensity calibration

We are interested in estimating the incident flux on the sample using the recorded counts readout on the CCD chip [105]. Implementing this conversion includes two main steps. First, we must consider all the light intensity losses induced by optical elements in the beam path from the sample position to the CCD detection plate. The next consideration is the conversion efficiency of the CCD in generating electrons from the photons arriving on the CCD chip. We will explain the details of these two steps in the following.

Looking at the schematic of the HHG beamline in Figure 2.1, there are three sources of intensity loss between the sample position and the camera. The first is the absorption of light by the Al filter, and its transmission must be considered. $T_{Al}(E)$ stands for the transmission of a 100 nm thick Al filter in the setup with an estimated 8 nm aluminum oxide layer (4 nm front side and 4 nm backside), the absorption of which is calculated from the atomic scattering factors of aluminum and oxygen in CXRO [96]. The second element is the SiN membrane on which the sample is coated. $T_{mem}(E)$ is the measured transmission of the membrane. The third element is the grating, and we account for this loss using the (polarization sensitive) diffraction efficiency of the grating $\eta_g(E)$ specified by the manufacturer [106].

The photons reaching the CCD are absorbed in the depletion region in CCD chip's silicon layer, creating pairs of electrons and holes. Hence, we need to account for the absorption probability of photons inside the silicon layer. The absorption probability (fraction of photons absorbed) is termed by the corresponding manufacturer the quantum efficiency of the CCD, $\Phi_{CCD}(E)$, and therefore we use here the same terminology.

The next parameter is the efficiency of electron-hole pairs creation in the silicon layer from the absorbed photons, $\eta_{CCD}(E)$, which varies with the incident photon energy according to equation (2.5).

$$\eta_{CCD}(E) = \frac{E}{W} \tag{2.5}$$

W is the required mean energy to generate one electron-hole pair, which is a property of the material. From experimental studies this is reported to be 3.66 eV per electron-hole pair for silicon and constant in the soft-X-ray region [107]. Therefore, the final number of generated photoelectrons n_{e-h} in silicon layer and at incident energy E is calculated by multiplying these two probabilities:

$$n_{e-h}(E) = \eta_{CCD}(E) \times \Phi_{CCD}(E) \qquad (2.6)$$

To readout the CCD chip the photoelectrons are amplified in the camera by settings in the electronics, and they are then converted to the digital units (counts) as an image recorded by the CCD. This effect is included as the gain factor of the camera, g_{CCD}, which represents the number of counts per electron [105, 108, 109]. $I_{spec}(E)$ is the spectrally resolved spectrum recorded on the CCD, converted from counts per pixel per second to counts per energy interval per second. Taking into account all the parameters above, the number of photons impinging on the sample is given by equation (2.7) in which the dependence on E is omitted for readability:

$$n_{ph} \approx \frac{I_{spec}}{\eta_g \eta_{CCD} \Phi_{CCD} g_{CCD} T_{Al} T_{mem}} \qquad (2.7)$$

As explained in section 2.1.3, in a high-harmonic absorption measurement, we record the spectrum after a neat membrane in each measurement cycle to exclude the absorption of the membranes from the absorption of tin-oxo cages spin coated on membranes. Therefore, the recorded spectra after the membrane from the first to the last cycle during an HHG absorption measurement are considered in equation (2.7) to calibrate the dose. This way, we also take care of the changes in the incident flux on the sample occurring during the entire measurement time.

Figure 2.10a provides an example of the high harmonics spectrum after the membrane recorded on CCD, calibrated in the energy domain as shown in part b, using the energy calibration method described in section 2.1.5.1. Converting the wavelength axis to the energy one requires the following transformation on the recorded spectrum:

$$I_{spec}(E) = -I_{spec}(\lambda) \frac{h\,c}{E^2} \qquad (2.8)$$

So that:

$$\int I_{spec}(E)\, dE = \int I_{spec}(\lambda)\, d\lambda \qquad (2.9)$$

Figure 2.10c shows the estimated number of XUV photons incident on the membrane in energy space, which is identical to the incident flux on the resist. Integration of the plot in energy space leads to the number of XUV photons on the sample.

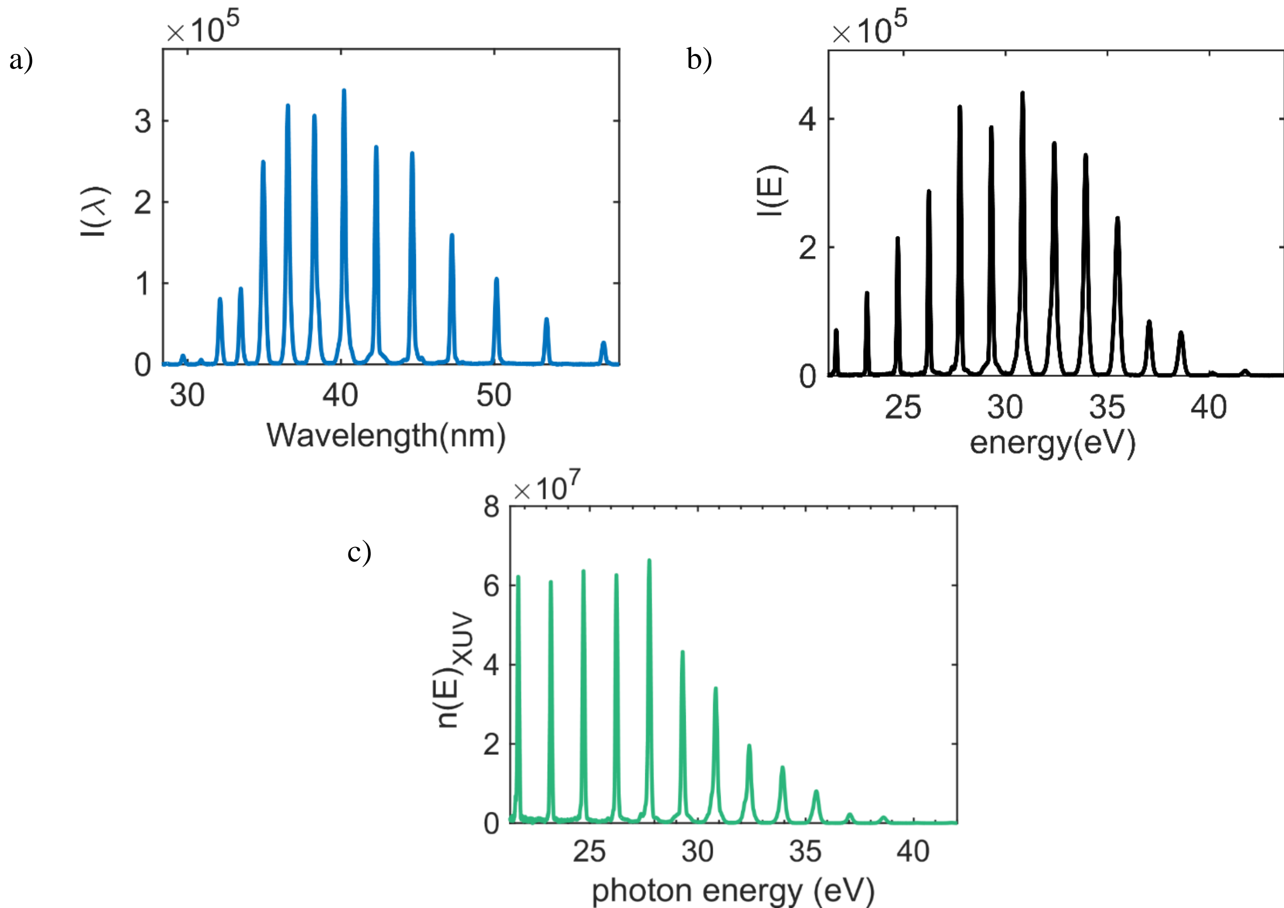

Figure 2.10. a) High harmonic spectrum after membrane as recorded on CCD. b) High harmonic spectrum after membrane calibrated in energy domain. c) Number of incident XUV photons incident on the membrane estimated using equation (2.7) in energy space.

For easier comparison, in Figure 2.5 and Figure 2.7, the numbers of XUV photons obtained using equation (2.7) are converted to the numbers of photons/0.1 eV/second, for two examples of typical spectra generated with Ar and Ne, respectively. The calculated number of XUV photons from equation (2.7) also can be normalized to the number of integrated pulses to estimate the incident energy per pulse on the sample. The usual incident energy per pulse arriving at sample position are 0.5 nJ/ per pulse for harmonics in argon and 20 pJ/pulse in neon, estimated using the described approach in this section.

2.2 X-ray photoemission spectroscopy of EUV photoresists

2.2.1 Total Electron Yield: Theory and definition

In Total Electron Yield (TEY) measurements all photoelectrons emitted from the surface of a sample irradiated with ionizing radiation are counted, independent of their energy, by measuring the sample's drain current [110-114]. A typical application is the near edge X-ray absorption fine structure (NEXAFS) measurement, in which an X-ray absorption spectrum is measured indirectly by detecting the electron yield as a function of photon energy. This assumes that the electron yield does not change with photon energy so that the detected signal is proportional to the photon absorption, which may be valid over small ranges of the photon energy [115-119].

In TEY, the photoelectrons are ejected from within a certain depth from the material's surface through elastic and inelastic scattering after absorbing the incident photons, usually from a synchrotron radiation source. TEY is a surface-sensitive method since the TEY probing depth, λ_e (or sampling depth), is only a few nanometers. It approximately lies in the range of 3 to 10 nm depending on the incident energy and the efficiency of electron scattering inside the material [120-124].

In the present work, we measure the total electron yield over a wide range of photon energies. In EUV photolithography, at an energy of 92 eV, it is commonly assumed that multiple electrons are generated per photon (primary, secondary and Auger electrons), but going to lower photon energies, near the ionization threshold, there are no electron amplification mechanisms generating more than one electron per photon. Our ultimate goal is to quantify the increasing electron yield with photon energy, which should become apparent when comparing the TEY spectrum and the independently measured (transmission) absorption spectra obtained with our HHG experiments (Chapters 3 and 4).

We used incident photons with energies from 5 to 150 eV to record the TEY. In this energy range, most contribution to the TEY signal for the higher-energy photons comes from the secondary electron cascades rather than Auger electrons and the probing depth of the technique is primarily due to the inelastic mean free path (IMFP) of secondary electrons [120-122]. Hence, quantifying the TEY yield, we could gain an insight on the number of secondary electrons generated inside the resist per absorbed photon.

When measuring X-ray Absorption Spectra in transmission mode, the absorption cross-section can be obtained from the transmission $T = I/I_0$ (where I and I_0 are the intensities (radiant power) through sample and blank) and the thickness of the sample according to equation (2.10)

$$\mu(E) = \frac{-1}{d} lnT(E) \qquad (2.10)$$

In equation (2.10), $\mu(E)$ is the absorption coefficient at photon energy E and d is the thickness.

In TEY mode, counting the escaped electrons from the sample's surface eliminates the challenge of making thin freestanding samples, or sample films on transparent substrates, which are required for the transmission mode. Deriving the absorption cross-section in TEY mode, or even the shape of the absorption spectrum, is not as straightforward as in the XAS mode. To have the desirable proportionality of TEY intensity to the absorption cross-section, one requirement is that the escape length of electrons from the samples must be much smaller than the effective light attenuation length inside the material for given incident energy; otherwise, the proportionality of the TEY signal to the absorption cross-section breaks down [115, 119, 121-123, 125, 126].

Furthermore, the geometry and details of the electrostatic field applied to extract the electrons from the surface might also lead to the deviation of the spectral shape of the TEY from the absorption spectrum. All these add further complexity in the data analysis of TEY compared to the transmission based XAS technique [111].

2.2.2 X-Ray Photoelectron Spectroscopy: Theory and definition

X-Ray-Induced Photoelectron Spectroscopy (XPS) is also a surface analysis technique. As mentioned, in TEY all electrons emitted are collected as a drain current from the sample's surface without considering their kinetic energy. But in XPS, the numbers of the emitted photoelectrons or Auger electrons are detected as a function of the kinetic energy that the released electrons gain through the photoelectric effect. In XPS, highly energetic X-ray photons can ionize the core electrons from the atomic orbitals by overcoming the binding energy (BE) of that electron and the work function of the material. Only those primary electrons originating very close to the surface can escape the surface and reach the detector without any loss. They appear as sharp peaks in an XPS spectrum, which are used to determine the binding energy of the electrons and the electron configuration of atoms in the sample, as will be described in this section. The rest of the photoelectrons undergo multiple energy losses due to inelastic scattering before

reaching the vacuum level, and they finally arrive at the detector with broadly distributed kinetic energies. These secondary electrons contribute, therefore, to a broad background signal in a general XPS spectrum.

The kinetic energy gained by the elastically scattered, primary, electrons through the photo-emissive radiation is given by equation (2.11).

$$E_k = h\nu - E_B - \phi_S + V_{bias} \tag{2.11}$$

In equation (2.11), ϕ_S is the work function of material that depends on the material properties such as crystallography, structure, and chemical composition of material at the surface. V_{bias} is the bias potential applied between the sample and the detector, giving the electrons some extra eV to escape the surface.

An electron kinetic energy analyzer is used for detecting the electrons versus their kinetic energy. The instrument also has a work function, the so-called analyzer work function ϕ_A. The analyzer is in electrical contact with the sample through the sample holder and the conductive gold substrate. This connection creates a potential difference at the surface, and electrons need to overcome that barrier before reaching the vacuum. Considering this potential difference $(\phi(\nu)_S - \phi(\nu)_A)$, the equation (2.11) is modified to equation (2.12).

$$E_K = h\nu - E_B - \phi_A + V_{bias} \tag{2.12}$$

The work function of the analyzer is determined by measuring the XPS spectrum from metals such as gold. Considering the binding energy of approximately zero for the electrons in the Fermi level of metals, the maximum kinetic energy carried by the fermi electrons is assumed to be equal to the incident photon energy in equation (2.12), which gives us the work function of the analyzer.

Assignment of the BE values to the peaks in an XPS spectrum requires precise calibration of the energy axis. The calibration is usually performed using the BE values of some reference peaks mainly from conductive materials such as the Au 4f peak at 84 eV. The positive charge induced in insulating materials by the photoemission of electrons can reduce the kinetic energy of the photoelectrons, shifting the peaks to higher BE energy values [127-129].

Therefore, experimentally detecting the energy of electrons, we can determine the binding energy of electrons, which has made XPS an effective commonly used analytical tool to investigate the chemical composition and the electronic structure of the elements in a material at surfaces.

2.2.3 TEY and XPS instrumentation

To investigate the photoelectron spectra of the resists and perform TEY measurements, we used the BEAR beamline in the Elettra synchrotron located in Trieste, Italy, in collaboration with the group of prof. Stefano Nannarone.

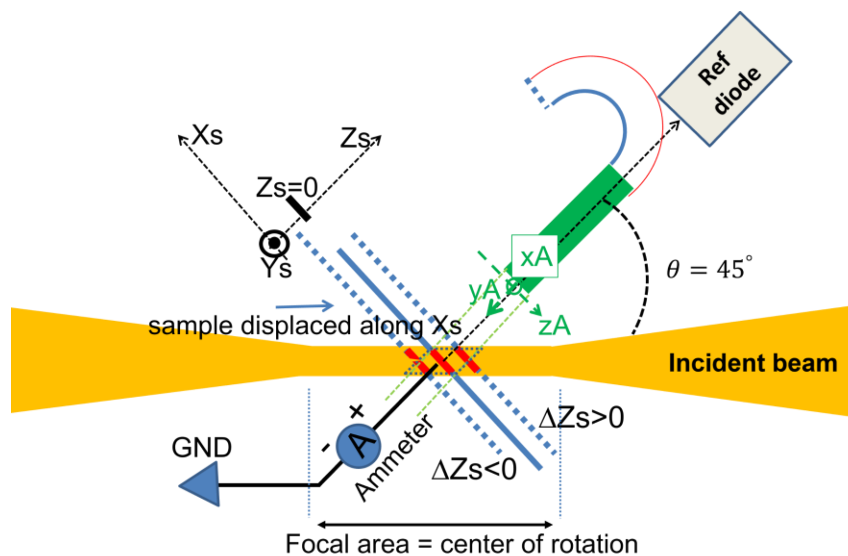

Figure 2.11. The relative positions of sample (S), electron analyzer (A), reference (Ref) diode and the incident beam in the BEAR beamline. For TEY measurements, the ammeter measures the drain current from the sample. The electron analyzer measures the intensity or and the kinetic energy of the photoelectrons in electron kinetic energy analyzer mode as in the case of XPS measurement.

The first step in performing a measurement is the proper alignment of the sample relative to the incident beam and the detectors, as the geometry depicted in Figure 2.11. This alignment is more critical in the case of XPS measurements, where the direction of the detector collecting the emitted photons relative to the samples' surface plays a significant role in the detection efficiency. However, both for TEY and XPS, the correct alignment of the sample relative to the beam's focus position is important for the precise calibration of the incident dose on the sample.

In this beamline configuration, the incident light and the electron analyzer make an angle of 45° relative to each other, and the analyzer collects the electrons at a normal angle from the surface of the sample. The electron analyzer and sample positions are specified as xA, yA, zA, and xS, yS, and zS in Figure 2.11, respectively.

For the alignment, first we move the analyzer out of the way between the sample and a reference diode located in the same direction. Then the tilt of the sample is optimized by aligning visible light

reflected from the sample surface to the reference diode before running the measurements. The visible light passes through the same beam path as the incident X-ray light. When the alignment of the sample relative to the incident beam is done, the analyzer is moved back to its initial position.

Next, we find the optimum position of the sample relative to the incident light's focus through a "Z-scan" process. This scan mode exposes the sample to X-ray photons while moving the sample around the focus along the Z-axis, and the photoemission signal on the electron analyzer is recorded. The maximum count on the analyzer corresponds to the optimum z position. An example of the Z-scan result is shown in Figure 2.12. Then, this Z value is preserved during a measurement while we move the sample along the X and Y axes to use different regions on the sample for measurement.

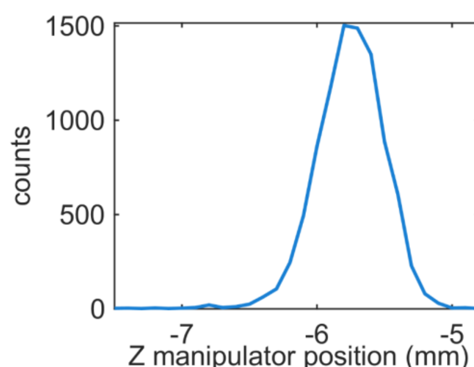

Figure 2.12. Example of a Z-scan measurement result. The intensity of photoelectrons is detected by the electron analyzer while aligning the sample's Z-position.

The electron analyzer is a hemispherical spectrometer with a channeltron detector which can detect the intensity of the impinging electrons and resolves their kinetic energy by mapping the energy of electrons to a position on the detector [129]. For TEY measurement, a picoammeter measures the drain current from the sample, as shown in Figure 2.11. In TEY mode, a bias voltage can be applied between the sample and ground to increase the efficiency of the electron detection. To meet the same purpose in XPS mode, a bias voltage can be applied between the sample and the analyzer.

A schematic from the BEAR beamline used for XPS and TEY measurement is shown in Figure 2.13 [130]. We briefly explain some of the key components of the beamline for our experiments. There are four insulated molybdenum photo emitting plates, named beam position monitor (BPM), located at the start of the beamline to monitor the position of the incoming beam. The drain current (I_{BPM}) from these plates also can be used to monitor the fluctuations in the photon flux coming from the storage ring.

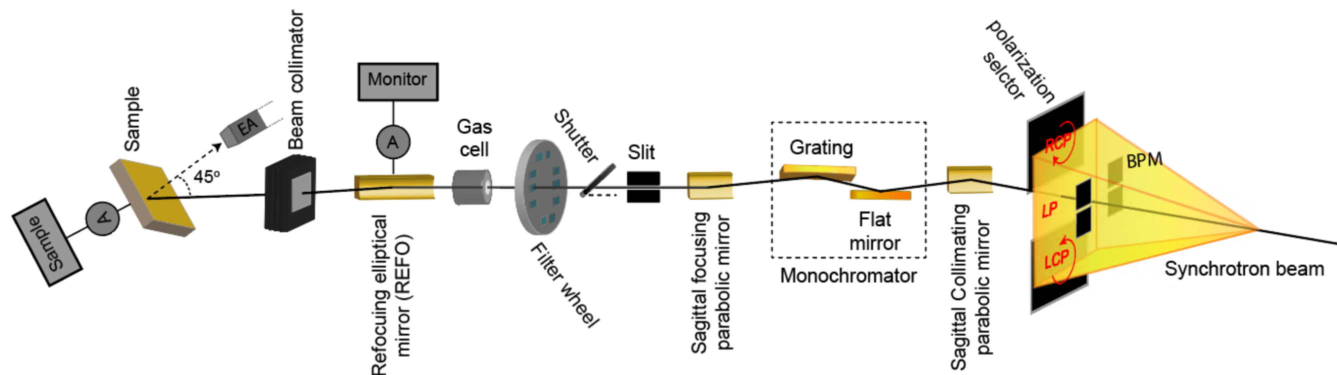

Figure 2.13. Layout of the BEAR beamline at the Elettra synchrotron. LP = linear polarization, CP = circular polarization [130].

Table 2.1. Filters used in the TEY measurement's energy ranges. No filters are used for energy ranges 24 - 37 eV and 100 - 200 eV.

SiO_2	LiF	In	Sn	Al	Si
3.9 eV	5.7 eV	12 eV	15 eV	37 eV	50 eV
7.8 eV	11.5 eV	17 eV	24 eV	72 eV	100 eV

The beamline radiation source extends over the range from 3 to 1600 eV. The setup embeds a combination of a mirror and a grating as a monochromator to select the wavelength of interest. Because of the wide energy range, a common problem with synchrotron radiation is the contamination of light of a wavelength λ selected with the monochromator by higher-order diffraction of radiation with shorter wavelengths λ/n ($n > 1$). The monochromator can operate with different angles between the flat mirror and the grating to maximize the total throughput, or to position the mirror in such a way that it reflects as little as possible of higher-order light. For further suppression of higher-order light, filters are used, as discussed below. In the case of our measurement, we used two gratings called GNIM and G1200, both with 1200 lines/mm. GNIM is set in the beamline's monochromator for diffracting energies in the range 5 - 45 eV and G1200 for the energy range of 40 eV to 1600 eV.

The light after the grating is focused onto a rectangular slit. The vertical slit width determines the wavelength resolution, the spot size in the vertical direction and it changes the number of incident photons. Therefore, we used the vertical settings in the measurements to adjust the incident power on the sample with changing the vertical slit size. The horizontal slit of spectrometer in our all experiments was set to its

maximum value (820 μm), giving a spot width of ~320 μm on the sample. The focus on the plane of the slit is then reimaged onto the sample by projecting optics, here an elliptical focusing mirror known as REFO located in the last part of the beamline before the sample. The drain current generated from this Zerodur platinum coated REFO mirror is used during the measurement to monitor the incident photon flux.

In addition to the higher-order suppression within the monochromator, filters can be used to block these undesired photons of higher energy (Table 2.1). For example, the quartz filter that is used for the energy range 3.7 – 7.8 eV does not transmit photons with energies > 7.8 eV that are present in the synchrotron radiation and pass through the grating in higher orders. In the ranges 24 – 37 eV and 100 – 200 eV no filter is used.

2.2.4 TEY experiments

2.2.4.1 Sample preparation for TEY measurement

The sample was prepared by spin-coating a photoresist film on a conductive 40 nm thick gold layer. The gold layer is sputter-coated on a silicon substrate, usually 2 × 2 or 2.5 × 2.5 cm^2, and 500 μm thick. A 5 nm Cr layer was used as an adhesive layer between the gold and silicon to minimize the imposed stress on the film due to lattice structure mismatch between gold and silicon. The spin-coating of the photoresist was performed with the same recipe described in previous works [73, 95].

2.2.4.2 TEY measurements

We performed TEY measurements in the incident radiation energy range of 5 to 150 eV. In this range, we can study the low energy photoelectrons from the valence molecular orbitals and Sn(4d) atomic orbitals in tin-oxo cages, which play a role in dissociation mechanisms upon EUV radiation. Later, we can compare the TEY spectrum with the absorption spectrum of the resist.

To obtain the complete TEY spectrum, we performed two sets of measurements. In the first one, we set the grating to GNIM, and the incident monochromatic energy on the sample was changed from 5 eV to 45 eV typically with steps of 0.2 eV. Using the G1200 grating, we recorded the TEY signal from 45 eV to 150 eV in steps of 0.5 eV in the second set of measurements. A fresh spot on the sample was used to record the TEY signal at each energy point. At each energy, we recorded the TEY signal continuously by exposing the sample over up to 120 shots to observe the evolution of the TEY data with increasing

exposure dose. Each shot corresponds to approximately 2 seconds of exposure. However, we should keep in mind that for a specific exposure time, the incident flux or dose is very different for different incident energies on the sample as can be seen in Figure 2.14.

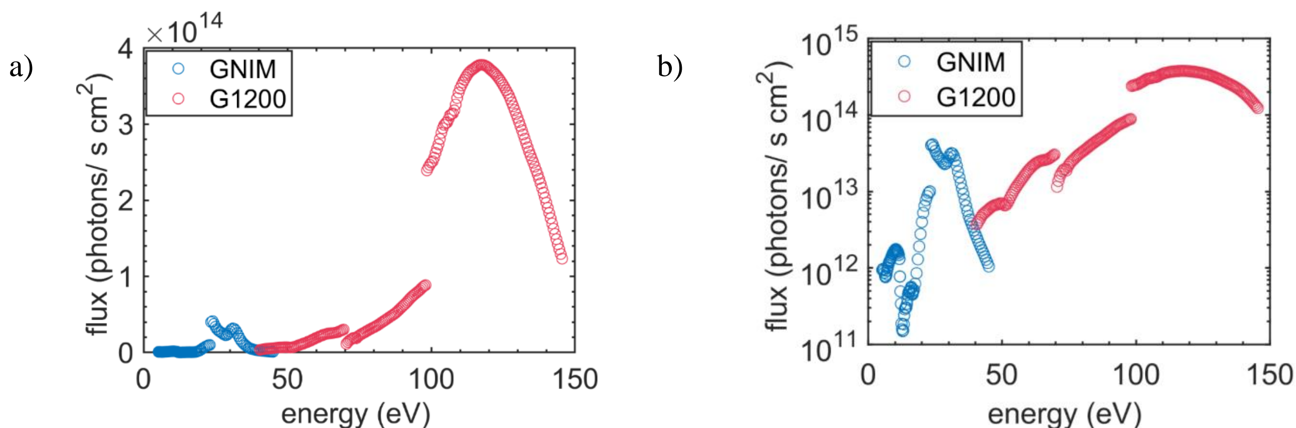

Figure 2.14. a) The integrated photon flux over the spectral bandwidth obtained with the slit width of 50 µm. The flux was calculated from equation (2.14) by measuring the reference diode (I_p). Blue and red plots show the flux for the two energy ranges measured using GNIM and G1200, respectively. b) The same but in logarithmic scale.

As shown in Figure 2.14, within the energy range of interest 5 to 150 eV, the synchrotron radiation flux is not uniform. The incident flux is noticeably higher for the G1200 energy range than for the GNIM energy range and markedly soars for energies above 100 eV.

The polarization selector at the start of the beamline is closed to the extent to only use the linear polarization light for performing TEY measurements. The underlying reason is to be able to see the evolution of TEY signal at initial exposure times at energies above 100 eV where the flux on the sample is very high.

The horizontal slit is set to its maximum value of 890 µm, but the vertical one in TEY mode is reduced to 50 µm. They are the typical settings used for TEY measurements in the BEAR beamline. The main reason for this setting is to make a good compromise between the spectral resolution and the dose of incident light on the sample.

2.2.4.3 Time resolved TEY measurements

As explained in section 2.2.4.2, the standard TEY measurements were performed over up to 120 shots with increasing exposure time on a single spot on the sample. Observing the evolution of TEY data with exposure, we decided to run a series of dedicated time resolved TEY measurement on the sample. In the

time-resolved TEY (TR-TEY) mode, we exposed the sample only at a few selected energies but for a much longer time to reach a reasonable dose on the sample, specifically at lower energies where the photon flux is relatively low (Figure 2.14). Then, the TEY signal was detected as a function of exposure time at the selected energies. We used fresh spots on the sample for the TR-TEY scan at each energy. The selected energies in G1200 region are nine values from 45 to 85 eV with spacing of 5 eV plus the 92 eV EUV energy. In the GNIM working range, we selected 23, 30, 35, and 39.5 eV. We also exposed the sample at 10 and 15 eV, but, unfortunately, the photon flux at these energies is extremely low so that we could barely expose the sample up to 40 mJ cm^{-2} and 15 mJ cm^{-2}, respectively. The results are discussed in Chapter 5.

2.2.4.4 TEY: data processing

The total electron yield $Y(E_{ph})$ (in units of electron per photon) is the ratio of the drain current I_S from the grounded sample to the photon flux q_P, equation (2.13), at the sample area, measured using a calibrated photodiode at the sample position. These two quantities are determined in separate scans over the photon energy E_{ph}. During both scans, the REFO mirror current I_m is measured, which allows the two measurements to be connected.

$$Y = \frac{I_s}{q_p} \tag{2.13}$$

By dividing the measured photocurrent of the reference diode I_p (which can be expressed in electrons per second) by its calibrated quantum efficiency Φ (electrons/photon) according to equation (2.14), we can convert the measured current to the flux in photons per second.

$$q_p = \frac{I_p}{\Phi} \tag{2.14}$$

Figure 2.14 shows the result of converting the I_R signal to the incident flux on the sample. To link the measurement of the sample's drain current and that of the photon flux, the current of the REFO mirror is recorded during both measurements. At each photon energy, the mirror current ($I_m$during the measurement, I_m^{cal} during the calibration run) is proportional to the photon flux (equation (2.15), in which a is constant).

$$q_p = aI_m = aI_m^{cal} \tag{2.15}$$

Combining equations (2.13), (2.14) and (2.15) we arrive at equation (2.16). The factor $I_m^{cal}\Phi/I_p$ is measured over the energy range of interest once during a beam time, and the ratio I_s/I_m is measured for each sample.

$$Y = \frac{I_s}{q_p} = \frac{I_s}{aI_m} \times \frac{aI_m^{cal}}{q_p} = \frac{I_s}{I_m} \times \frac{I_m^{cal}\Phi}{I_p} \tag{2.16}$$

The current measured by the BPM, I_{BMP}, located at the start of the beamline, can be used to monitor the variations in the beam. Since the BPM is located before the monochromator and the filters, it only accounts for the fluctuations from the Elettra ring current. Therefore, using I_{BMP} instead of I_{m} does not cancel out the variations induced by the instruments between the BPM and sample, such as optics and filters transmissions. In the 5 to 45 eV energy range, however, the measured I_{m} signal is small, and in this case, it is better to use I_{BMP} instead of I_{m} in equations (2.15) and (2.16).

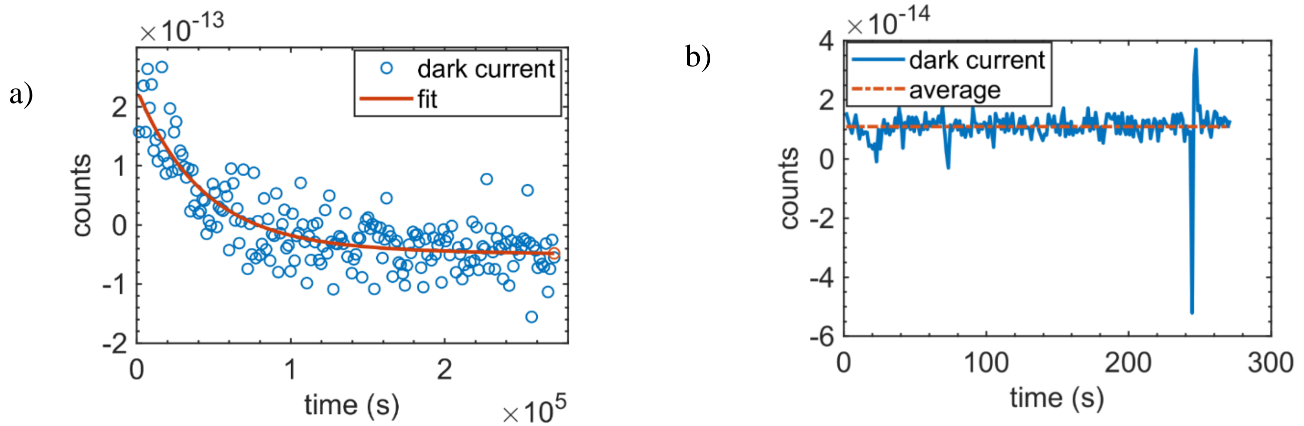

Figure 2.15. Example of dark current for the ammeters a) connected to sample, b) connected to the REFO.

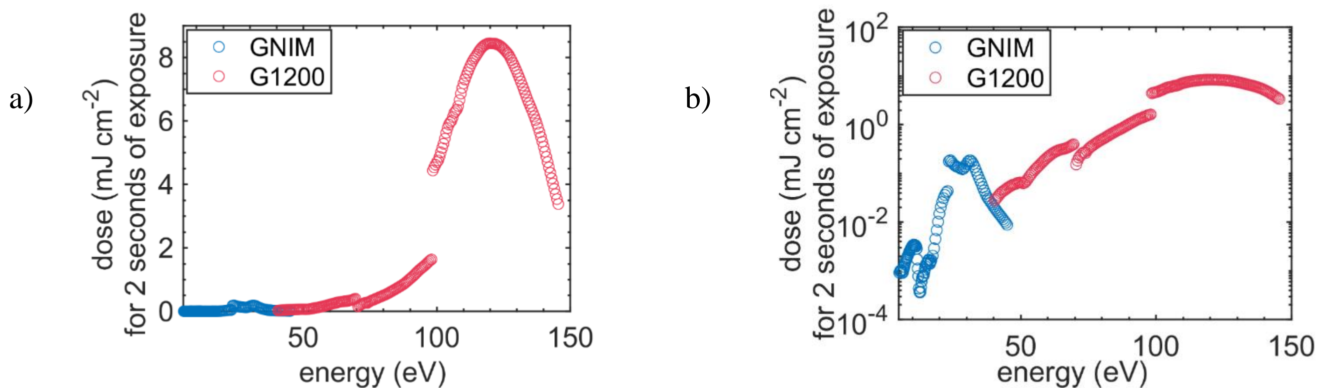

Figure 2.16. Incident dose on the sample at different incident energies over exposure time of 2s for vertical slit's width of 50 µm and linear polarization. a) linear scale, b) logarithmic scale.

To obtain correct current measurements, we need to subtract the dark currents for all the picoammeters mentioned above. The background signal originates from the random generation of electrons inside the detector, for example, due to heat or stray light. The dark current measurement is done simply by stopping the radiation into the beamline while recording the signals from the corresponding detectors for some time. It takes a while for detectors to reach stabilization; therefore, to record a proper background, the dark measurement time must be longer than the stabilization time of the instrument. In practice, the dark currents are negligible except for the measurements at low photon energies. Examples of the dark currents for the two detectors connected to the sample and REFO mirror are illustrated in Figure 2.15a and b, respectively. As we can see in Figure 2.15a, the ammeter connected to the sample takes a while to stabilize. Therefore, the measured dark current's data was fitted using a decaying exponential fit and the value at the plateau was considered as the dark value. For REFO mirror, the averaged value was used as the dark current, shown in Figure 2.15b with a red line.

The regular calibration of dose is performed by the beamline scientists for the incident energy of 92 eV, which is equal to 1.189 mJ cm^{-2} for the same slit dimensions used in the TEY measurements and 2 seconds of exposure. Therefore, the dose value for 2 seconds of exposure at other incident energies can be estimated as:

$$Dose(E_i) = \frac{flux(E_i)}{flux(92eV)} \times \frac{E_i}{92} \times 1.189 \tag{2.17}$$

In equation (2.17) E_i is the energy of interest, and the dose is in mJ cm^{-2}. The obtained dose values are shown in Figure 2.16 over the TEY measurement's energy range for 2 seconds of exposure equivalent to incident dose per shot. The exposure time for each shot of measurement is recorded in raw data files, and hence the irradiant dose on the sample for a certain exposure time can be estimated. Figure 2.17 shows processing steps of raw data from a TEY measurement. Figure 2.17.a is the raw measured drain current from sample, I_S. Part b in Figure 2.17 is the result after normalizing the measured I_s to I_m. Figure 2.17.c is the data after applying the TEY data processing method described in this section according to equation (2.16) and after removing the data points in the energy overlap ranges and smoothing the spectrum.

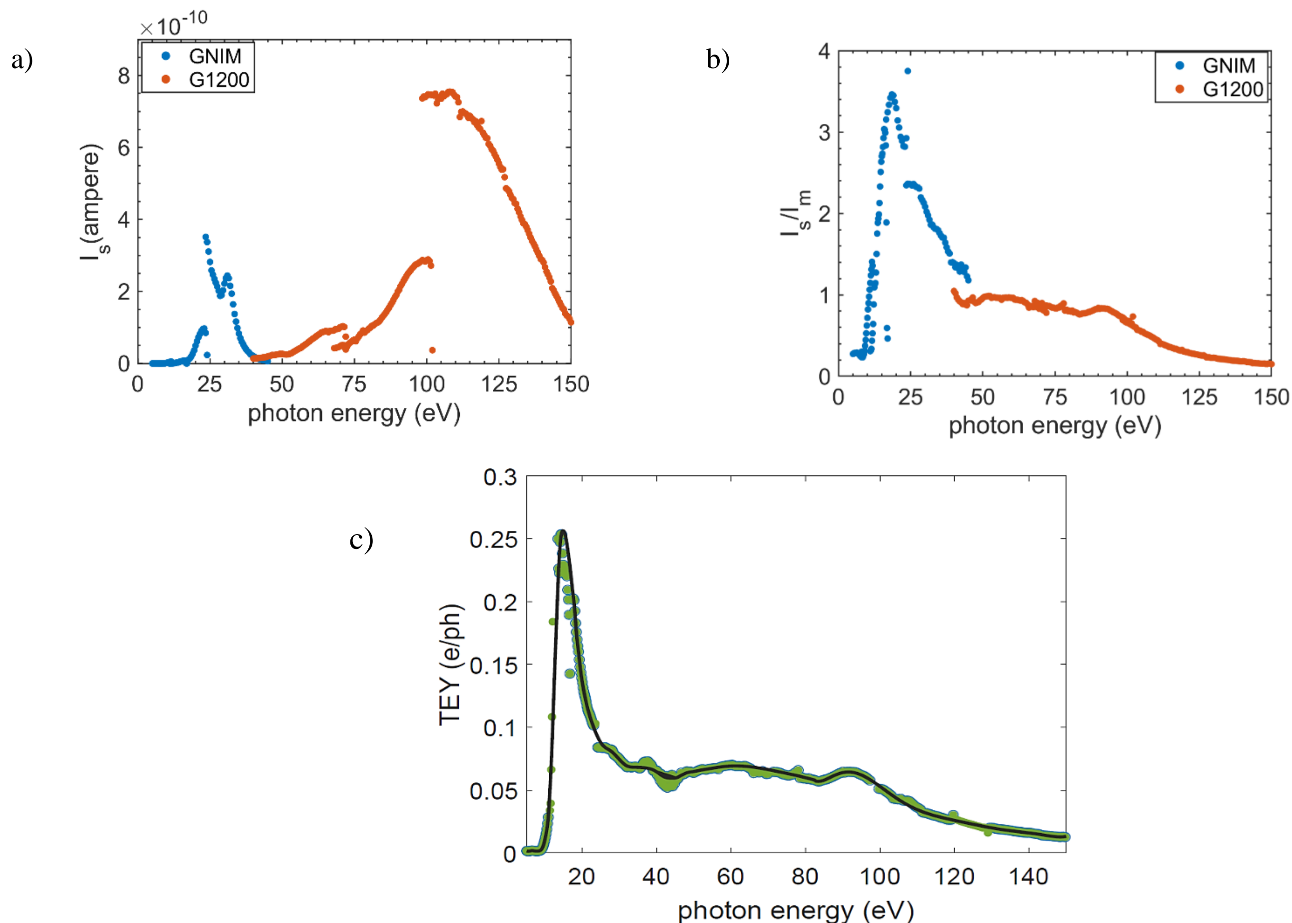

Figure 2.17. a) Example of raw data from a TEY measurement on TinOH sample, which is the measured drain current from the sample after dark subtraction. b) Ratio of the measured current from the sample to the one measured from the REFO mirror. c) TEY data after corrections, using equation (2.16).

2.2.4.5 Energy axis calibration

The sharp absorption edges of the different filters in the beamline are used as the benchmarks to calibrate the energy axis for the TEY measurements. To calibrate the energy range of 40-150 eV using the G1200 grating, we used $L_{2,3}$ absorption edges of Al and Si filters at 72.45 eV and 99.3 eV, respectively, as the references for the calibration. Similarly, the benchmarks in GNIM operating range are the edges of SiO_2, LiF, In, and Sn at energies of 7.75, 11.82, 16.55, and 23.75 eV, respectively. Figure 2.18 shows the absorption features measured for the calibration of energy axis. The data regarding each absorption feature is normalized to 1 to make the comparison visually feasible due to the nonuniformity of the flux at different energy regions.

Since the grating's diffraction is approximately linear in wavelength, we first convert the energy to wavelength. The calibration is performed by applying a linear fit through all the benchmarks. The obtained coefficients are used to calibrate the wavelength values in TEY measurement, which are then converted back into photon energy. As can be seen in Figure 2.18a and Figure 2.18b, the low energy values are not off in calibration, while a difference of ~2 eV can be observed for the high energy values between the default energy values set in the software and after calibration.

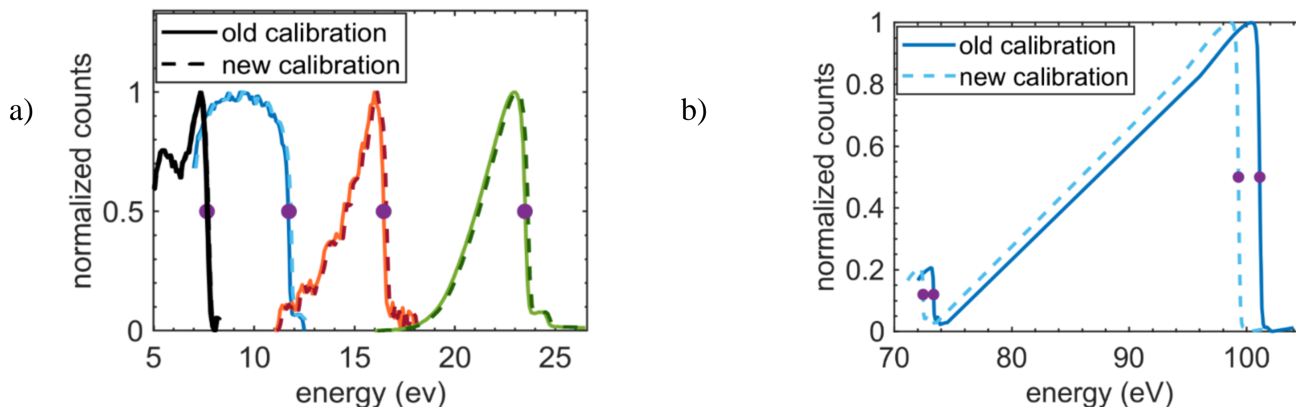

Figure 2.18. a) The absorption edges of different filters used to calibrate the energy axis in the energy range 5 - 45 eV. Different colors are representative of the measurements around different absorption features. Solid lines illustrate the energy values shown on the software. The dashed lines are the energy values after the calibration using the absorption edges. b) The absorption features to calibrate energy axis in 45 - 150 eV.

2.3 Ellipsometry

A commonly applied non-destructive optical technique to measure the thickness of thin films is ellipsometry. This is particularly attractive for photoresist films on very thin silicon nitride membranes, for which Atomic Force Microscopy (AFM) cannot be used. In this section, the basic principle of ellipsometry will be presented, as well as some results of the characterization of photoresists with this technique. For thin resist films on hard and strong substrates, AFM can be used to measure the surface profile and the thickness, using a scratch that locally removes the resist. For optical experiments, photoresists are spin coated on silicon nitride windows supported on silicon frames. The measurement of the film thickness on the thin SiN membrane is a challenge. AFM cannot be used here because the membrane is too fragile. In principle, it is possible to scratch the Si frame side of the membrane and apply AFM for thickness measurement. However, the thickness of the spin-coated film on the frame is different from the thickness value on the window and often suffers from nonuniformity issues due to the known edge effects, which gets more noticeable in the case of rectangular substrates [131, 132]. We observed higher thickness on the frame than on the window for the measured samples using ellipsometry.

We used the Woollam Variable Angle Spectroscopic Ellipsometer (VASE) at AMOLF. This has a large spot that is difficult to position precisely on the sample, so it can be used only for homogeneous samples. Some experiments were performed with a Woollam M-2000 located at ASML, which has imaging capabilities, so scanning of samples with SiN windows was possible.

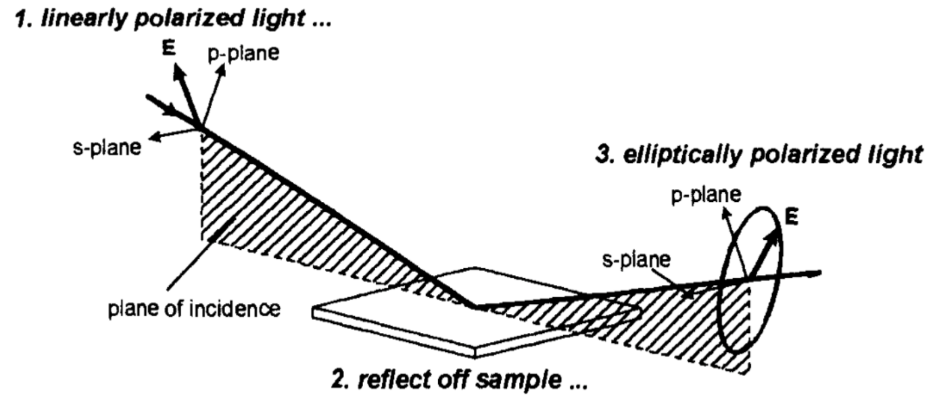

Figure 2.19. Interaction of a linearly polarized light beam with a sample, the principle which is used in ellipsometers. This image is taken from ref [133].

The ellipsometers measure the induced changes of S- and P-polarization components of a linearly polarized light beam after reflection from a substrate (Figure 2.19). The measurements are performed under one or more selected angles of incidence and as a function of incident wavelength (250 to 1500 nm). The result is typically presented in terms of the angles ψ and Δ as shown in equation (2.18):

$$\rho = \frac{r_P}{r_S} = \tan\psi e^{-i\Delta} \tag{2.18}$$

In equation(2.18), ψ is the amplitude ratio of P to S Fresnel components of the reflected light, and Δ is the relative phase shift [133-135]. The measurements were also done for three different incident angles around the Brewster angle of the material, which is the angle at which the maximum sensitivity can be achieved [136-138]. Typical ellipsometry data for TinOH spin-coated on a 500 μm substrate are shown in Figure 2.20.

In a general multi-layer material, the measured $\psi(\lambda)$ and $\Delta(\lambda)$ depend on the thicknesses of the different layers and on the complex refractive index values ($n(\lambda)$, $k(\lambda)$) for the materials. For many materials these parameters are known. For amorphous insulating materials such as the photoresists studied here, a Cauchy function in equation (2.19) usually gives a suitable description of the wavelength dependent refractive index in the UV-Vis and NIR spectral range.

$$n(\lambda) = A + \frac{B}{\lambda^2} + \frac{C}{\lambda^4} \tag{2.19}$$

The absorption coefficient $k(\lambda)$ can be obtained independently from a direct UV/Vis transmission measurement. The tin-oxo cages investigated here have a characteristic absorption band at 220 nm [73, 74, 139] but are transparent at $\lambda > 300$ nm.

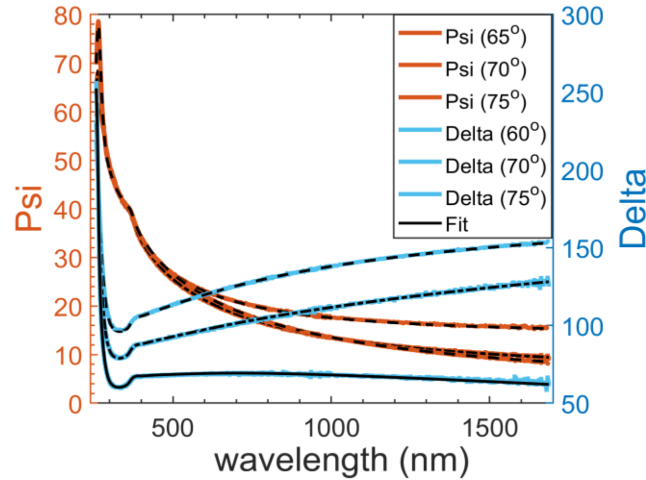

Figure 2.20. Ellipsometry data for TinOH on Si substrate. The thickness is found to be 38.9 nm.

We used the commercial CompleteEASE software [133] to perform the fitting on the measured $\psi(\lambda)$ and $\Delta(\lambda)$ values and obtain the $(n(\lambda), k(\lambda))$ and the sample's thickness.

Our ultimate goal of measuring the thickness of thin films on 30 nm SiN membranes is challenging due to the small reflection amplitude reaching the detector due to the high transparency of the SiN substrate and low reflection at the resist/SiN interface. Therefore, to be more precise in estimating thickness on membranes, we initially performed an ellipsometry measurement on a resist thin film coated on 500 µm silicon substrates, which provides a high signal. A Cauchy model on Si substrate was used for fitting in Figure 2.20 and deriving the n, k values for the resist which are presented in Figure 2.21. The obtained values at 632 nm wavelength are n=1.56, $k = 2.8 \times 10^{-4}$, respectively and the thickness of 38.9 nm. The thickness values obtained for thin films on silicon using ellipsometry were compared with the results from AFM for various thicknesses. The results between the two methods only differ by less than 2 nm, which is close to the precision of the measurement techniques. The resultant n, k values were saved and used later in the fitting procedure for the resist layer on the membrane.

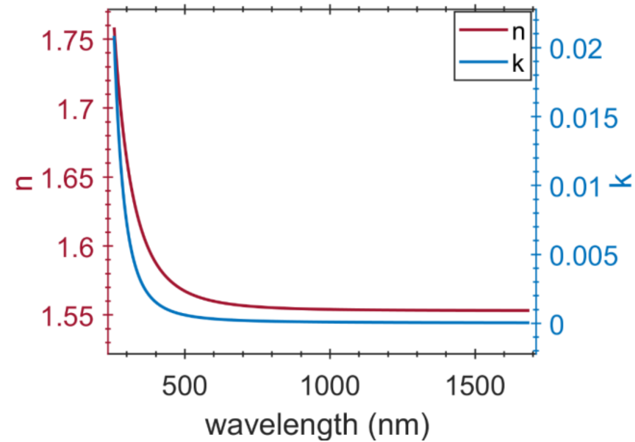

Figure 2.21. The obtained n, k values for TinOH resist by fitting the recorded ellipsometry data on Si wafer in Figure 2.20. These values were used for obtaining the thickness of the resist film on transparent membranes. Cauchy parameters for the fit are A = 1.54, B = 0, C = 8.3 × 10^{-4}.

The SiN membranes are fabricated on 500 µm thickness silicon frames. The Si frame as a reflective substrate makes the ellipsometry of the SiN on the frame area possible. In the second step, we performed ellipsometry on the available SiN on the silicon frames of an uncoated membrane to determine the *n*, *k* values of the SiN membrane material (Figure 2.22) resulting in n = 2 and k = 6 × 10^{-3} at 632 nm incident wavelength. The commercial membranes are made of "silicon-rich silicon nitride", which differs from the stoichiometry Si_3N_4.

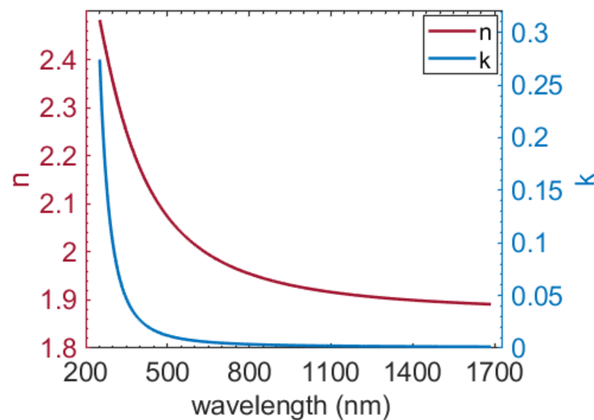

Figure 2.22. The *n*, *k* values for SiN on the frame of a neat membrane using a Cauchy model with parameters A = 2.217, B = 0.023, C = 6.7 × 10^5.

The thickness of TinOH on the frame can then be obtained using the model in Figure 2.23a. The model and parameters obtained in the second step for SiN on the Si frame (Figure 2.22) were used as fixed default settings for layer 1 and 2 in Figure 2.23a. For layer 3, we used the already saved parameters for TinOH on a silicon wafer (Figure 2.21). Therefore, the thickness of TinOH is the only variable to fit in this model.

Figure 2.24 shows an example of such fitting for TinOH on the frame, resulting in a thickness of 78.5 nm at the measured spot.

Figure 2.23. Illustration of the models used to fit the ellipsometry data for a) resist on the Si frame of the membrane. b) resist spin coated on top of 30 nm thick membrane.

Now we can determine the thickness of the resist on 30 nm membranes using the model visually shown in Figure 2.23b. In this model, Air ("void" in CompleteEASE software [42]) was used as the layer 1 beneath the membrane. The optical parameters (n, k) of the membrane and resist obtained from the previous fittings on Si substrates were imported into the software as the fixed values for layers 2 and 3, respectively. The thickness of the resist on the membrane is finally determined by setting the thickness as the only variable in the fitting, an example of the fit and ellipsometry data for TinOH on membrane is illustrated in Figure 2.25. The resist film shown in this example was relatively thick, 70 nm, which helps here to obtain high quality spectra and a good fit with the experimental data.

Although ellipsometry is a commonly used, and a potentially powerful method in thin film characterization, its application is often challenged by very inhomogeneous film thicknesses for the thin resist films coated on SiN windows on Si substrates. Unfortunately, the imaging ellipsometer was not available for routine use.

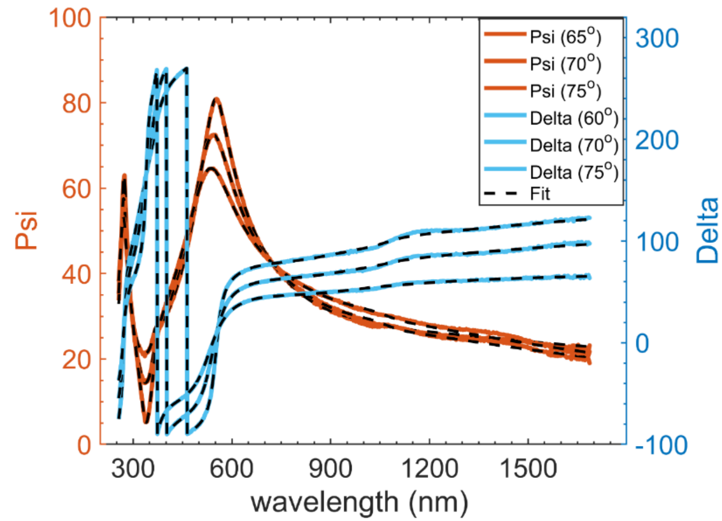

Figure 2.24. The ellipsometry data measured at three different incident angles and the corresponding fit for TinOH resist on the Si frame of the membrane using the Cauchy parameters in Figure 2.21. The measured thickness for TinOH on the frame at this spot is 78 nm.

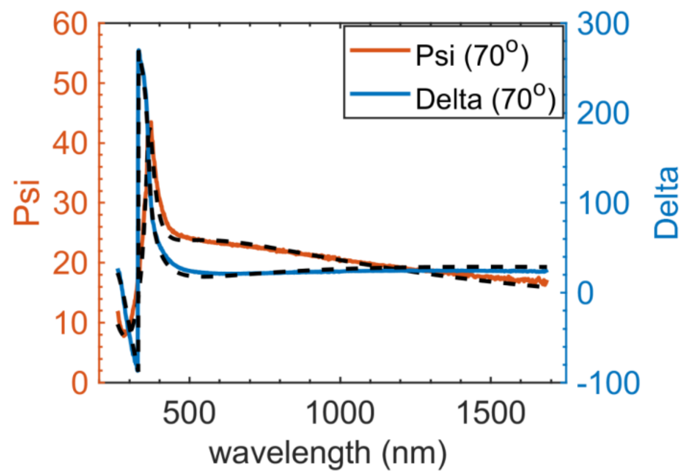

Figure 2.25. The ellipsometry results plus the fit for TinOH on the transparent window of the membrane which results in a thickness of 70 nm.

Chapter 3

XUV induced bleaching of a tin-oxo cage photoresist studied by high harmonic absorption spectroscopy[1]

Abstract

Inorganic molecular materials such as tin-oxo cages are a promising generation of photoresists compatible with the demands of the recently developed Extreme UltraViolet (EUV) lithography technology. Therefore, a detailed understanding of the photon-induced reactions which occur in photoresists after exposure is important. We used XUV broadband laser pulses in the range of 25 – 40 eV from a table-top high-harmonic source to expose thin films of the tin-oxo cage resist to shed light on some of the photo-induced chemistry via XUV absorption spectroscopy. During the exposure, the transmitted spectra were recorded, and a noticeable absorbance decrease was observed in the resist. Dill parameters were extracted to quantify the XUV induced conversion and compared to EUV exposure results at 92 eV. Based on the absorption changes, we estimate that approximately 60% of tin-carbon bonds are cleaved at the end of the exposure.

[1] This work was published in slightly modified form in: N. Sadegh, M. van der Geest, J. Haitjema, F. Campi, S. Castellanos, P. M. Kraus, and A. M. Brouwer, "XUV induced bleaching of a tin-oxo cage photoresist studied by high harmonic absorption spectroscopy," *J.Photopolym. Sci.Technol.,* 33, 145-51, (2020).

3.1 Introduction

Metal containing molecular inorganic resists are considered as promising materials for Extreme Ultraviolet (EUV) lithography, and their development is crucial for the success of this technology [140]. Compared to the traditional organic resists the metal atoms in the inorganic cores provide high etch resistance and high absorption cross sections, which may help to reduce stochastic noise. The small and well-defined sizes of molecular materials potentially allow small line edge roughness [51, 141-145].

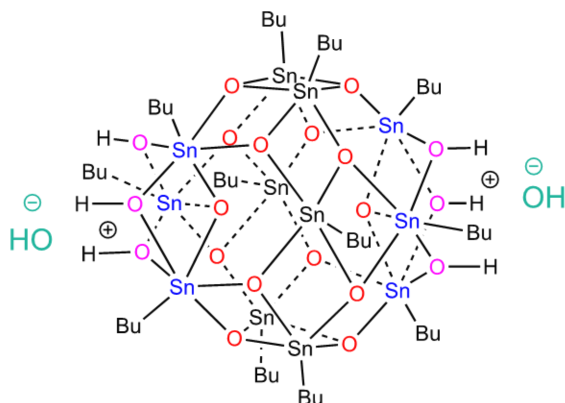

Figure 3.1. Tin-oxo cage with hydroxide counter ions (TinOH): $[(SnBu)_{12}O_{14}(OH)_6](OH)_2$.

Tin-oxo cages (Figure 3.1) are known as negative tone resists and the tin and oxygen atoms in the cage provide a high absorption cross-section of 13 μm^{-1} at the EUV wavelength (13.5 nm, 92 eV) [64]. In the compound investigated in this work (nicknamed TinOH), the twelve tin atoms in the cage have butyl groups as the organic substituents, and two $(OH)^-$ groups are present as counter ions [146, 147]. Cardineau et al. [71] were the first to study tin-oxo cages as EUV photoresists, and suggested that tin-carbon bond cleavage is the key step in the radiation induced reactions. This model is also supported by computational [73] and experimental studies in more recent work [95, 148, 149]. Hinsberg and Meyers [56] proposed a numerical model describing the reaction process in metal oxide-based resists.

According to this model, radiation initially leads to the photo-dissociation of ligands from the metal oxide cores, generating active sites on the metal atoms. The interaction of the active sites with each other leads to cross-linking of the cores through metal oxide binding, finally resulting in the solubility switch of the resist with exposure. In previous work, TinOH and related compounds were exposed to EUV, Deep UV (DUV), and electrons of various energies [64, 73-76, 150]. In the work presented here we used broadband extreme ultraviolet (XUV) pulses with energies in the range 25 – 40 eV to induce photoreactions in thin films of the tin-oxo cage resist, and to simultaneously study the transmission

changes. The XUV pulses were generated using a tabletop high harmonic generation (HHG) setup developed in our laboratory as the exposure source [151, 152]. The recorded absorption changes are quantified, and compared with the predictions from the CXRO database [96] and with EUV results in the literature.

3.2 Experimental

3.2.1 Sample preparation

TinOH films were spin-coated on free-standing silicon nitride (Si_3N_4) membranes (NORCADA; 30 nm thickness) [146, 147]. With the same spin coating method film thicknesses of 30 – 40 nm were obtained on other substrates [73, 150].

3.2.2 Experimental set-up and methodology

The general concept of the experiment relies on using a table-top HHG source to simultaneously expose TinOH samples and measure their transmission spectra. By carefully balancing the exposed area and thus the single-shot exposure dose with the collection efficiency of the spectrometer, we can achieve a continuous measurement of the TinOH transmission while simultaneously slowly photo-converting the TinOH cage in the thin film. Figure 3.2 shows a schematic drawing of the HHG set-up used for the XUV absorption measurements described here. It is an earlier version of the set-up described in detail in Chapter 2. Pressures inside the chambers were 10^{-8} to 10^{-6} mbar. An amplified Ti:Sapphire laser (Solstice Ace; Spectra-Physics) is used for generating extreme ultraviolet pulses by high-harmonic generation. The laser delivers 35 fs, 3.5 mJ pulses at 800 nm center wavelength with a repetition rate of 2 kHz. The fundamental beam is divided into two arms and one beam is frequency-doubled in a BBO crystal. The generated 400 nm beam is recombined with the remaining 800 nm subsequently. The combined beam is focused with a 50 cm focal length concave mirror into a gas cell inside the HHG chamber. An argon pressure of 25 mbar was used in the gas cell for this experiment. The interaction of argon atoms with the high intensity electric field of the laser pulse leads to the generation of high harmonics in the range 25 – 40 eV. The remaining 800 nm light is removed from the XUV pulses with an aluminum filter of 200 nm thickness located between the HHG source and the sample chamber, where the generated harmonics expose the prepared thin films. The XUV pulses were not focused in order to ensure a large illumination

area. The broadband transmitted light is directed to the spectrometer chamber where an XUV aberration-corrected concave grating (Hitachi, 1200 lines/mm) disperses the different harmonics onto an XUV charge-coupled device camera (GreatEyes). The TinOH resist coated on a silicon nitride membrane and an uncoated membrane were mounted next to each other on a motorized stage, and transmission measurements alternated between sample and blank with exposure times of 14.6 seconds.

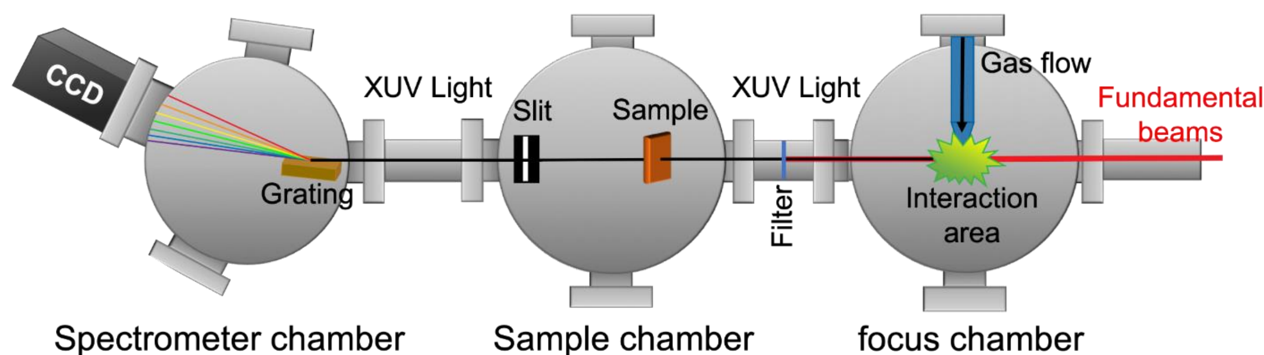

Figure 3.2. Schematic of the HHG set-up used for XUV generation. The red line shows the beam path of the fundamental beams, and the black path highlights the beam path of the generated XUV pulses.

3.3 Results

A typical high harmonic spectrum in argon generated in our setup is shown in Figure 3.3. The energy axis was calibrated using the diffraction equation of the grating. The spectrum includes both odd and even harmonic orders as it was generated with a two color (800 nm + 400 nm) driving pulse. The spectrum covers 20 – 48 eV, out of which the photon energy range from 25 to 40 eV has sufficiently high flux for measuring transmission changes. For the exposure and the simultaneous transmission measurements, the whole HHG spectrum was used. The entire exposure time covers almost 1000 cycles of repeated movements between the resist sample and the uncoated membrane to record the transmitted spectra.

Figure 3.4.a shows the evolution of the absorbance of the sample ($A = -\ln T$) as a function of exposure time. This graph includes all the absorption spectra obtained during each measurement cycle, while each absorption spectrum is smoothed using the lowpass filter as described in section 2.1.4.1. The final exposure time corresponds to an accumulated dose of ~1500 mJ cm^{-2}. The reported dose is only a crude estimate, and we are currently working on a dose calibration method to achieve a more precise value. The single-pulse exposure dose was roughly constant over time.

In Figure 3.4.b, the average absorbance over the 25 – 40 eV energy window is plotted with a smooth biexponential trend line. The absorption decreases from the initial $A_{0,av}$ = 1.1 to $A_{\infty,\mathrm{av}}$ = 0.73 extrapolated to infinite exposure time.

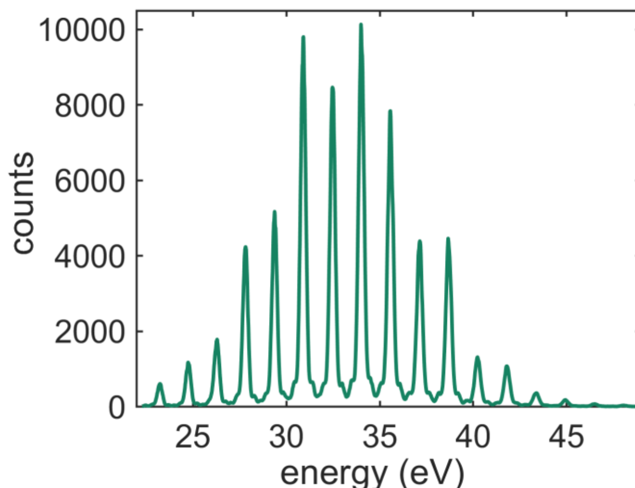

Figure 3.3. High-harmonic spectrum generated in argon recorded after transmission through an Al membrane.

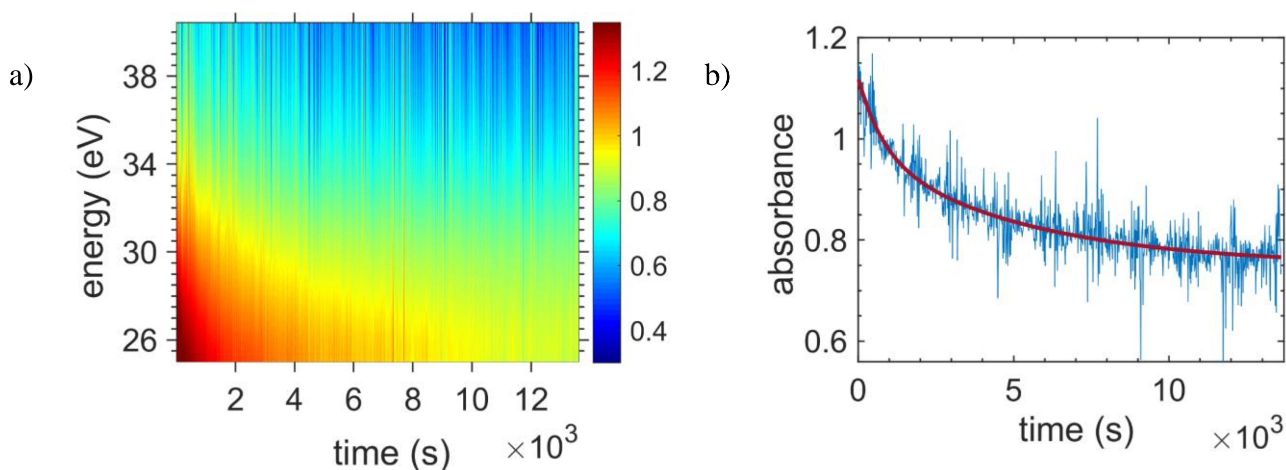

Figure 3.4. Spectrally resolved absorbance (color coded) exposed up to ~1500 mJ cm^{-2}. b) Spectrally averaged absorbance plotted as a function of exposure time. The fit function is a biexponential decay.

The experimental absorption spectra at the start (dashed red line) and end (dashed blue line) of the exposure time $A_0(E)$ and $A_f(E)$ are shown in Figure 3.5, together with the predicted spectra based on the scattering factors [96] at the beginning of exposure $A_{0,\mathrm{pred}}$ (red solid line), at the end $A_{f,\mathrm{pred}}(E)$ (blue solid line) and for $Sn_{12}O_{18}$ $A_{\infty}(E)$ (black line), which is the hypothetical end product after the dissociation of all butyl groups and the loss of all remaining hydrogen as water.

All spectra show a decrease of absorbance for increasing photon energy, which will be discussed below.

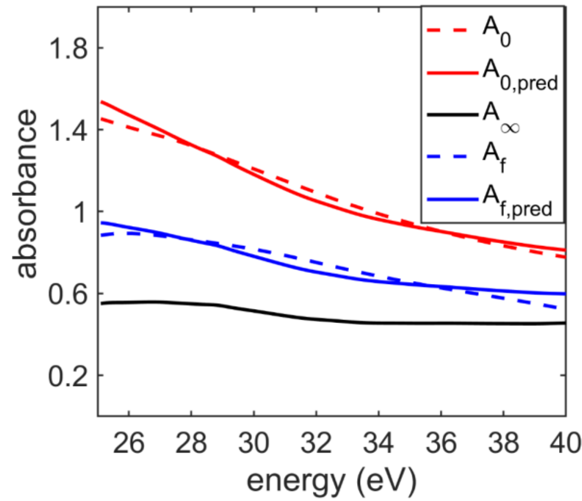

Figure 3.5. XUV Absorption spectra of TinOH resist film. Dashed lines are experimental spectra at the beginning (red) and at the end of exposure (blue). The solid lines are calculated from CXRO data [96]. The spectrum A_∞ is the predicted absorbance of $Sn_{12}O_{18}$.

3.4 Discussion

Using the CXRO database values derived from the atomic cross sections σ [96], the experimental spectrum at the beginning of exposure can be described according to equations (3.1) and (3.2).

$$A_0(E) = \sigma(E)_{\mathrm{T}inOH} \times S \tag{3.1}$$

$$S = \frac{\rho z}{M} \tag{3.2}$$

$A_0(E)$ is the experimental absorbance as a function of photon energy as shown in Figure 3.5, $\sigma(E)_{TinOH}$ is the predicted absorption cross section of $Sn_{12}C_{48}H_{116}O_{22}$ as a function of energy, S is the surface density of TinOH cages (in mol cm^{-2}), ρ the density of the thin film (in g cm^{-3}), z the thickness (in cm) and M the molecular weight (in g mol^{-1}).

We obtain the surface density of $S = 2.6 \times 10^{-9}$, from the measured $A_0(E)$ and predicted $\sigma(E)_{tinOH}$ in a single parameter fit, which results in a good match between the predicted and measured spectra as shown in Figure 3.5. The fitted value of S corresponds to z = 34 nm using ρ = 1.9 g cm^{-3}, which is a typical density found for various tin cage crystals [146, 147, 153]. This film thickness is in line with values for the spin-coated films on different substrates [150]. The good match between the predicted and

experimental spectra in Figure 3.5 also indicates that the tabulated values of the elemental cross sections in the energy range 25 – 40 eV are in good agreement with the experimental data, as was previously found for the EUV energy of 92 eV [64, 154].

The absorption decreases with increasing exposure time, which is attributed to the loss of butyl groups. We previously observed the loss of carbon-containing side groups with other types of electron or photon activation in tin-oxo cages [76, 148]. The hypothetical final product is $Sn_{12}O_{18}$, where all hydrocarbons dissociated ($C_{48}H_{108}$), and all mobile hydrogens are lost as water. In practice, not all butyl groups will dissociate. We plot the CXRO predicted spectra for $Sn_{12}O_{18}$ in Figure 3.5 as A_∞ (E), using the surface density of tin cages found for the initial film. The final measured spectrum $A_f(E)$ clearly indicates less than complete conversion.

By modeling the final experimental spectrum as a linear combination of the initial experimental and predicted final spectra, we estimate the fraction of conversion to be ~60% at the end of the irradiation period in another single parameter fit, i.e. ~60% of all butyl groups and cleavable water dissociated. The predicted final spectrum is shown as $A_{f,pred}(E)$ in Figure 3.5.

The absorption changes of photoresists are usually characterized in terms of the A, B, and C Dill parameters. To avoid confusion with the symbol for absorbance, we use the symbol A_{Dill}. A_{Dill} and B are defined according to equations (3.3) and (3.4) [4, 155]:

$$A_{Dill} = (A_0 - A_\infty)/z \tag{3.3}$$

$$B_{Dill} = (A_\infty)/z \tag{3.4}$$

The Dill C parameter is a measure of the rate of conversion, but due to the uncertainty in the exposure dose value in the present experiment, we do not discuss C in the present work.

A_{Dill}, usually given in units of μm^{-1}, represents the bleachable part or the exposure dependent absorption of the resist, and B defines the unbleachable part of the absorption. A_0 is obtained from the measured initial absorption spectrum, for A_∞ we use the predicted spectrum for complete conversion to $Sn_{12}O_{18}$. The linear absorption coefficient of a material α (μm^{-1}) is the sum of the Dill parameters A_{Dill} and B. These parameters are shown as a function of energy in Figure 3.6.

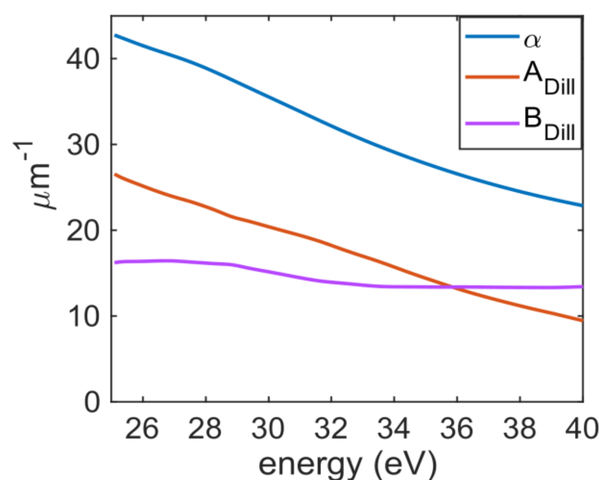

Figure 3.6. Dill parameters and linear absorption coefficient for TinOH in the XUV range.

It should be noted that the value of B is purely from the tabulated cross-sections, for α and A_{Dill} the values represent the measured spectral shape and they are scaled using the best fit of the observed spectra to the tabulated cross sections multiplied by the surface density.

The extrapolated change in absorbance averaged over the whole energy range in Figure 3.4.b suggests that at the end of the exposure time most of the maximum conversion has been reached. This would imply that the final product still contains more carbon and oxygen than $Sn_{12}O_{18}$ (Figure 3.5). On the other hand, the gradual decrease in the conversion rate with time renders the extrapolation based on a biexponential decay function uncertain. In our future experiments we plan to shed more light on the dynamics of the photobleaching process.

Fallica and coworkers reported the Dill parameters at 92 eV for several photoresists, including two tin based Inpria resists (the structures of which were not disclosed) [72]. They showed that the bleachable part A_{Dill} is much smaller than the unbleachable part B at 92 eV. For these two resists, the B parameters were 16 and 19 μm^{-1} while their A_{Dill} values were ~0.4 and ~0.7 μm^{-1}, respectively. For TinOH and related tin-oxo cages, EUV absorption values around 13 μm^{-1} were reported [64].

Comparing the present XUV results with the EUV reported values, the unbleachable parts in resists at XUV and EUV energies are similar. In the XUV, the bleachable part of the resist absorption is noticeably larger than at 92 eV.

While XUV and EUV radiation have in common that they cause electron ejection as the primary photo-process, the cross-sections and the selectivity for the ionization from different types of orbitals are different. Thus, XUV and EUV irradiation can be complementary tools in EUV photoresist research. The

absorption cross-sections of the tin-cage and its constituent elements between 25 and 100 eV are presented in Figure 3.7 [96].

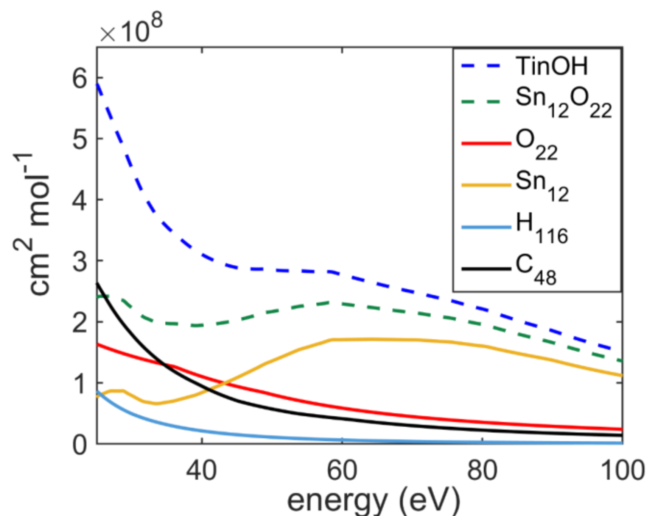

Figure 3.7. Photo-absorption cross-sections calculated from the atomic scattering factors from the CXRO database for $C_{48}H_{116}O_{22}Sn_{12}$ (TinOH) and its constituents [96].

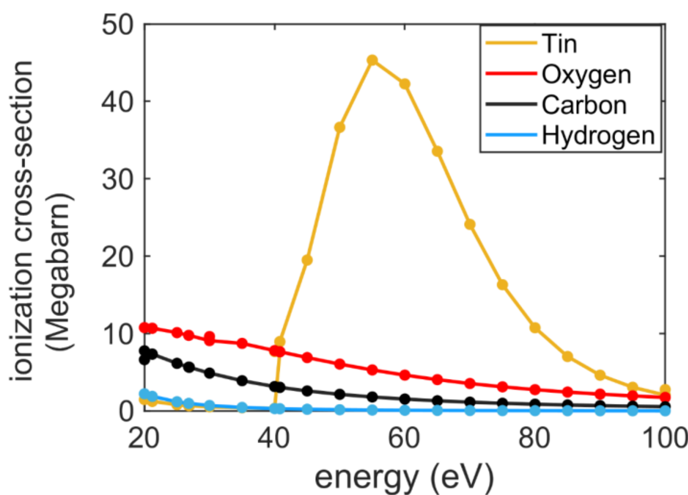

Figure 3.8. Photo-ionization cross-section for constituent elements of the resist [156, 157]

In the energy range <40 eV the absorption is large and mostly due to the valence ionization of carbon and oxygen. Therefore, the photo-induced outgassing of the butyl groups and some water molecules from the oxo metal cage are responsible for the absorbance decrease during exposure in the XUV. The cross sections in Figure 3.7 also explain why the absorbance decreases more for low energies during exposure (Figure 3.4.a and Figure 3.5), as carbon has a larger contribution to the absorption cross section at lower energies. At 92 eV, however, the absorption is dominated by the Sn atoms, primarily because of ionization from the Sn 4d level. Ionization from these atomic orbitals, with a binding energy of ~25 eV is

energetically feasible in the XUV, but the probabilities of exciting these 4d electrons are low and increase substantially only above 40 eV [156-158]. This is further illustrated in Figure 3.8, in which the computed photoionization cross sections are shown [156]. The large peak at ~60 eV is due to the Sn 4d electrons. Interestingly, recent experimental results indicate that the peak in the formation of Sn 4d photoelectrons occurs near a photon energy of 90 eV, rather than near 60 eV, as was calculated (Figure 3.8) [139].

3.5 Conclusion

We used a broadband XUV source from a high harmonic generation setup spanning from 25 eV to 40 eV to study the photo-induced absorption changes of a tin-oxo cage, which is a prominent candidate as photoresist in extreme ultraviolet lithography. We observed a strong absorbance decrease during XUV exposure that is attributed to XUV-induced tin-carbon bond cleavage. From the absorbance spectra we estimated a ~60% dissociation of all butyl groups for an exposure dose of roughly 1500 mJ cm^{-2}.

We extracted the Dill parameters A_{Dill} and B, which represent the bleachable and unbleachable part of the absorption. The bleachable part in the studied energy range is larger than in the EUV (92 eV). Compared to EUV exposure, the more pronounced XUV absorbance decrease during exposure was attributed to the photo-induced outgassing of the butyl side groups and some water molecules, which have larger XUV than EUV cross sections due to valence ionization of carbon and oxygen. In contrast, the 4d electrons in tin have a lower cross section in the XUV spectral energy range, but contribute more to the reactions at 92 eV exposure [159].

Our studies introduce table-top high-harmonic sources into the field of photoresist research for EUV lithography. The femtosecond to attosecond pulse durations of HHG sources [160] will make HHG table-top experiments an ideal tool for unraveling the primary steps in the photochemistry of EUV resists, as has been demonstrated on other targets before [161]. Extreme ultraviolet transient spectroscopy has shed light on the coupled electronic and nuclear dynamics in a number of molecules [162], transition metal complexes [163], semiconductors [164, 165], and metals [166] in the past. Our work paves the path towards using ultrafast transient extreme ultraviolet spectroscopy in complex inorganic materials in general and photoresists in particular.

Chapter 4

High harmonic absorption spectroscopy of tin-oxo cage acetate with XUV photons up to 70 eV

This chapter provides the results of the broadband high-harmonic absorption spectroscopy performed on thin films of a tin-oxo cage EUV photoresist with acetate counterions, nicknamed TinOAc. The absorption spectra are measured for the two energy ranges 22 – 40 eV and 42 – 70 eV, with high harmonics generated in argon and neon, respectively, as the exposure sources. The photo-induced changes in the transparency of the sample as a function of exposure dose are also studied for the two energy ranges.

The shape of the absorption spectrum in the range 22 to 70 eV matches very well with the predicted spectrum according to the CXRO database. The predicted tin N4-edge absorption feature is not apparent in the initial spectrum as it is masked by the strong contribution from the organic groups in the molecules but becomes clearer during exposure.

The photobleaching results are consistent with loss of the butyl side groups, which is the common process in tin-oxo cages using activation with electrons or photons with any energy >5 eV. Spectra are obtained of the Dill parameters representing the bleachable and unbleachable parts of the resist material. Bleaching is strongest in the low-energy range (<40 eV), where the absorption is largely due to the butyl side chains. At higher energies (42 – 70 eV), absorption is dominated by the tin atoms, and since these remain in the film after photoconversion, the absorption change in this region is smaller. It is estimated that after prolonged irradiation (up to 3 J cm^{-2} in the range 22 – 40 eV) about 70% of the hydrocarbon groups is removed from the film. The rate of bleaching is high at the beginning of exposure, but it rapidly decreases with time. This indicates that the first few Sn-C bonds are efficiently cleaved, but the photoproducts are less and less reactive as they have fewer Sn-C bonds.

4.1 Introduction

To understand the working mechanisms of photoresists for Extreme Ultraviolet Lithography it is important to use different analysis techniques and different electron or photon sources of activation. In these techniques, photon- or electron-based exposure sources with a diverse range of incident energies are used to obtain a thorough image of the induced reactions and their yield are compared with the results at 92 eV (13.5 nm), the wavelength of interest for the lithography industry. The main characteristic of EUV photons is that they ionize the material, generating electrons that mostly lose their kinetic energy by inelastic scattering, possibly generating electronic and vibrationally excited states, and releasing more electrons and holes. To understand the mechanisms at play, the optically allowed transitions in the energy range <92 eV have to be characterized. Moreover, when the energy is decreased from 92 eV down to the ionization threshold of ~8 eV (Chapter 5), ionization can still occur, but with lower and lower yields of secondary electrons. By studying the electron yield (Chapter 5) and the photochemical conversion in the XUV regime, the role of secondary electrons can be investigated.

The tin-oxo cages as potential EUV inorganic photoresists were already studied extensively in different works of the group using deep UV, EUV, soft x-rays, and electron beams at different energies [64, 70, 71, 75, 76]. In Chapter 3, we studied a tin-oxo cage with hydroxide counterions (TinOH) using a broadband XUV light source in the range of 22 – 40 eV, generated in a home-built HHG setup [167]. In the present work, we compare the results for a related compound, the tin-oxo cage with acetate counterions TinOAc (Figure 4.1) [70, 71, 168] and extend the energy range up to 70 eV. Acetate counterions are less nucleophilic and basic than OH^- [146] and therefore for practical purposes, TinOAc has an advantage over TinOH in terms of chemical stability and processability, but the radiation induced chemistry of the tin-oxo cage dication, which the two compounds have in common, will be essentially the same.

In addition to extending the energy range close to the commercially relevant EUV energy of 92 eV, we further developed the HHG setup and improved the spectrometer's resolution and the incident flux on the sample as explained in detail in section 2.1.1. These improvements in the setup can be observed by comparing Figures 3.1 and 2.1. The older version of the setup is shown in Figure 3.1 which was used to perform the XUV absorption measurements in Chapter 3 on TinOH. The improved version of the setup as the last update during this project is schematically shown in Figure 2.1 used for the XUV absorption measurements presented in this chapter on TinOAc. The new design of the spectrometer chamber provides a more precise relative distance and angle between the grating and the CCD, improving the measurement

resolution. The rotatory flange used to mount the CCD permits the detection of energies above 45 eV. The added focusing toroidal mirror increases the incident dose on the sample and improves the resolution further. The increased dose enabled high harmonic absorption measurements up to 70 eV with the generated harmonics in neon as the exposure source, which have one to two orders lower conversion efficiency than the generation in argon.

In this chapter, we used the approach mentioned in section 2.1.5.2, after measuring the beam spot size on the sample, to estimate the dose on the sample. Therefore, the bleaching results are also reported as a function of exposure dose. In the older version of the setup, the presence of the slit in the beam path to the spectrometer made the dose estimation approach less reliable than in the case of the updated setup, mainly due to the inaccuracy in the number of XUV photons lost at the slit position.

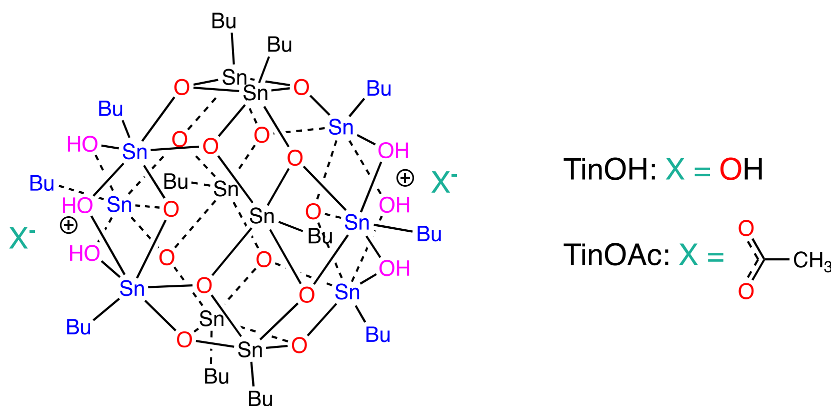

Figure 4.1. Structures of TinOH ($C_{48}H_{116}O_{22}Sn_{12}$) and TinOAc ($C_{52}H_{120}O_{24}Sn_{12}$).

4.2 Results

4.2.1 Tin-oxo cage absorption spectra in XUV energy range

Figure 4.2a and b show the number of XUV photons arriving at the sample position from the high harmonic generation in argon and neon, respectively, estimated using the approach described in section 2.1.5.2. These two harmonic spectra were used as the source of exposure for performing separate absorption measurements in the low-energy (22 - 40 eV) and high-energy (42 - 70 eV) ranges, from which the data throughout this chapter is presented. The argon and neon pressure were set to 20 mbar and 36 mbar, respectively. The numbers of photons correspond to ~ 0.2 nJ per pulse in the low-energy region, and ~ 4.6 pJ per pulse in the high energy range. The sample area was measured to be 1.2×10^{-4} cm^2 and

9.4×10^{-5} cm^2, these amounts to a power of 3.28 mW cm^{-2} and 0.096 mW cm^{-2} in the low and high energy regions, respectively.

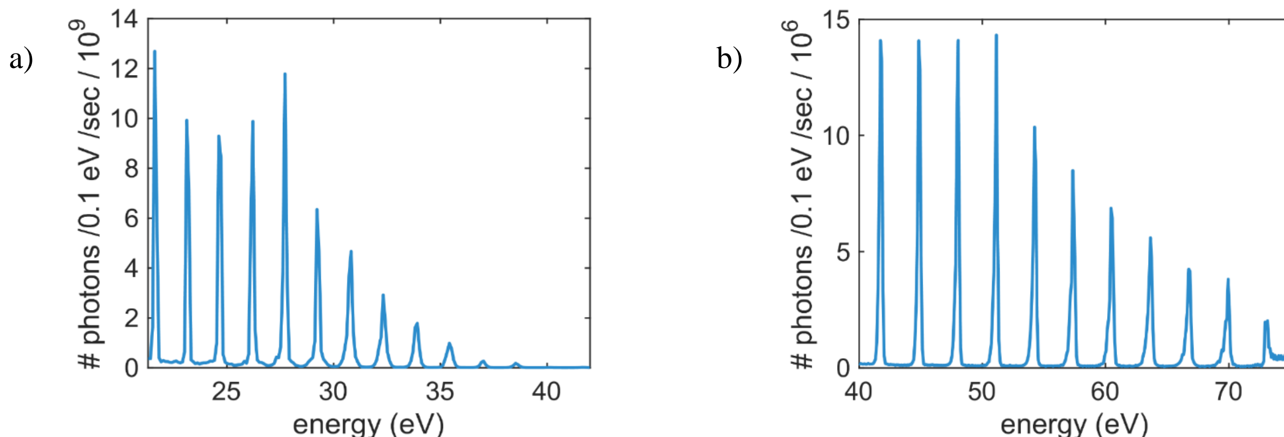

Figure 4.2. The number of XUV photons incident on the sample. a) For argon as the generating medium, and b) for neon.

Samples of TinOAc are spin coated from toluene solutions on silicon nitride membranes (3×3 mm^2 windows, 30 nm thick, on 7.5×7.5 mm^2 Si frames) [73, 150]. We used different samples for the experiments with the different energy ranges, and we obtained the results with two representative samples for each case. One set of data is shown in the main text, the other in the supporting information. The typical thickness of the thin TinOAc films is 30 - 50 nm, but there is some variation in different sample preparations, and the thicknesses could not be directly measured by independent methods for reasons explained in Chapter 2.3. Absorption spectra ($\mathrm{A} = -\ln(I_s/I_{mem})$) are obtained by alternately measuring the transmission of the XUV beams through the sample (I_s) and a blank SiN reference (I_{mem}) and absorbances are calculated at the peaks of the HHG spectra, as the intensities at energies in between the peaks are too low to obtain reliable data. In the present work, the exposure dose was calibrated in a more reliable way than the estimated values in Chapter 3. For more details see Section 2.1.5.2.

Figure 4.3 shows the experimentally determined absorption spectrum of the TinOAc films. As discussed in more detail below, it is based on the absorption data from separate measurements in the low and high energy ranges performed on two different TinOAc samples (Figure 4.4). The absorption data in the low energy range is normalized to the spectra at high energy around 42 eV and the whole spectrum is fitted to the predicted absorption spectrum for TinOAc from the CXRO database for a film of 45 nm [96], calculated from the atomic scattering factors of the elements in the TinOAc compound. For comparison, the predicted absorption spectrum of tin oxide (a 1:1 mixture of SnO and SnO_2, based on the assumed loss

of all organic and volatile material from TinOAc) is also added in Figure 4.3 as this is the hypothetical final product upon loss of all organic material and water from the cages. Overall, we can observe that there is a very good agreement between the shape of the measured absorption spectrum and the predicted one. There is a small feature around 24.5 eV in the absorption spectrum of TinOAc predicted using the CXRO database [96], presumably due to the $N_{4,5}$ absorption edge of Sn [169-171], but this is not clearly visible in the measured data before exposure.

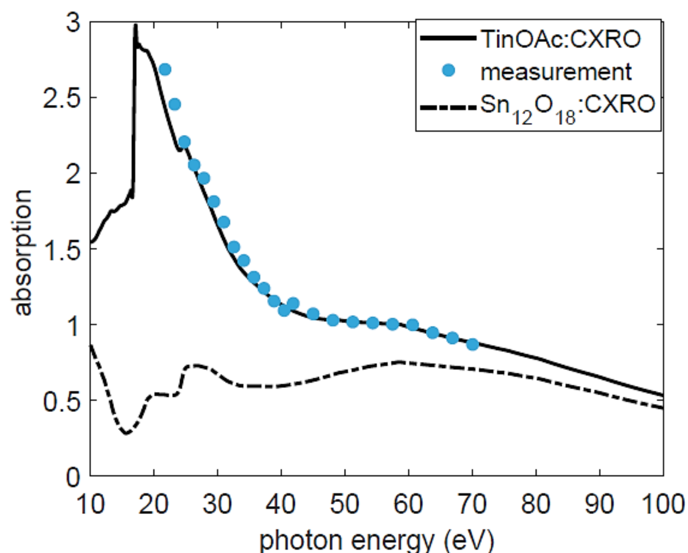

Figure 4.3. Comparison between the predicted absorption spectra and the measured initial absorption spectrum of TinOAc. The measured spectra for the low energy range normalized to the measured spectra for the high energy range around 42 eV.

4.2.2 XUV induced bleaching of tin-oxo cage acetate

The absorption spectrum of the resist plotted in Figure 4.3 is constructed from the recorded spectra at the start of exposure. To follow the induced changes in the spectrum of the resist with exposure time, selected spectra recorded during the exposure time are plotted in Figure 4.4a and b for the measurements in the low XUV energy range and the higher energy range separately for two different TinOAc samples (see Supporting Information for an additional set of data). In these graphs, the color change from blue to red depicts the transition of the initially recorded absorption spectrum to the final recorded one. The circles represent the actual data points from the measurement corresponding to harmonics' peaks in Figure 4.2.

The experimental absorption spectra in the high energy range (42 – 70 eV) suffer from lower signal-to-noise levels and therefore more recorded spectra are averaged (10 times) for presentation in part b of Figure 4.4 compared to the data in the low energy range. This is due to lower conversion efficiency in the

generation process of harmonics in Ne compared to Ar as can be seen in Figure 4.2 by comparing the counts for the two energy ranges in the measurement.

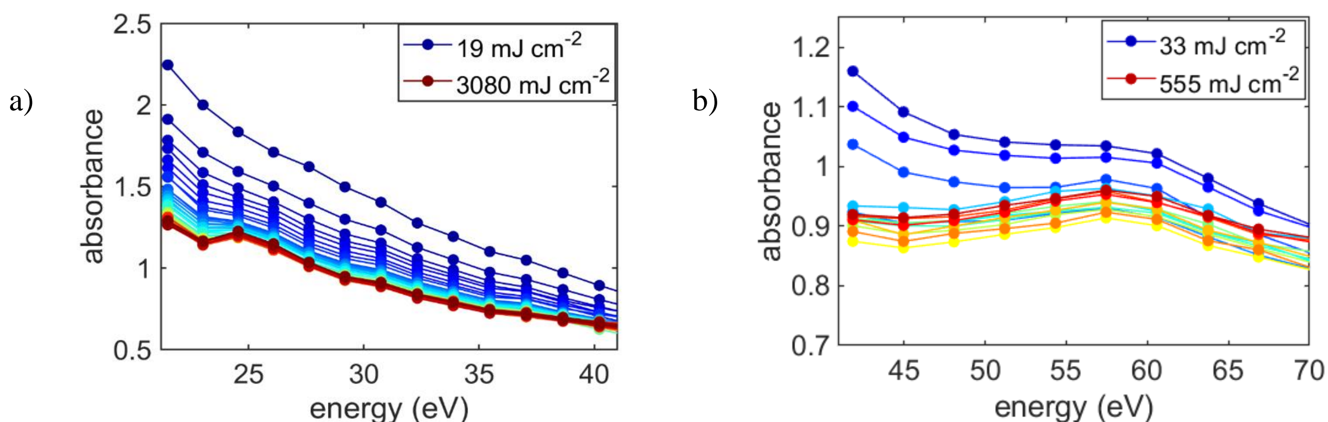

Figure 4.4. The evolution of the absorption spectrum of TinOAc for the two thin films used in the measurement. a) In the range of 22 to 40eV using high harmonics from Ar and the sample is exposed up to 3080 mJ cm^{-2}. b) Using the harmonics in Ne in the range of 42 to 70 eV and for the exposure dose up to 555 mJ cm^{-2}. The color change from blue to red corresponds to the increase of dose and the circles are the energies at the harmonics' peaks.

In Figure 4.4a, the sample is exposed up to 3080 mJ cm^{-2} and we clearly notice the evolution of the absorption feature at 24.5 eV with the increase in exposure time corresponding to the tin $N_{4,5}$ edge [169-171]. Referring to Figure 4.3, this feature in the predicted absorption spectrum of the resist is not as noticeable as the predicted one for tin oxide due to the contribution of carbon and hydrogen atoms to the absorption of the TinOAc sample. Therefore, at the beginning of the exposure the feature is masked by the strong absorption of carbon and oxygen. However, as exposure proceeds, more butyl groups dissociate from the tin cage structure in the resist leading to the decreasing contribution of carbon and hydrogen atoms in the absorption cross-section of the resist film. Therefore, the tin feature relatively grows and could be detected at longer exposure times.

In the energy range of 42 to 70 eV, Figure 4.4b, we can follow the gradual transition from the spectral shape of TinOAc to the spectrum of tin oxide(s) over the exposure time that corresponds to 555 mJ cm^{-1} incident dose on the sample. For the high energy range in Figure 4.3, we can see that the predicted TinOAc absorption spectrum reaches almost a plateau between 45 to 58 eV. Then it follows a decreasing trend for values higher than 58 eV. The turning point of 58 eV in Figure 4.3 comes from the peak in the absorption of 4d tin orbital at this energy as predicted from the CXRO data. This feature also becomes more visible (Figure 4.4b) with increased exposure time as the tin element contribution to the absorption spectrum of the resists grows with exposure due to the outgassing of carbon-containing materials. The two absorption features around 24 and 58 eV are small but were experimentally reproducible.

Considering Figure 4.4, we observe a decreasing trend in the absorbance of the resist with exposure time. The amount of the induced photobleaching continuously decreases when moving to higher energies.

We use the following data analysis approach to visualize the changes in the absorbance of the TinOAc samples over the entire exposure time in Figure 4.4 and quantify the resist's bleachable part. The recorded images (corrected for dark counts) for each measurement cycle during the exposure time are integrated over the energy axis for the sample and the membrane individually. Then we divide them by each other, as described in equation (4.1):

$$T_i = \frac{\int I(E)_{t_i,S} dE}{\int I(E)_{t_i,mem}\, dE} \tag{4.1}$$

Where i is the cycle number and T is the transmission. The integration is done over the energy axis. In the case of harmonics generated in argon we consider the energy range from 21.6 to 40 eV, where the harmonic peaks in the spectrum stand out from the background noise level, and 42 – 70 eV for the harmonics in neon. Therefore, plotting the T_i for consequent cycles from $i = 1$ to $i = n$, we can monitor the evolution of the sample's optical transmission with exposure time, as in Figure 4.5 for the two energy ranges. The data is fit with a biexponential function. The deviation from a simple exponential decay is to be expected, because the conversion rate decreases as more and more butyl groups are cleaved. Several factors contribute: decreasing absorption, change in efficiency of the reaction. Moreover, the light source is not monochromatic, and the absorbance is averaged over the whole spectrum.

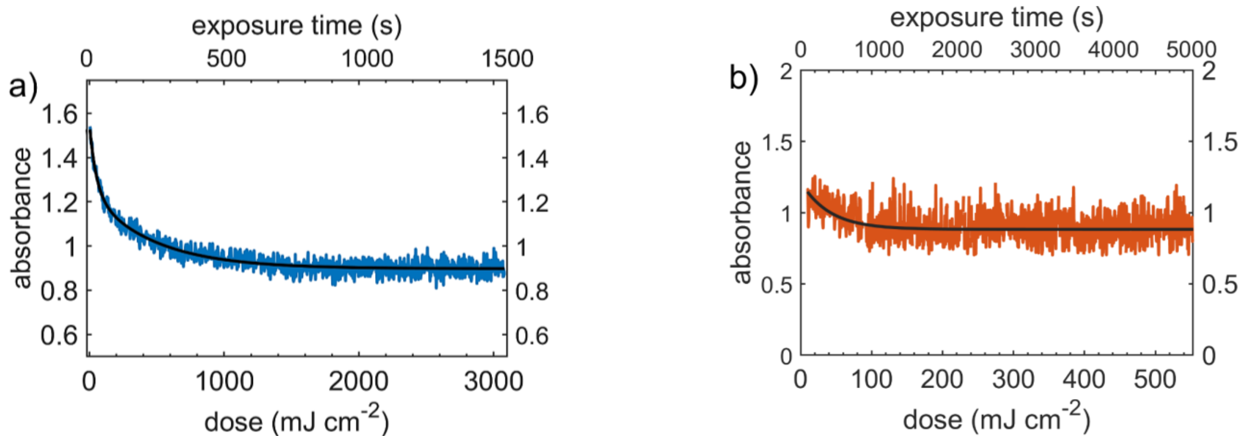

Figure 4.5. Spectrally averaged absorbance plotted as a function of exposure dose. The fit function is a biexponential decay. a) averaged over the energy range of 21 – 40 eV. b) averaged over 42 – 70 eV.

In Figure 4.5a, the average absorption decreases from the initial value $A_0 = 1.55$ to $A_\infty = 0.89$. A_0 is the extrapolated value for unexposed sample, dose equal to zero, and A_∞ is the value extrapolated to infinite exposure time. Figure 4.5b represents the bleaching trend of the average absorption (Figure 4.4b) in the energy window of 42 to 70 eV. The sample shows a bleaching with the ratio A_0/A_∞ =1.18. The average bleaching mainly results from the absorption change below 55 eV, as can be seen in Figure 4.4b.

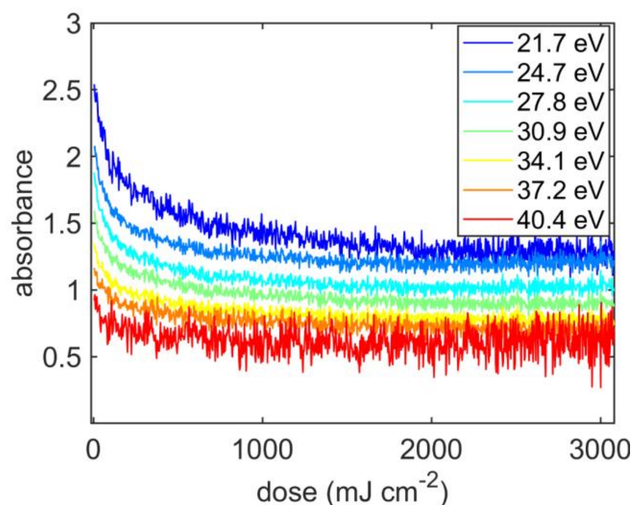

Figure 4.6. Bleaching of the TinOAc sample in the low energy range (21 – 40 eV) at some selected energies.

The energy dependency of the bleaching is further illustrated in Figure 4.6, where the absorbance change as a function of exposure dose is shown for selected harmonic energies, while the full broadband excitation is still responsible for the photobleaching.

4.3 Discussion

4.3.1 XUV absorption spectra of tin-oxo cage acetate

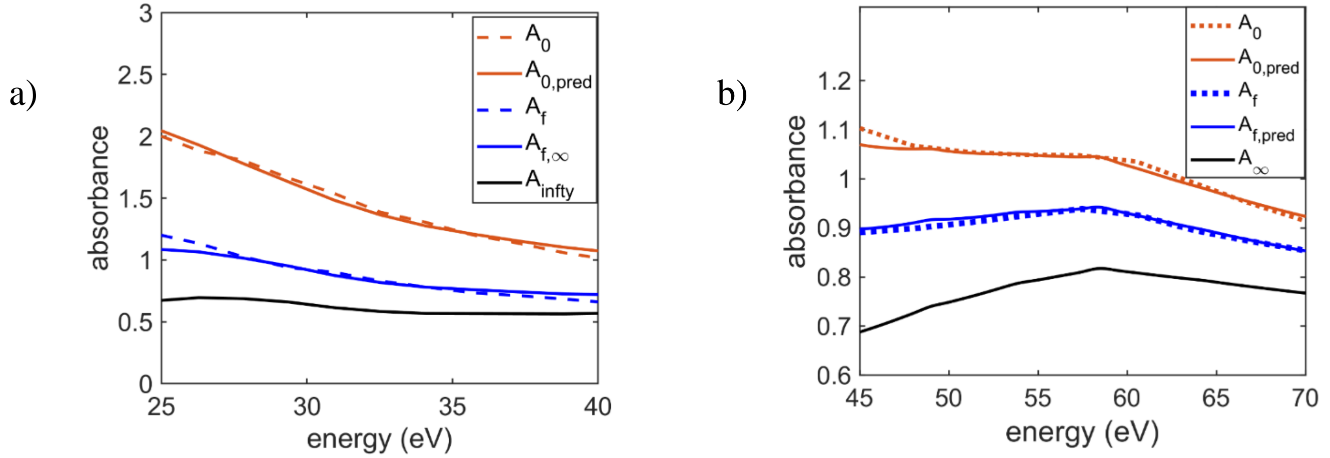

Figure 4.7. XUV Absorption spectra of two TinOAc resist films measured in the low and high energy ranges. Dashed lines are experimental spectra at the beginning(red) and at the end of exposure (blue). The solid lines are calculated from CXRO data using film thicknesses that give the best match with the experimental spectra. The spectrum A_{∞} is the predicted absorbance of $Sn_{12}O_{18}$. The end-of exposure spectra A_f are modeled as a linear combination of $A_{0,pred}$ and A_{∞}.

Following the same approach as in section 3.4, we re-plot the initial (A_0) and final experimental (A_f) absorption spectra throughout the exposure time (Figure 4.4a and b) in Figure 4.7 together with the predicted spectra at the beginning of exposure ($A_{0,pred}$) at the end of the exposure ($A_{f,pred}$). In this figure, A_{∞} is the predicted absorbance of $Sn_{12}O_{18}$ as the hypothetical final product after the cleavage of all hydrocarbons, the loss of acetate as acetic acid, and all OH groups as water according to equation (4.2).

$$Sn_{12}O_{24}C_{52}H_{120} \xrightarrow{h\nu} Sn_{12}O_{18} + 2H_2O + 2CH_3COOH + 12C_4H_9 \quad (4.2)$$

The measured initial absorption spectrum, A_0, can be constructed as the product of the absorption cross section of TinOAc and its surface density S (equation (4.3)), in which $\sigma(E)_{TinOAc}$ is the predicted absorption cross-section from the CXRO data. Then the thickness z of resist (molecular weight M) on the membrane can be estimated using equation (4.4):

$$A_0(E) = \sigma(E)_{TinOAc} \times S \quad (4.3)$$

$$S = \frac{\rho z}{M} \quad (4.4)$$

The density ρ of TinOAc films has not been determined experimentally. From the crystal structures of several butyltin-oxo cages, however, a typical density of 1.9 g cm^{-3} emerges [146, 172, 173]. Considering the initially measured absorption values in the Figure 4.7, a linear fit according to equation (4.2) result in very close values, $S \approx (3.48 \pm 0.3) \times 10^{-9}$ mol cm^{-2} and $S \approx (3.63 \pm 0.17) \times 10^{-9}$ mol cm^{-2} as the surface density for the two TinOAc samples used in the two separate measurements in low and high energy ranges. The given error bar originates from the variation in the obtained thickness values at different wavelengths. In Chapter 3, we obtained a surface density of 2.6×10^{-9} mol cm^{-2} for the measurement on TinOH due to the smaller thickness of the prepared thin film (34 nm). As already discussed in ellipsometry-related section 2.3, controlling the thickness of the thin films in the spin-coating process on small membranes (only 3 × 3 mm^2) to have thin films with very close thickness values for different measurements is challenging.

This surface density gives the average thickness (equation (4.4)) of 46 and 48 nm for the two resists samples used in the low and high energy measurements, respectively. These thicknesses of the films on the SiN windows are in good agreement with expectations based on the thickness of samples prepared in the same way on Si substrates, which could be determined using AFM. Furthermore, the absorption cross-sections of TinOAc and related compounds measured at 92 eV in ref [64] agree well with CXRO-based absorbance cross-sections. Therefore, we conclude that the CXRO data give a reliable description of the XUV-EUV absorption spectra of tin-oxo cages.

4.3.2 XUV induced photobleaching

The final spectra in Figure 4.7 can be modeled as a linear combination of the initial spectrum and that of the hypothetical product that has lost all organic material. Applying this model to the photon-induced changes in the absorption of TinOAc samples results in 70 % and 55% tin-carbon bond cleavage for the low and high energy measurements by the end of exposures, respectively. We see clearly less than complete conversion (cleavage of all butyl groups) at the ends of exposure with doses of 3080 mJ cm^{-2} in the low energy range and 555 mJ cm^{-2} in the high energy range. The data in Figure 4.5 show that the bleaching is fast at the beginning, but slows down rapidly, and appears to converge on a plateau at the later stage of the exposure. That is why we labeled $Sn_{12}O_{18}$ as a hypothetical product since the full conversion does not take place. In Chapter 6, we present measurements (Figure 6.7) of the outgassing rate of the carbon-containing products as a function of exposure dose at 92 eV. Also in that case, the major

outgassing and dissociation reactions occur at the beginning of exposure, and the resist outgasses at a strongly decreasing rate for higher exposure doses.

4.3.3 XUV versus EUV Dill parameters

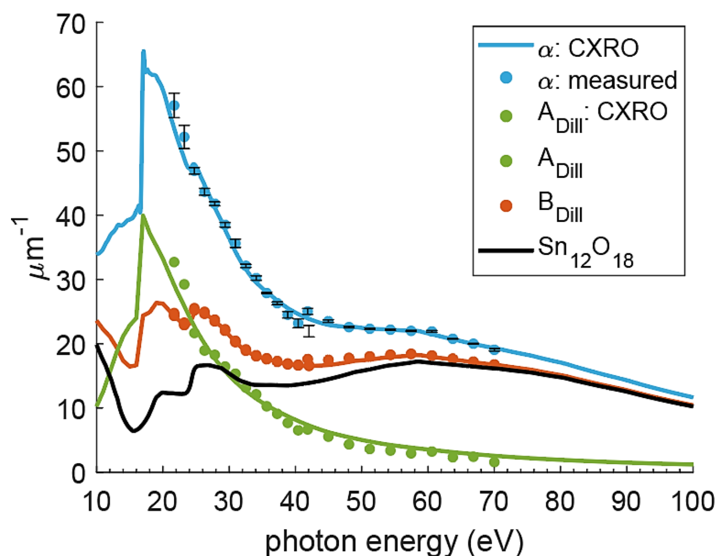

Figure 4.8. Experimental Dill parameters and linear absorption coefficient for TinOAc in the XUV range. The circles show the data points corresponding to the peak of harmonics in the measurement.

In the photolithography field, the so-called Dill parameters are used to characterize the bleachable and non-bleachable contributions (A_{Dill} and B_{Dill}, respectively) to the absorption coefficient $\alpha = A_{Dill} + B_{Dill}$ at the exposure wavelength [155, 174, 175]. In the present case, the sample is excited at multiple wavelengths simultaneously, but the chemical changes (butyl group loss) that occur upon prolonged exposure do not depend on photon energy. Therefore, A_{Dill} and B_{Dill} depend only on the probe wavelength, not on the excitation energy. Figure 4.8 illustrates the absorption coefficient α and Dill parameters obtained using equations (4.5) and (4.6) [4, 72, 155, 174]:

$$A_{Dill} = (A_0 - A_\infty)/z \tag{4.5}$$

$$B_{Dill} = (A_\infty)/z \tag{4.6}$$

In calculating the Dill parameters, we used the initial and final absorption values Figure 4.7. The values of A_{Dill} are slightly higher than those of TinOH (Figure 3.6) for the energy range of 25 to 40 eV, due to higher numbers of oxygen and carbon in TinOAc than TinOH. As discussed in section 3.4, α and A_{Dill} depend on the experimentally measured initial absorption values. As observable in Figure 4.8,

performing the absorption measurements up to 70 eV results in the extension of the given parameters that compatibly continue the acquired values of the low energy. The absorption cross-section of TinOAc was experimentally determined in ref [64] to be at 14.2 μm^{-1} at 92 eV. Using the obtained surface density values in section 4.3.1 and extrapolating the absorption cross-section to 92 eV in Figure 4.8 gives 13.5 ± 0.5 μm^{-1}.

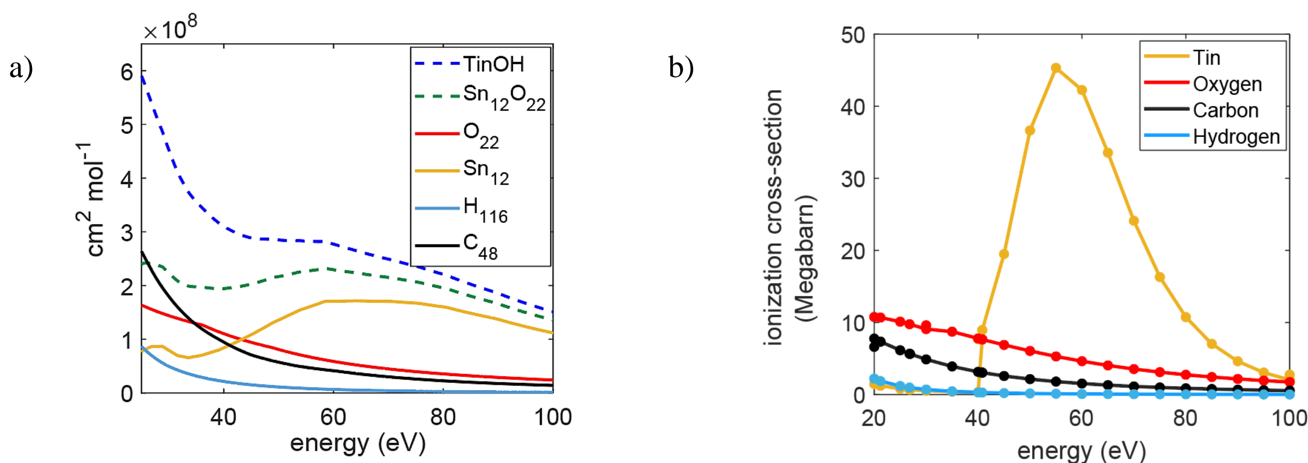

Figure 4.9. a) Photo-absorption cross-sections calculated from the atomic scattering factors from the CXRO database for $C_{52}H_{120}O_{24}Sn_{12}$ (TinOAc) and its constituents [96]. b) Theoretical photo-ionization cross-sections for constituent elements of the resist [156, 157].

Figure 4.9a shows the photoabsorption cross-sections of TinOAc and its constituting elements at photon energies in the range 20 – 100 eV. According to equation (4.2), butyl groups, acetic acid and water are the outgassing products after exposure. The cleavage of the butyl groups leading to different hydrocarbon products from the cage structure was also experimentally observed with time transient outgassing mass measurement at 92 eV (chapter 6) and other works in the group [95, 176]. Figure 4.9a shows that there is a decreasing trend in the photoabsorption of the atoms that can be lost by outgassing ($C_{52}H_{120}O_6$) from 25 eV to 100 eV, in agreement with the A_{Dill} parameter. As a result, the XUV absorption in the range of about 25 to 40 eV is very suitable for sensitive monitoring of the conversion of the resist.

In Figure 4.9b, we can see the ionization cross-sections of the atomic elements in the resist. Photoionization is the primarily initiated mechanism in the resist after photo absorption of energies higher than 20 eV. Therefore, both in EUV and XUV exposure, photoionization is mainly accountable for triggering the subsequent chemical reactions. From XPS studies (see Chapter 5 and ref. [139]), we know the binding energy of 4d tin orbitals to be 29 eV in TinOAc and similar tin-oxo cage compounds. At energies below 40 eV, the photoionization essentially occurs from the valence orbitals of the organic

atoms in the resist rather than from tin. In contrast, for energies above 40 eV, the photoionization from the 4d tin orbitals dominates and the excess energy can trigger cascades of secondary electrons.

While photons of different energy differ in the ultrafast primary activation mechanism, and in the number of reactions that a single photon can initiate, it is likely that the bond breaking reactions occur on longer timescales, in the relaxed radical cations, having a “hole” in the highest occupied molecular orbital (HOMO), and in the relaxed radical anions, having an electron trapped in the lowest unoccupied molecular orbital. For the intact tin cages, the HOMO is a sigma orbital between Sn and C and the LUMO is a corresponding sigma* orbital, which leads to facile bond breaking in both cases. The quick decrease in the reaction rate with conversion suggests that the primary reaction products, which have lost only few butyl groups, form less reactive radical ions. Haitjema et al. [74] proposed structures for the stable products that have lost two butyl groups, and these products have Sn atoms in a lower valence state, where the hole would be localized on a tin-centered orbital rather than on a Sn-C bond, which offers a tentative explanation for the lower reactivity.

4.4 Conclusion

TinOAc as a model of tin-based inorganic resist and an attractive candidate for EUV lithography was studied using high-harmonic absorption spectroscopy. The measurements were performed using broadband XUV photons in two energies ranges, 22 – 40 eV and 42 – 70 eV, from the high harmonic generation in Ar and Ne, respectively. The Dill parameters and absorption coefficients of TinOAc were obtained from the measured absorption spectra. The results over the 25 – 40 eV energy range agree well with the previous study for TinOH, while they are extended up to 70 eV.

For the measurements in the 22 – 40 eV range, we observe considerably larger photo-induced bleaching than in the range of 42 – 70 eV. The difference is due to the significant contribution of carbon atoms to the absorption in the lower energy range and the dissociation of butyl groups as the primary outgassing products with exposure.

For energies above 50 eV, the B_{Dill} prevails the A_{Dill} in the absorption spectrum of the resist. While in this energy range, the induced reactions are mostly triggered by photoionization of tin 4d orbitals and launched secondary electrons. The extension of the HHG absorption measurements 70 eV could be used as the complementary study at 92 eV since similar photon-induced mechanisms and explanations are expected at this energy.

The HHG setup is a time-efficient measurement technique for obtaining the overall shape of the absorption spectrum of samples over a broad energy range, while it consumes more time in synchrotron due to the monochromatic entity of synchrotron radiation. Our results in this study point to the potential of the homemade HHG setup for performing fundamental research on EUV photoresists. The harmonics' cutoff energy can be extended to higher orders by increasing the intensity and beam's wavelength, requiring a more powerful fundamental beam. Therefore, the current setup can be further improved to perform measurements at 92 eV on the resists, for example, by adding a chirp-pulsed amplification system to boost the power of fundamental IR.

Chapter 5

Soft X-ray photoelectron spectroscopy of tin-oxo cage EUV photoresists[1]

This chapter presents the results of total electron yield (TEY) and X-ray photon electron spectroscopy (XPS) on three tin-oxo cage EUV photoresist compounds, with the use of synchrotron irradiation in the XUV range as the exposure source.

The XPS measurements were conducted using incident photon energies within 50 – 135 eV to study the electrons in the Sn(4d) orbital with a binding energy of ~28 eV. It was observed that the number of emitted electrons decreases with the increase in the energy of incident photons above ~65 eV in agreement with the predicted photoionization cross-section of the Sn(4d) orbitals.

The TEY experiments were performed on tin-oxo cage derivatives TinOAc, TinOH and TinB by exposing the resist to monochromatic XUV photons with energies from 5 to 150 eV. Neglecting the differences in the relative electron yield intensities, we obtained very similar TEY spectra for the three tin-based compounds. To gain more assertion on the recorded TEY spectra of the resist, we also measured the TEY spectra for thin films of a resist sample coated on Si and Au substrates. The TEY of the substrates were also recorded individually.

The TEY spectra show that the resist's ionization starts at ~8 eV. Based on the assumption that in the XUV range, the TEY yield increases linearly with photon energy and the material's absorption coefficient, we estimate the generation of 3 – 4 secondary electrons per absorbed EUV photon. This agrees with expectation when it is assumed that the energy loss function (ELF) of the resists has a peak in the range 20 – 30 eV, like many materials for which it was measured.

[1] A part of this chapter was included in: N. Sadegh, Q. Evrard, N. Mahne, A. Giglia, S. Nannarone, A. M. Brouwer, "Electron generation in tin-oxo cage extreme ultraviolet photoresists," *J.Photopolym. Sci.Technol.*, 36, 373-378, (2023)

5.1 Introduction

The chip manufacturing industry has recently introduced Extreme Ultraviolet lithography technology to downscale the pattering of the fine features below 10 nm [177-180]. The transition from deep ultraviolet (196 nm; DUV) to the EUV wavelength of 13.5 nm has triggered the incorporation of metals in photoresists in the form of hybrid inorganic materials to increase the photon absorption cross-section and etch resistance of the materials [39, 50, 145, 181-183].

In DUV lithography, photons directly induce the desired solubility switch reaction mechanisms in the Chemically Amplified Resists (CAR) [184, 185]. Photons with energy of 92 eV, on the other hand, lead to the photoionization of the material. The primary photoelectrons lose their energy due to inelastic scattering, launching the secondary electron cascade inside the resist. Therefore, at the EUV wavelength, low-energy photoelectrons (0 – 80 eV) are mainly responsible for the resist's photolysis chemistry. The photosensitivity of the resist may be improved with optimized electron yields upon exposure, which is a factor of paramount importance in EUV lithography due to the relatively low throughput of the EUV light source [183, 186-191].

Tin-oxo cages are attractive potential EUV inorganic resists [66, 71] that provide a high absorption cross-section of ~13 μm^{-1} [192] at the EUV wavelength with experimentally demonstrated potential for nanopatterning. The photochemistry mechanisms in tin-oxo cages, mostly with n-butyl side chains, have been studied using different methods [70, 76, 139, 148, 192, 193]. The onset of electronic absorption in the tin cage thin films is at ~5 eV [74]. Photons with energy above this value lead to the dissection of the tin-carbon bonds between the cage structure and the butyl side groups. This Sn-C cleavage is assumed to be ultimately followed by the formation of intermolecular O-Sn-O bonds, leading to the condensation of the resist after exposure and the switch of the resist to insoluble form in the development step [56, 71]. The loss of butyl groups during the exposure has been confirmed in outgassing measurements (Chapter 6) [74, 95].

The Sn-C binding energy is typically around 2.2 eV [194], and electrons with similarly low energy can initiate the condensation reaction [76]. Therefore, optimizing the resist's performance requires studies to understand the origin of low-energy electrons in the resist adequately and also to gain a quantitative picture of the dissociation reactions driven by the low-energy photoelectrons, per EUV absorbed photons inside the resist. XPS measurements showed that under EUV exposure, primary photoelectrons originate

from the Sn(4d) orbitals and the valence orbitals of the tin-oxo cage [139, 148]. Our own experiments described in Section 5.3 extend this to the study of the low energy electron tail.

In this chapter, we first focus on Total Electron Yield spectroscopy (TEY) to investigate the contribution of the photoelectrons generated by photons with energies of 5 – 150 eV, which includes the EUV photon energy of 92 eV (wavelength 13.5 nm) [113, 114]. Technical details of the experiments, which were carried out at the BEAR beam line of the Elettra synchrotron, can be found in Chapter 2. We studied the tin-oxo cages with OH^- (TinOH), acetate (TinOAc) and tetrakis[pentafluorophenyl]borate (TinB) anions.

In TEY experiments, the sample is exposed to photons. The total number of emitted electrons (primary, secondary, Auger) from the surface is detected by measuring the induced current in the sample [124, 195]. TEY is a surface-sensitive technique since the inelastic mean free path of electrons is only a few nm. The primary electrons that are created too far below the surface cannot escape and do not contribute to the TEY. Only electrons with very low energy can travel larger distances and they do contribute to the TEY [112, 196-198].

TEY measurements are widely used (especially at incident photon energies above a few hundred eV) to study the near edge absorption fine structures (NEXAFS spectroscopy) [123, 124, 126, 196, 199]. Different studies have demonstrated a good agreement between the shape of the TEY measurement of the NEXAFS spectrum and the absorption of the materials close to the sharp absorption edges. The TEY measurement is commonly used as an indirect method for measuring the photo-absorption cross-section based on the simple assumption that the total electron yield is proportional to the product of the absorption coefficient and the incident photon energy as an average way to account for the amplification mechanism producing low energy electrons [200, 201]. From a more fundamental perspective, however, we observed deviations in the TEY recorded spectrum of the resist from the measured (Chapters 3 and 4) or predicted absorption spectra. Several factors need to be considered to interpret TEY data properly; for example, the electron escape depth [198, 202], the photon penetration depth [203, 204], and the density of states contributing to the TEY signal are all energy dependent[127, 205]. Some of these factors are discussed in this chapter.

For most TEY measurements, the resist is spin-coated on top of a conductive layer (gold) to avoid charging effects in the resist. The gold layer is sputter-coated on silicon. Few samples are also made by spin coating the resist directly on top of silicon substrates. We obtained similar spectra for the resist film

on gold with the one on top of silicon, excluding the possibility that the contribution of the holes created in the layers beneath the resist may be the reason for the observed deviations in the recorded TEY of the resist from the absorption spectrum. Additionally, we recorded the TEY spectra of gold and silicon as reference material and compared them with the reported ones in the literature [177, 199] to validate the measurement setup and the data analysis approach.

Before turning to the results on the tin-oxo cage photoresists (section 5.2.3), we first present and discuss the spectra of silicon and gold as reference materials in sections 5.2.1 and 5.2.2.

5.2 Results

5.2.1 TEY measurement on Si

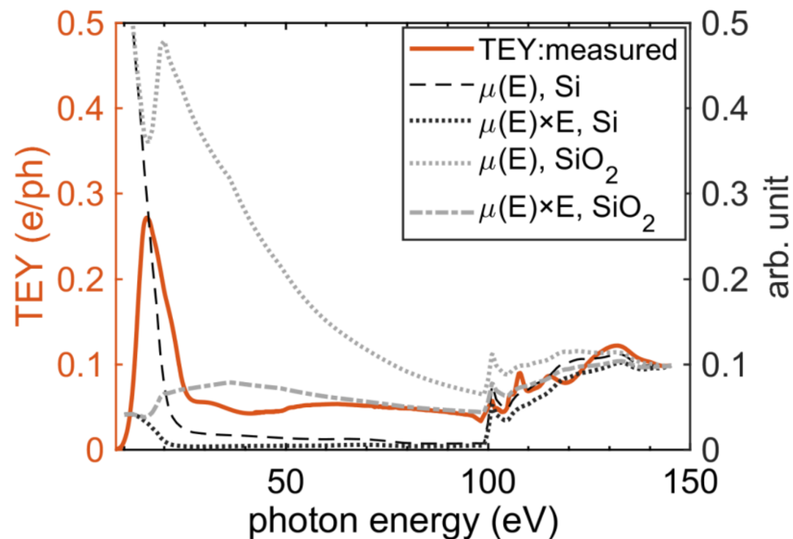

Figure 5.1. TEY spectrum of uncoated silicon wafer. The black and gray dotted lines represent the normalized result of the multiplication of the absorption cross-sections of Si and SiO2 [206] by the incident photon energy. All spectra were normalized to the measured TEY spectrum at 150 eV.

The red curve in Figure 5.1 shows the results of the TEY measurement performed on a piece of a silicon wafer (500 µm thick). The absorption spectra of silicon and silicon oxide from the CXRO database [206] are also added to the graph for comparison. Since the TEY is a surface-sensitive technique, in the case of forming an oxide layer on top of silicon, the electrons from the thin oxide layer that is usually present on silicon are likely to also participate in the TEY signal. In this graph, absorption values are calculated from the atomic scattering factors of the elements in the CXRO database. In Figure 5.1, we also

plot the absorption spectrum (CXRO) and the product of the two parameters: absorption and the photon energy for both Si and SiO_2.

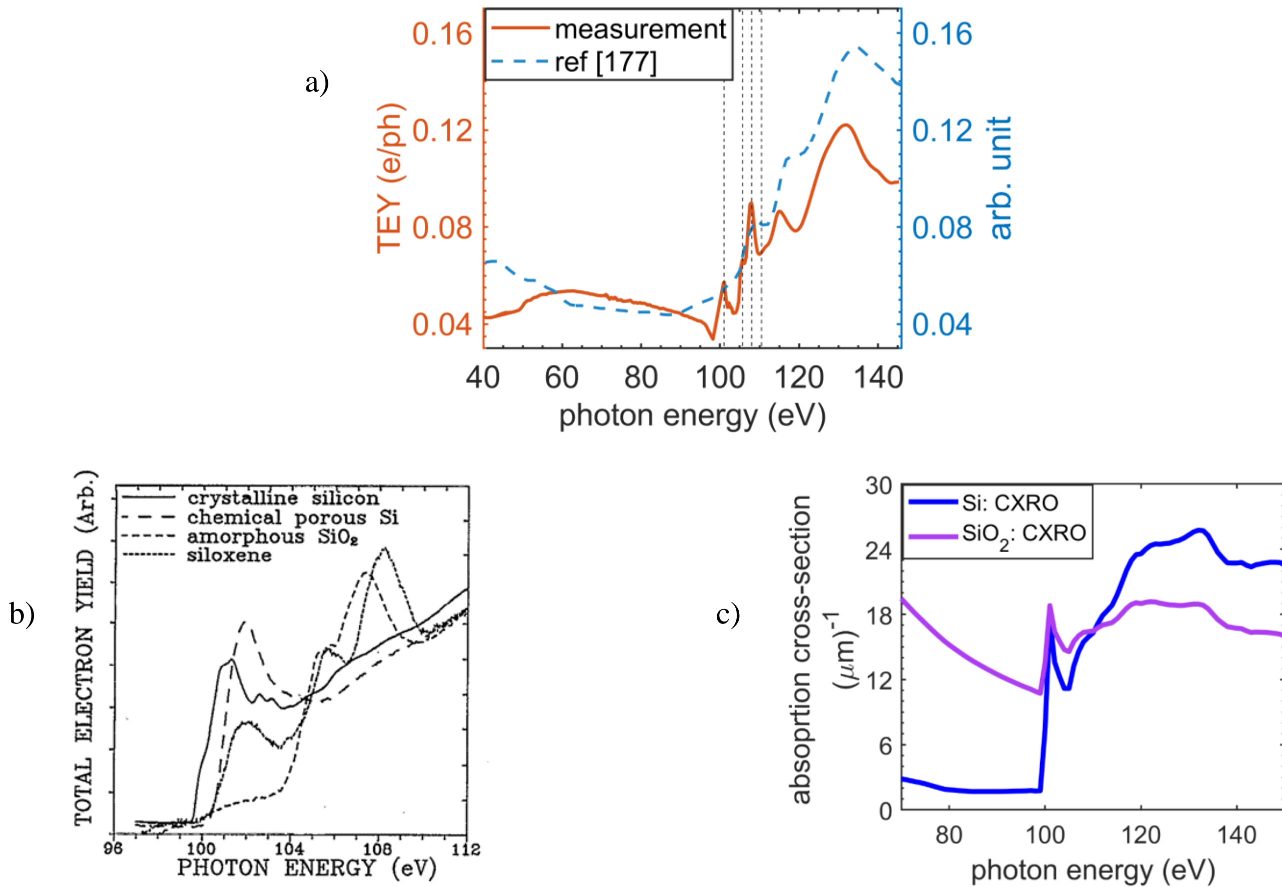

Figure 5.2. a) Comparison between the measured TEY spectrum with the one in ref [177] in the range of 40 to 150 eV. The TEY values from the reference are scaled to values close to our measured data to make a better comparison between the overall shape of the two plots. b) spectra from Dahn et al [207]. c) absorption cross section of Si and SiO_2 in high energy range, derived from CXRO data base.

Kitamura et al.[177] measured the TEY of silicon over the energy range of 40 to 150 eV. Their result is compared in Figure 5.2a with our measured data. Spectra in a small range around the L-edge are shown by Dahn et al. [207] (Figure 5.2.b). For better visibility, the absorption spectra of Si and SiO_2 from CXRO database are plotted in Figure 5.2c over the energy range of 70 – 150 eV. In this graph, there is a pronounced peak at 101 eV, which is visible in our measured spectrum as well, but missing in the data of Kitamura et al. Between 104 and 112 eV, Dahn et al. do not show any peaks in Si, but there are peaks in SiO_2 near 105 and 107 eV. Our data show a shoulder at 107 eV and a peak at ~110 eV, which may be attributed to the oxide. At ~115 eV and ~135 eV two broad features are found in our spectrum and that of Kitamura's team. The feature at 135 eV is apparent in the reported absorption cross section of Si from

CXRO in Figure 5.2.C, and less noticeable at the presence of oxide layer. Additional experimental data of the TEY of silicon in the energy ranges < 40 eV and > 115 eV unfortunately have not been found in the literature.

For the lower energies, the predicted spectrum of Si shows negligible absorption between 20 and 99 eV, and thus a low TEY signal is expected. We attribute the signal that we observe in this range to the SiO_2 surface layer, attesting to the surface sensitivity of TEY. The TEY signal increases at the $L_3(M_2)$, $L_2(M_2)$ silicon absorption edge around 100 eV. Both Si and SiO_2 absorb strongly, which explains the band at ~16 eV, of which the onset is at ~8.5 eV (first ionization energy of silicon from 3p orbitals). We note, however, that carbon contamination could also contribute to the signal due to the strong VUV absorption of carbon-containing molecules in this range.

5.2.2 TEY measurement on Au

The result of the TEY measurement on neat gold is presented in Figure 5.3. The absorption cross-section of gold (σ_A from CXRO) and its theoretical ionization cross-section σ_I are added to the graph. The TEY data does not start at zero at 5 eV compared to the observation for Si as the work function of gold is almost 4.5 eV. The measured TEY intensity for Au is very low compared to that of silicon (on average, it is almost half of the TEY signal of Si), although the ionization and absorption cross sections of Au in the range of 20 – 100 eV are higher than those of Si. In gold, the electron density is very high, which reduces the escape probability of electrons. In general, the escape probability of electrons in metals is smaller than in semiconductors and insulators due to the stronger electron-electron scattering at low kinetic energies [112].

In Figure 5.3, some of the detected absorption features are labelled. The broad feature around 65 eV and the small one at 78 eV result from the absorption of photons leading to ionization of electrons from the Au(5d) orbitals. The two small peaks at 85 and 88 eV are connected to Au's N6 and N7 edges (4f orbitals). In the range 60 – 150 eV, although both the absorption and ionization cross-section of gold drops rapidly, a larger number of electrons is emitted from the surface due to secondary electron multiplication. For the incident energies above 60 eV, the excess energy of the ionized 5d electrons is lost through the secondary electron cascades, and only above 120 eV, the 4f electrons start to take the role in the cascade generation. The maximum probability of ionization from the 5p orbital is located within 24 – 45 eV, which could be the reason for the detected broad feature around 35 eV.

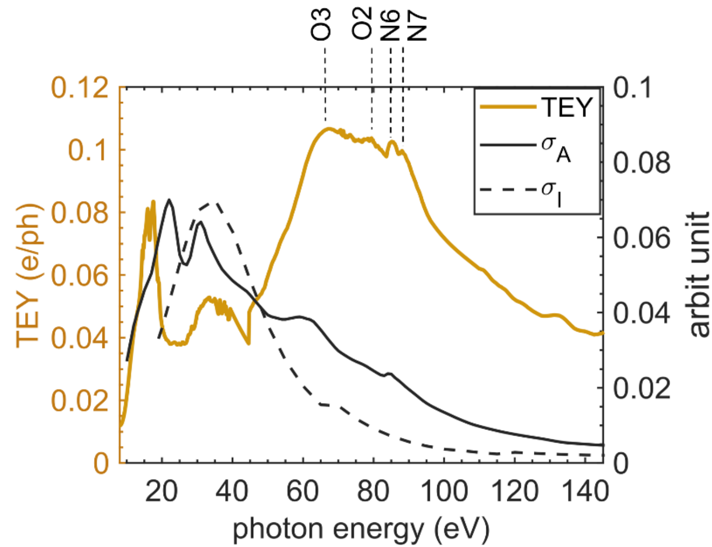

Figure 5.3. TEY spectrum of gold in the range of 5 – 150 eV (gold color). The absorption cross section (σ_A) and ionization cross section (σ_I) spectra of gold are also plotted in solid and dashed black lines, respectively. The σ_A and σ_I curves are normalized to the TEY value at 16 eV.

In Figure 5.4, we compare the measured Au TEY spectra and the secondary electron result for Au published by Henneken et al. [199], normalized to our measured data at 60 eV for better visualization. Except for a minor energy difference between the two spectra, a fair agreement between them could be observed. In our measurement, we could also resolve the Au(N6,7) edges from each other.

The photon attenuation length (L_{eff}) of Au is shown in Figure 5.5.a. As can be seen until 50 eV, Au absorbs the incident photons strongly so that the photons can only penetrate the sample up to 6.5 nm under irradiations at an angle of 45 degrees.

Equation (5.1) shows a simple model suggesting the linear proportionality of the TEY yield (η_{TEY}) with the product of absorption coefficient ($\mu(E)_\theta$) and photon energy (E). Deriving this simple model, however, is established on several assumptions. One critical assumption to be fulfilled is that the effective photon attenuation length (L_{eff}) must be large enough compared to the escape depth of electrons (L_e) within the energy range of interest. Therefore, the assumed proportionally does not hold in case of strong absorption [112, 121, 126]. L_{eff} is the length that light travels through the sample before it reaches 37% (1/e) of its initial intensity and is defined according to equation (5.2).

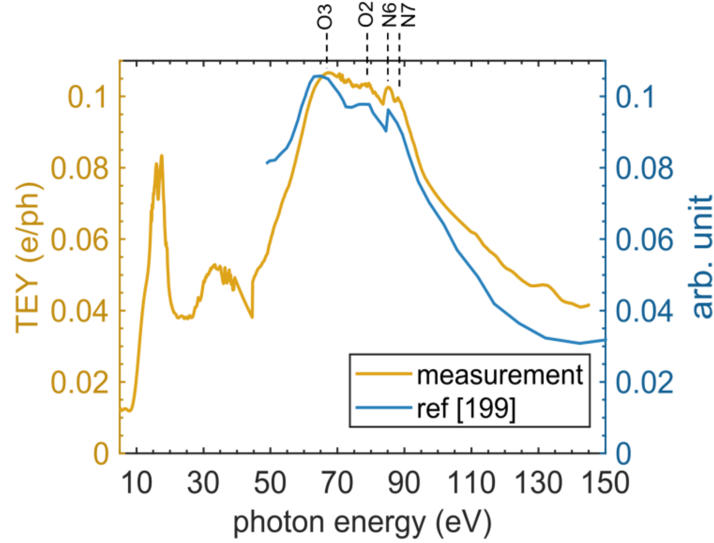

Figure 5.4. Comparison of the measured TEY data with the reported TEY spectra in ref [199]. The TEY values from the reference are scaled to values close to our measured data to make a better comparison between the overall shape of the two plots.

$$\eta_{TEY} \propto [\mu(E)_{\theta} \times E] \quad (5.1)$$

$$L_{eff} = \mu(E)_{\theta}^{-1} = \mu(E)^{-1} \times cos(\theta) \quad (5.2)$$

In equation (5.2), $\mu(E)$ is the absorption factor of the material at energy E, and θ is the angle between the surface normal and the incident beam's direction, which is 45° in our experiment.

Henneken et al. [199] measured the escape depth of electrons (L_e) by recording the secondary electron yield from different gold thicknesses, and they obtained 1.4 nm at 150 eV as the minimum of the escape length. Thomas [208, 209] and Pong et al. [209] also reported a constant escape depth independent of the primary energy for Au, of 3.7 and 4 nm, respectively. Using an average of $L_e = 2$ nm for Au electrons, the product of $L_e L_{eff}^{-1}$ (see equation (5.2)) could reach values above 0.2 (Figure 5.5), too far from satisfying the $L_e L_{eff}^{-1} \ll 1$ condition to consider the possible proportionality in equation (5.1).

In the energy range <50 eV no reference data are available. Possibly, the peak at 15 eV (Figure 5.4) is due to carbon contamination.

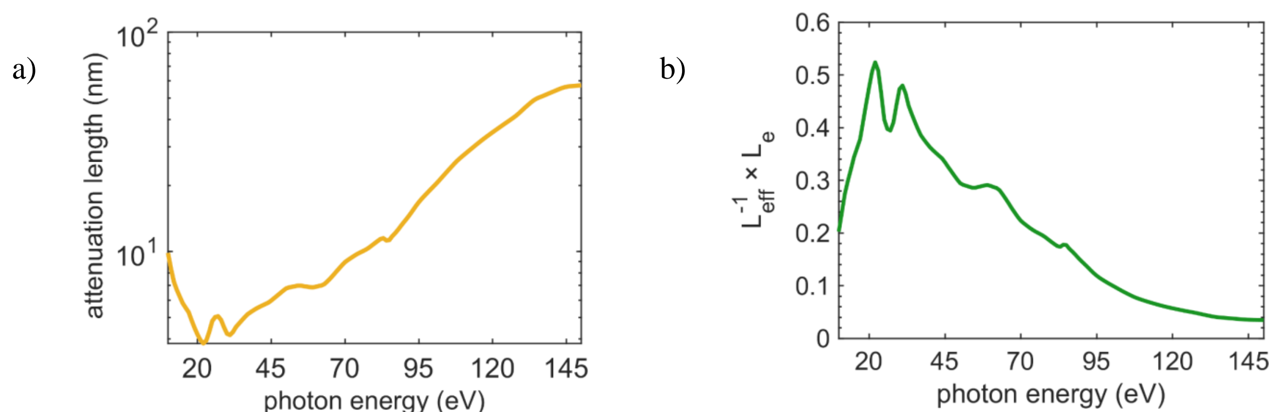

Figure 5.5. a) Photon attenuation length (equation 5.2) for Au in the energy range of 10 – 150 eV at incidence angle of 45°. b) Ratio of escape depth to effective absorption length for Au with L_e = 2 nm.

5.2.3 TEY measurement on tin-oxo cages

Figure 5.6 shows the total electron yield from the tin-oxo cages with three different counterions. The corresponding absorption spectra of these compounds from the CXRO database are compared in Figure 5.7 for 20 nm thick films. The TEY spectra for the three compounds have similar shapes. The ionization for all the three compounds begins at ~8 eV, and the maximum electron yield occurs around 15 eV. The broad feature from 50 to 80 eV and a narrower one around 90 eV was reproducibly observable in all measured TEY spectra.

Although the shapes of all the 3 TEY plots are similar, on average, the spectrum of TinOAc shows the features around 60 and 90 eV more prominently. The broad feature around 60 eV mainly comes from the ionization from the Sn(4d) orbitals, as can be seen from the reported ionization cross-section of different elements in tin cage compounds (Chapter 4, Figure 4.9). However, the detected peak around 90 eV is neither present in the absorption spectra nor in the ionization cross-section values. Since the N6,7 edges of gold are located around 85 – 88 eV, and it has a high contribution of secondary electrons at this energy (Figure 5.6), we performed the TEY measurements once on a thin film of resist spin-coated on gold and once on the resist coated on a silicon substrate. In the absence of gold, we measured similar TEY spectra for the resist, eliminating the possibility of gold contribution to the observed peak around 90 eV (Figure 5.8).

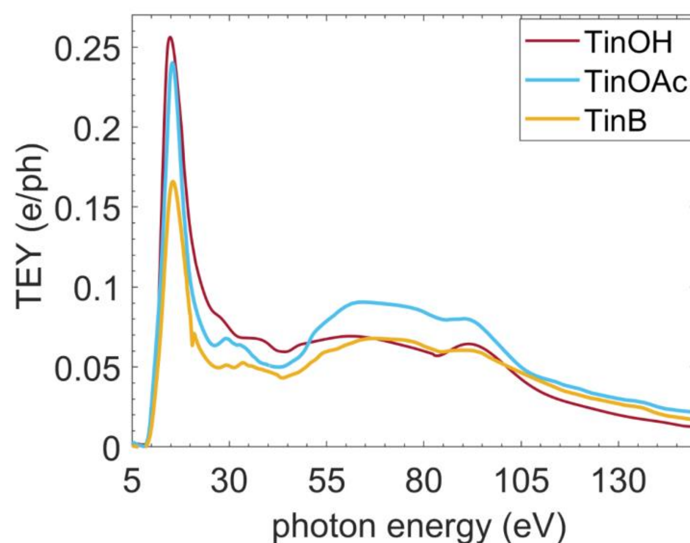

Figure 5.6. TEY measurement results for 3 tin-oxo cages with different counterions.

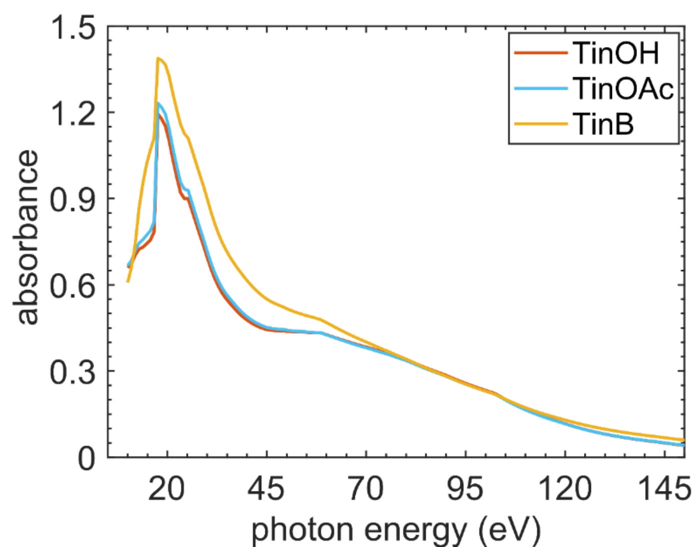

Figure 5.7. Calculated absorption of the tin-oxo cage compounds for a 20 nm thick film from CXRO database.

Comparison of the spectra in Figure 5.8 shows that the spectra measured for TinOAc on Au and on Si substrates, and the spectra with different thicknesses, have very similar shapes. Two different thicknesses of TinOAc films were prepared using concentrations of 20 mg/ml and 10 mg/ml for spin coating of TinOAc on silicon and Au substrates, labeled as Thick and Thin in Figure 5.8, respectively.

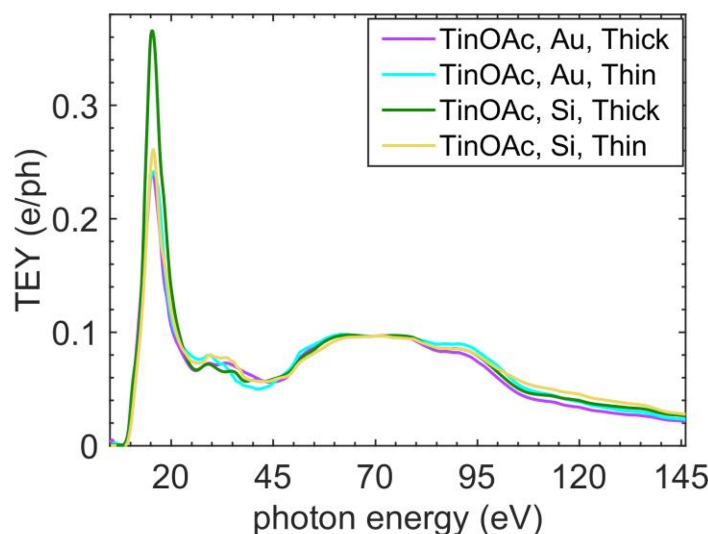

Figure 5.8. The TEY signal measured for TinOAc samples spin coated on silicon and gold substrates. All spectra normalized at 70 eV.

5.2.4 Total electron yield evolution with exposure

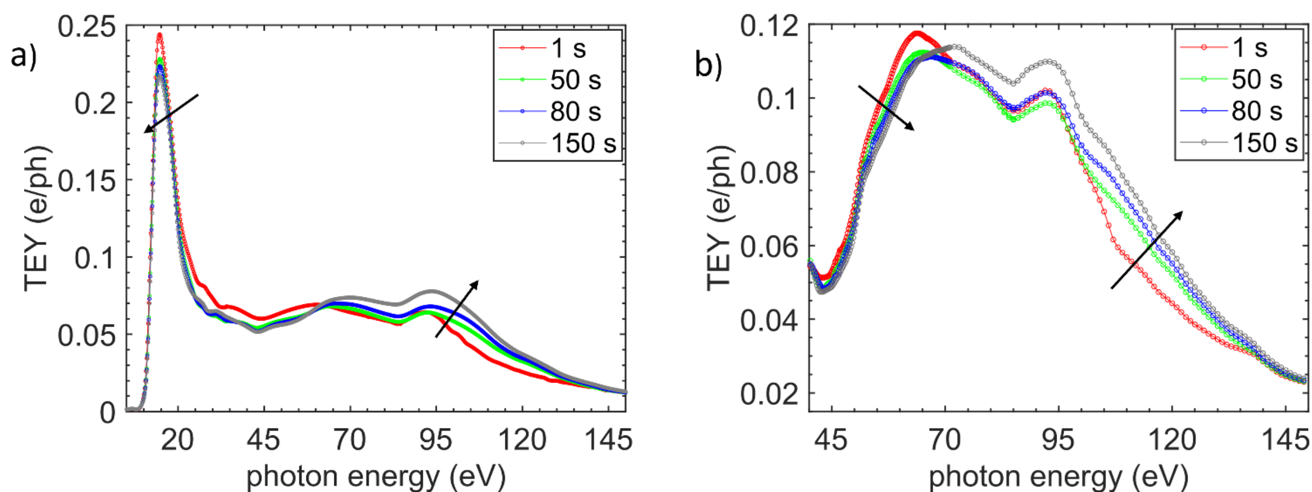

Figure 5.9. Evolution of electron yield with increase of exposure time. a) For TinOH across the energy range of 5-150 eV. b) for TinOAc over the high energy range, 40 – 150 eV.

In section 5.2.3, we presented the TEY data for different tin-oxo cage compounds recorded at the early exposure of the resist, but we know that the resist properties change with exposure time. Therefore, the evolution of the TEY signal was measured with the increase of exposure time. Figure 5.9 shows some of the recorded TEY data for TinOH and TinOAc samples at different exposure times. For TinOAc, the dependency of the TEY signal on exposure dose was only investigated in the range of 40 eV to 150 eV

(Figure 5.9 b). In general, the electron yield decreases with increased exposure time on the lower energy side of the spectrum, but the trend reverses for higher energy incident photons, as indicated by arrows in the graph. Similar trends are also observed in the case of TinB TEY (not shown).

The changes in the TEY signal are plotted in terms of exposure time instead of dose, since, as explained in the experimental section (Chapter 2, section 2.2.4), there is a considerable variation in the incident flux of the synchrotron radiation beam across the energy range used in the measurement (Figure 2.14).

To obtain higher conversion at low photon energies, we followed the change of the TEY signal at a few selected incident energies in which we applied higher doses. The result is presented as a function of exposure dose in Figure 5.10. There is no need to conduct such a separate measurement for incident higher energy photons since high exposure dose values are available in the regular TEY measurements with exposure times up to 120 seconds.

Comparing the TEY trends at different incident energies in Figure 5.10, we can see a drop in the electron yield at the beginning of exposure for doses below 25 mJ cm^{-2} for photon energies < 92 eV. But with the elapse of exposure time, the yield again starts to increase. However, moving to higher energy incident photons, the onset of the yield's growth occurs at earlier exposure doses so that for energies around 90 eV and above, on average, we do not observe the initial drop in the signal.

In general, the TEY depends on the photon absorption within the depth range from which electrons can escape. The chemical conversion mainly consists of the loss of hydrocarbons from the film. This leads to a reduction of the absorption cross section, which is much stronger in the lower energy ranges than at higher energies (Chapter 3 and 4). At the same time, the material becomes denser, which leads to a decrease of the photon penetration depth at higher energies so that relatively more photons are absorbed close to the surface and more primary and secondary electrons can escape. The chemical changes are especially rapid in the early stages of conversion, as shown in Chapters 4 and 6. This could account for the initial decrease of TEY with conversion in the low-energy range. At higher photon energies, the quantum yield of conversion is likely to be higher because more electron-hole pairs are generated per photon. The decrease of the cross section here is small, and the effect of densification leads to an increased absorption coefficient (per unit length), smaller penetration depth, and enhanced TEY. However, the chemical changes are likely to influence the dielectric functions of the material as well and thereby change the electron energy loss function, which influences the secondary electron generation.

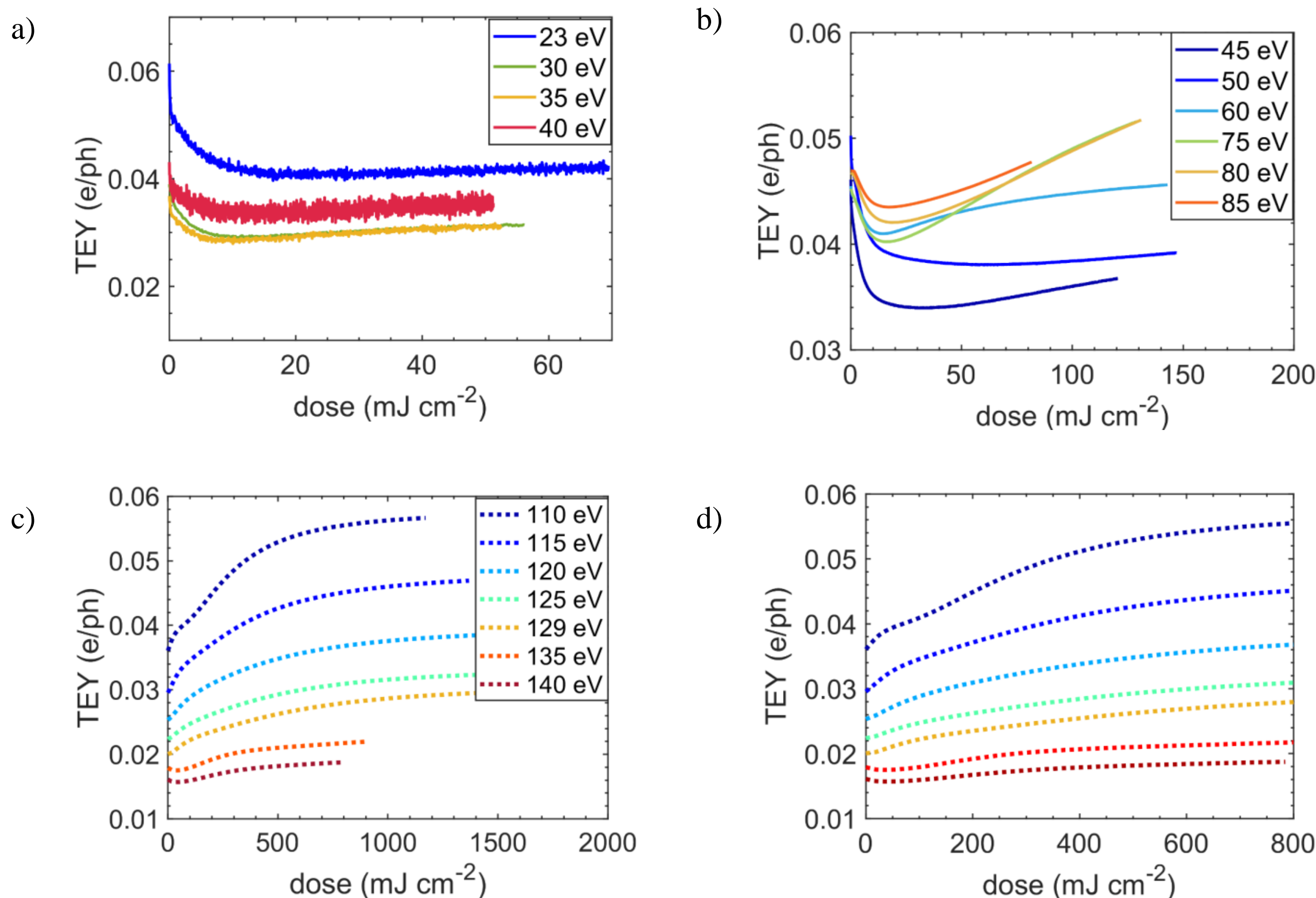

Figure 5.10. TEY signal change as function of exposure dose at few selected incident photon energies. a,b) The results from transient time-resolved TEY measurement on TinOAc. c) The data from a MACRO TEY for incident energies above 115 eV. d) zoom in on the data in (part c) to be able to follow the trend of TEY evolution at low exposure doses where the dose is comparable to the rest of data at lower incident energies.

5.3 X-ray photoelectron spectroscopy of tin-oxo cage

We performed XPS measurement on the tin-oxo cages using the incident photon energies shown in Figure 5.11. The kinetic energy of the emitted electrons was detected over the range from 0 eV up to the applied photon energy over the exposure to the photons. For each incident energy, the detection across the kinetic energy range was done on a single spot so that, in total, eight spots on the sample were consumed to perform this XPS measurement. A bias of 5 eV was applied between the sample and the detector to increase the detection efficiency. Performing an XPS measurement on gold, the work function of the analyzer was determined to be 4.5 eV. Considering these values for bias and work function of the analyzer and using equation (2.11), the BE energy of the electrons was calculated. Therefore, we plotted the count of electrons versus BE in Figure 5.11.

The outcoming electrons form valence or orbitals carry the highest kinetic energy, and they form the peak at the energy around 8.5 eV. The ionization of the tin cage starts at ~ 6.6 eV, as reported in ref [139]. Photons with the energy of 50 eV result in the highest contribution of valence electrons, and this contribution decreases with the increased photon energy.

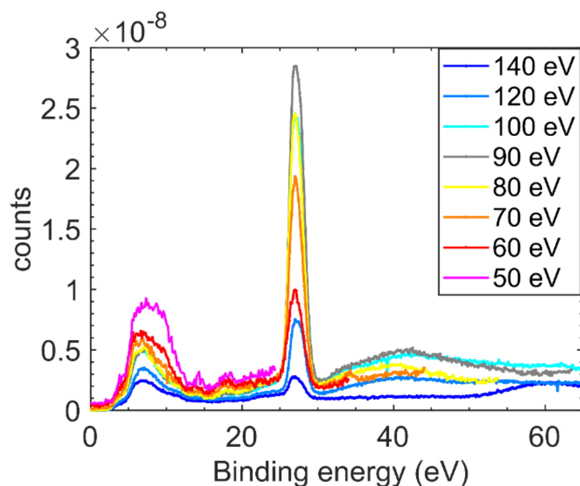

Figure 5.11. XPS measurement result on tin cage at different incident photon energies mentioned in the legend.

The second peaks occur at the binding energy of 28 eV from the Sn(4d) orbitals [139, 148]. More and more electrons from this orbital reach the detector with the increase in photon energy, with the highest count rate detected at an incident photon energy of 90 eV. Calculation of photoionization cross sections, illustrated in Figure 5.15, predict the maximum ionization from Sn(4d) orbitals at incident energies around 60 eV, which does not agree with our observation in Figure 5.11. However, this measurement was done on a photosensitive material whose properties change with exposure. Moreover, the incident flux increases strongly at increasing energies. Therefore, we needed to plan the XPS measurement in such a way as to detect the electrons with minimum possible induced changes in the resist. To achieve this, we applied two modifications to the measurement design. First, we limited the detection range of kinetic energy to that of Sn(4d) orbitals. Secondly, the detection of the kinetic energy was done with steps of 0.15 eV with moving to a fresh spot on the sample for each energy. Hence, in total, more than 500 spots on the sample were used to perform the measurement. The result of this measurement is presented in Figure 5.12.a., in which the intensities are corrected for the different photon fluxes at different energies. We observe the maximum number of electrons from Sn(4d) orbitals at 60 – 65 eV, which then follows a decreasing trend utilizing more energetic photons. Both observations accord with the calculated ionization cross-section for 4d orbitals of tin. However, we should note that for precise data interpretation, we need the transmission

function of the spectrometer, which was not known at the time of this project. The transmission function of most electron spectrometers usually decreases for more energetic electrons so we can expect that the photon energy that gives the highest yield of Sn(4d) electrons will be higher than the 65 eV found here without the correction for the detection efficiency.

To examine the results further, we used the same exposed spots from this measurement and redid the same measurement on these spots. Figure 5.12.b compares the detected electron count for the measurement on the exposed spots (in grey) with the primary one (main measurement) on the fresh sample (colourful plot map). By comparing the results of measurement on the fresh spots versus on the exposed ones, we can observe a noticeable difference between the results of the two measurements, and therefore, a reliable XPS measurement on the resist needs to be accomplished with the least conversion of the material possible.

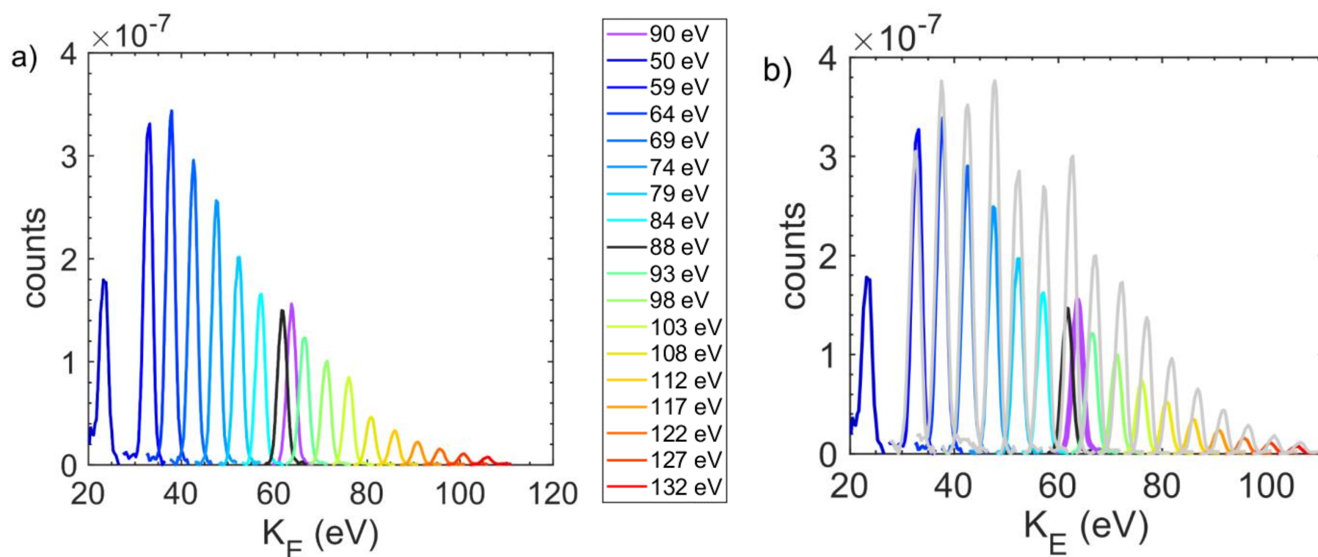

Figure 5.12. Electron emission from the tin 4d orbital of tin cage. a) On the fresh spots as the goal measurement. b) The result of XPS measurement on the exposed spots as the test measurement, shown in gray and compared with the results of measurement on fresh spots, plotted in color.

To obtain further insight into the energy distribution of the electrons detected in the TEY measurement, photoelectron measurements were performed on TinOAc at four selected incident energies (Figure 5.13). The prominent peak at 5.2 eV results from all low energy electrons that could leave the surface after multiple inelastic scatterings inside the material. The data is normalized to 1 and zoomed in the Figure 5.13.b to be able to see the rest of the spectrum at higher kinetic energies.

At a photon energy of 30 eV, only the valence orbitals contribute to the spectrum from the tin cage since the binding energy of 4d orbitals was determined to be at 28 eV. At higher incident energies the Sn(4d) electrons also participate in the total XPS emission. The total number of emitted electrons at each photon energy was calculated by integrating the area under the corresponding spectrum in Figure 5.13. Similarly, the area under the peaks belonging to valence and Sn(4d) were integrated. The ratio of the outcoming electrons from these orbitals to the total detected ones are shown in Figure 5.14 parts a and b, respectively. As we can see, the contribution from these orbitals decreases with increased photon energy and more Sn(4d) electrons contribute to the XPS spectra at the incident energies of 60 and 90 eV. For a quantitative analysis we should also apply a correction for the transmission function of the electron spectrometer, which unfortunately is unknown.

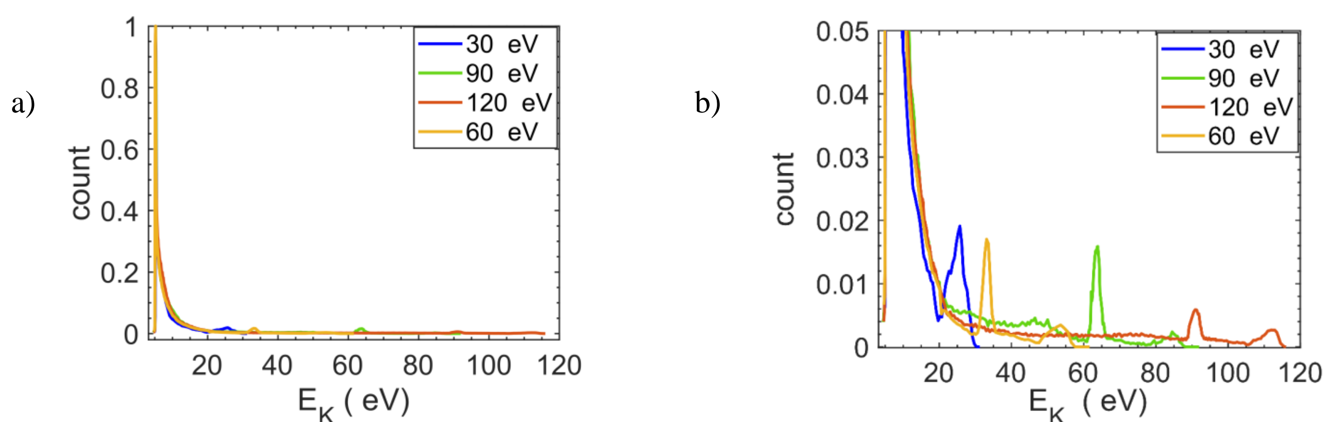

Figure 5.13. a) The result of UPS measurement performed on TinOAc at the given photon energies. b) Zoom in part a.

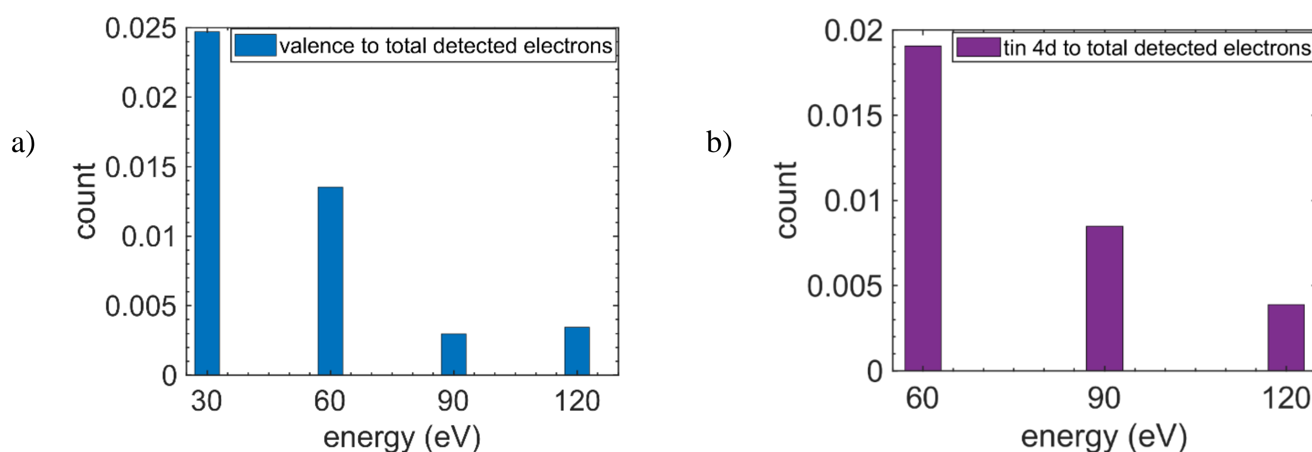

Figure 5.14. Ratio of the valence and Sn(4d) electrons to the total detected ones at each incident photon energy.

5.4 Discussion

The minor feature at 21 eV on the TinB TEY spectra (Figure 5.6) is the N4 edge of the Sn 4d orbital. This peak is predicted precisely at the same energy on the ionization cross-section of the tin cages (Figure 5.15). But it is interesting that this peak was only detectable in the case of TinB and not observable in the TEY spectrum of the other two compounds. This peak is located at 24 eV on the absorption spectra of the resist, 3 eV of blue shift relative to its position (21 eV) on the ionization cross-section spectrum and on the recorded TEY one. This energy difference is the same as the one for the maximum in TEY spectra at ~15 eV relative to the absorption spectrum (~18 eV).

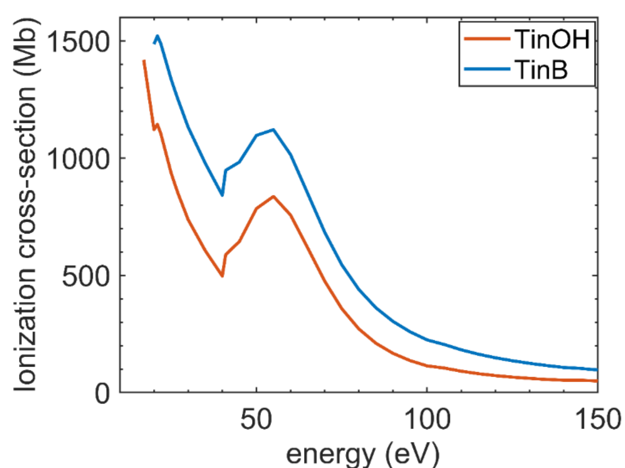

Figure 5.15. Theoretical ionization cross-section of TinB versus TinOH. The ionization cross-section of TinOAc is almost identical to that of TinOH and therefore it is not plotted.

We also observed (Chapter 4, Figure 4.3 and Figure 4.4) the N4 edge of Sn 4d orbital at 24.5 eV on the absorption spectra of TinOH and TinOAc, obtained using the broadband photons from the high harmonic generation in argon as the exposure source. However, this feature became only visible when the contribution of Sn 4d orbitals was elevated at this energy due to the cleavage of carbon-containing groups after some exposure.

The recorded TEY spectra show ~8 eV as the onset for the resist's ionization, as the minimum required energy to eject the first primary photoelectron. This is somewhat higher than the smallest binding energy reported with XPS (5 eV) [139] or estimated from computation (6.6 eV). The binding energy in XPS is, in principle, defined with respect to the Fermi level, which sets the HOMO binding energy as minus half the band gap.

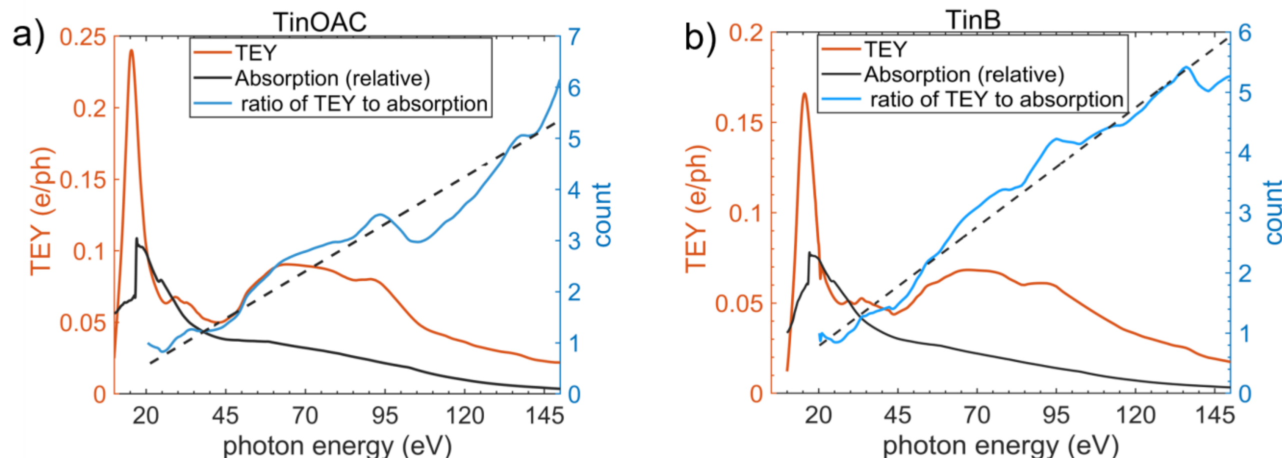

Figure 5.16. TEY (red) and absorption spectra (black) set to a same value at 20 eV, and their ratio (blue) for a) TinOAc, b) TinB. The dashed lines are linear fits to the ratios.

Theoretically, the electron energy loss as a function of electron energy can be calculated without any adjustable parameters if the electron energy loss function (ELF) of the material is known [210]. This then allows to predict the inelastic mean free path and the energy distribution of emitted electrons. Unfortunately, the experimental determination of the ELF of tin-oxo cages was not possible within the scope of the present project. Typically, the ELF of most materials has a broad and strong peak in the energy range of 20 – 30 eV associated with a plasmon state in the material. This gives the most probable amount of energy loss in inelastic scattering. Excitation of the plasmon leads to the formation of a free electron-hole pair, but the kinetic energy of the electron generated will be insufficient to excite another plasmon. Further relaxation can take place by transfer of energy to electronically excited states and vibrations. Thus, we may expect that when an EUV photon generates a valence electron with a kinetic energy of ~85 eV, about three secondary electrons can be emitted. A photoelectron ejected from an Sn 4d orbital at the incident energy of 92 eV, gains a kinetic energy of ~60 eV, and approximately two secondary electrons can be expected to be formed. In addition, Auger relaxation can produce a low-energy electron [211].

Based on this simple consideration, an EUV photon of 92 eV is likely to generate ~4 photoelectrons. The proposed linearity of the TEY with the product of absorption coefficient and photon energy, already mentioned in the introduction of this chapter, is based on the stepwise energy loss due to transfer of energy to the plasmon state. At low photon energies where secondary electron generation is not feasible, the TEY should be expected to follow the shape of the absorption spectrum. To generate a secondary electron that leaves the surface with minimum kinetic energy, the primary photon should have at least twice the energy

of the onset of ionization (~16 eV). In Figure 5.16, we normalized the absorption spectrum of the resist to the TEY at an energy of 20 eV as the point from which the generation of the first secondary electron becomes feasible. The ratio of TEY data to the normalized absorption value is calculated and shown in black in Figure 5.16. As can be seen, with the increase of the energy, the normalized absorption values fall below the TEY spectrum, meaning that the absorption of one single photon at higher energies leads to the generation of more secondary electrons. This comparison also shows that secondary electrons originate mainly from $E_{ph} > 25$ eV. The high peak in the TEY spectrum near 15 eV is from the direct ionization of valence electrons. In the figure, the dashed line shows a linear fit to the secondary electron yield as the function of energy. The slope of the two fits for TinOAc and TinB are ~0.037 and ~0.039, corresponding to 37 and 39 secondary electron per incident keV, assuming that the secondary electron generation yield continues linearly to increase with photon energy, which is usually the case before the SE yield reaches its turning point at very high incident energies. This corresponds to 3.5 – 4 SE at a photon energy of 92 eV.

5.5 Conclusion

We presented the results of photoelectron spectroscopy on tin-oxo cage EUV photoresists by investigating the XPS and TEY spectra in the XUV range in the BEAR beamline synchrotron. For XPS, photons with impinging energies between 50 to 135 eV were used to study the Sn(4d) orbital of the resist specifically. The TEY spectra of the resist were investigated over a broader energy range, 5 to 150 eV. We also traced the changes in the TEY spectrum of the resist with exposure.

The XPS results on Sn(4d) electrons reveal that, in the energy range used in this the study, fewer electrons escape the resist's surface for incident photon energies above 50 eV. The predicted decreasing ionization cross-section of Sn(4d) orbital in this energy region potentially can explain the observed trend. We studied the contribution of the valance and Sn(4d) orbitals to the XPS spectra at the three incident energies of 60, 90 and 120 eV. The result shows more electrons are emitted from the Sn(4d) than valence orbitals at 60 and 90 eV incident energies. We emphasize that the XPS data interpretation lacks the information regarding the spectrometer’s transmission function, which was not available at the time of this project.

Relatively similar TEY spectra were obtained for TinOH, TinOAc and TinB compounds, ignoring the relative detected intensities. An opposite trend was noticed in the electron yield of the resist with

exposure time across the entire recorded TEY spectrum, mainly a decreasing trend for low-energy photons versus a growing one for more energetic photons. This observation was explained by the different photochemical conversion rates of the resist at different energies and with exposure time.

TEY spectra give the ionization onset of 8 eV for the resist. We estimated that approximately 3.5-4 electrons are generated per absorbed EUV photon assuming that the electron yield linearly changes with the absorption coefficient and photon energy in the XUV range. Unfortunately, the data for the ELF of the resist is not currently available. Nevertheless, relying on a value of 20 – 30 eV as the maximum in the ELF for most materials, we obtain a close value of 4 for the emitted secondary electrons per EUV photon.

Chapter 6

Photoconversion of tin-oxo cages at 92 eV

Molecular inorganic tin-based resists are currently in application for printing sub 20 nm features using EUV lithography. An example of this photoresist class is tin-oxo cage with hydroxyl counter ions (TinOH) which can be used as a study model to investigate the complex induced photochemistry at 92 eV radiation.

This chapter presents the results of a study on TinOH using an EUV exposure tool combined with residual gas analysis (RGA) to detect the volatile reaction products, and ellipsometry to analyze the changes in film thickness. The major photoproducts outgassing from the resist were identified as butene, butane and octane by recording their mass spectra during the exposure to the EUV beam, and no tin containing species were observed in the recorded mass spectra. For a few selected masses, the outgassing rate as a function of exposure dose was measured with high time resolution. The results show that the outgassing rates of butene and octane decrease rapidly during the initial stage of conversion, to ~50% of their initial value after a dose of ~25 mJ cm^{-2}.

Furthermore, we obtained a better view of the resist's contrast curve by measuring the resist film's thickness change after exposure and development using ellipsometry. The material is a negative tone resist and at exposure doses >9 mJ cm^{-2}, a measurable layer remains on the substrate after development. The resist reaches its maximum thickness at 45 mJ cm^{-2}. After the full condensation, applying doses higher than 100 mJ cm^{-2} leads to decreasing thickness for both the exposed and developed films with values close to each other.

The thickness decrease upon exposure is related to the chemical conversion, and ~14.5% cleavage is determined as the onset for the complete agglomeration of the resist, corresponding to ~1.7 Sn-C bond cleavage per molecule, with an average quantum yield of ~3 bond dissociations per absorbed photon.

6.1 Introduction

Organotin-based EUV resists are among the most attractive candidates for the EUV lithography nanopatterning technique due to the high absorption of tin at the EUV wavelength of 13.5 nm (92 eV). One promising example of organotin EUV photoresists is the tin-oxo cages with their well-defined structures and relatively easy synthesis procedures [71, 150, 172, 173]. They provide a high absorption cross-section of 11 – 15 μm^{-1} with demonstrated patterning potential at EUV radiation wavelength [64, 72].

Most tin-oxo cages become insoluble upon radiation, acting as negative tone resists [66, 70, 75, 212]. So far, it is assumed that the initially induced cleavage of tin-carbon bonds upon irradiation is the primary trigger of the further subsequent reactions during exposure. The formed tin radicals presumably crosslink with neighboring cages, leading to the material's solubility switch, while the cleaved butyl radicals outgas from the resist [71, 213].

The lowest-energy electronic absorption band of tin-oxo cages occurs in the ultraviolet range, with an onset around 250 nm (4.9 eV), and a maximum at ~220 nm (5.6 eV) [73, 139]. For energies above the onset, the cleavage of tin-carbon bonds is experimentally observed [74, 95]. The reduction of the intensity of the carbon 1s peak in XPS spectra for the exposed resist films was noted and this was attributed to the cleavage of tin-carbon bonds, anticipated based on quantum chemical calculations[73, 148]. However, the solubility switch and the photo-induced chemistry in tin molecular resists need to be understood better to further improve the patterning quality for the EUV lithography application. To achieve that, we have used different approaches [73, 75, 95, 139, 148, 214]. In the present work, we determine the outgassing products from the resist during exposure. Studying these photoproducts and their outgassing rates gives information about reaction pathways and their efficiencies. Moreover, the thickness changes of the tin-oxo cage upon exposure and upon subsequent development are studied using ellipsometry.

In previous works, the photo-fragmentation of tin-oxo cages in the gas phase was studied by mass spectrometry of the ionic fragments formed during the exposure of n-butyl tin-oxo cages in an ion trap to DUV and EUV wavelengths [95, 214]. In the present work, we used the residual gas analysis technique (RGA) to investigate the outgassing products of the thin resist film spin-coated on silicon wafers, which resembles the real conditions in the lithography process inside the EUV scanners. The RGA technique is based on mass spectrometry, in which the outgassing products leaving the resist are detected in the form of ions with different masses after electron impact ionization. The patterns of the fragments observed,

together with the molecular ion peak (M^+) allow to characterize the molecular structures. Because the RGA is calibrated, the measured intensity can be converted to the number of molecules. Certain masses assigned to the four outgassing molecules were selected, and their outgassing rate as a function of time was observed in RGA fast acquisition mode [215], which is then related to the rates of reactions during the exposure.

One concern for EUV lithography is the contamination of vacuum systems and optics inside the EUV scanners through the outgassing of poorly cleanable products. Outgassing metal-containing products are a main source of permanent (non-cleanable) contaminations. In comparison, hydrocarbons can be removed from the optics' surface with methods such as in-situ atomic hydrogen cleaning [216, 217], though their outgassing level must stay below the permitted levels [218-222]. Therefore, the current study additionally addresses this concern.

6.2 Materials and methodologies

6.2.1 Sample preparation

For outgassing measurements, thin films of the TinOH resist on a silicon wafer were used [73, 150]. Si wafers with 4 inch or 8 inch diameters were initially heated up to 150 °C and covered by pure hexamethyldisilazane (HMDS) to form a single silane layer on the wafers followed by spinning them at 4000 rpm to remove the remaining HMDS. The treated wafers were heated again at 150 °C for 1 minute.

A 10 mg/ml solution of TinOH was prepared in toluene and filtered using a 0.2 μm pore size syringe filter. For outgassing measurements, fresh solutions of TinOH were spin-coated at 2500 rpm for 30 seconds on top of the HMDS layer and then they were baked at 90 °C for 1 minute. The exposed wafers were developed using a mixture of isopropanol: water (2:1) for 35 seconds and then rinsed in pure water and dried under a flow of nitrogen.

6.2.2 RGA measurements: methodology and instrumentation

Outgassing experiments were performed using a tool located in IMEC (Leuven, Belgium). Figure 6.1 shows a schematic of the used instrumentation [215, 219, 222, 223]. The tool includes a (Hamamatsu) Energetiq EQ-10 Z-pinch xenon plasma source for EUV exposure. The generated EUV radiation from the source is filtered by a Zr spectral purity filter (SPF) and reflected by a multilayer (ML) mirror and grazing

incidence mirrors towards the wafer to expose the samples at 92 eV (13.5 nm wavelength). The tool is equipped with a Residual Gas analyzer (RGA) consisting of a Pfeiffer QMG422 mass spectrometer which can measure over an atomic mass unit (amu) range of 1 to 512 amu.

The beam diameter on the wafer is approximately 5 mm, and an irradiance of 3 mW cm^{-2} was used to expose the wafers. The thickness of the films on the wafers was measured using an ellipsometer (KLA-Tencor ASET F5x) in Imec, and a Cauchy model was used to fit the ellipsometry data of the resist on a silicon wafer.

In this chapter, we describe three types of measurements on the TinOH resist films on silicon wafers:

(1) We utilized the RGA to identify the outgassing molecular masses from the resist during exposure by recording the mass spectra of the resist's outgassing species (6.2.2.1).
(2) The outgassing rate of particular masses over exposure time was monitored using the RGA fast acquisition scan mode (6.2.2.2).
(3) We exposed the sample using the EUV source to different exposure doses, and the corresponding thickness change at the applied doses was measured before and after development to obtain the contrast curve of the resist (6.2.2.3).

6.2.2.1 Mass spectrometry of tin-oxo cage outgassing fragments: methodology

For this measurement, a thin layer of TinOH photoresist with a thickness of approximately 11 nm was coated on a 4-inch Si wafer. The wafer was inserted into the RGA tool on an x-y stage. The RGA tool operates in a vacuum environment, but gas molecules always penetrate the chambers. Therefore, a mass spectrum was recorded from the gas molecules present inside the tool as the background before starting the exposure, shown in Figure 6.2, section 6.3.

Afterwards, the wafer was exposed to the 92 eV beam, with the beam continuously scanning the sample's surface at a fixed scanning speed of 0.5 mm s^{-1}. The outgassing data was collected in eleven subsequent exposure cycles. Each exposure cycle lasted ~135 s, while one second of exposure equals 3 mJ cm^{-2} dose of EUV photons. The reason is that the RGA tool takes ~135 seconds to record masses from 1 to 300 amu, therefore, the outgassing rate of ions can be measured over 135 seconds with the sample being exposed up to 30 mJ cm^{-2}. During each exposure period, a mass spectrum was recorded from the outgassing resist species within the range of 1 to 300 amu.

6.2.2.2 Fast acquisition RGA measurement: methodology

After determining the outgassing species through the mass spectrometry measurement described in section 6.2.2.1, we selected a few outgassing masses, each representative of an outgassing molecular material from the resist. Then we run the RGA tool in the fast acquisition mode with a temporal resolution of ~ 0.65 s. This mode enables us to follow the outgassing rate of those selected masses over exposure time which is connected to the rate of the photoinitiated reactions at EUV radiation.

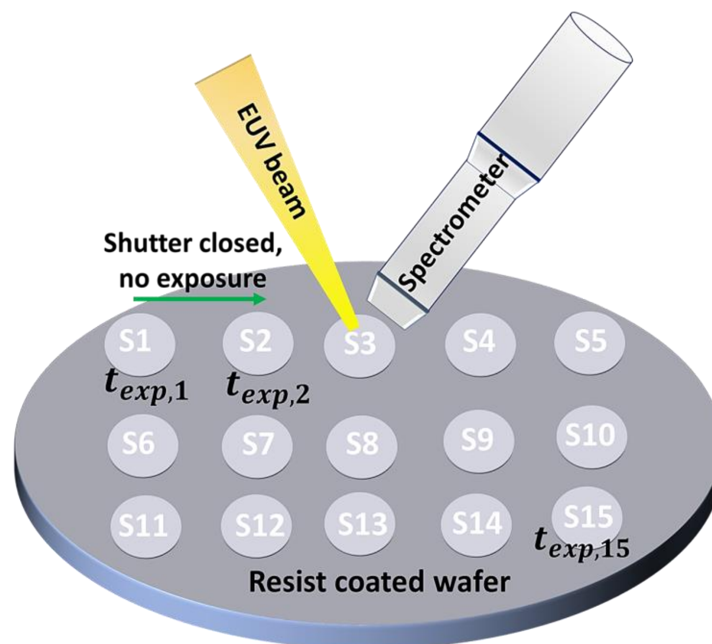

Figure 6.1. Schematic representation of the fast acquisition RGA measurement. 15 spots on the wafer, symbolically shown by letter S, were exposed to 92 eV beam. The exposure time of $t_{exp,i}$ (or the exposure dose) increases from the first spot to the last one. During the movement (shown by the green arrow) between the two adjacent spots, the exposure is interrupted by closing the shutter in front of the beam while recording the outgassing species is continued.

We selected masses at 56, 84, 44, and 2, indicative of butene, octane, carbon dioxide, and hydrogen, respectively, to perform the time resolved RGA measurement. The reason for choosing hydrogen and carbon dioxide was to ensure that they outgas from the resist since they were also present in the background spectrum. Supposing these two products outgas from the resist upon exposure, we expect their number of molecular ions reaching the detector to change with exposure time. Probing the outgassing rate of more masses is possible at the expense of time resolution. Since we were interested in observing the rise of outgassing products as the exposure starts and monitoring the photoinitiated reactions at the beginning of exposure, we limited the measurement to the above-four mentioned species.

A TinOH film of approximately 24 nm, coated on an 8-inch wafer, was used for time-resolved RGA measurements. Fifteen different spots on the wafer were exposed to EUV photons to different dose values by increasing the exposure time from one spot to the next. For more clarity, the measurement procedure is schematically represented in Figure 6.1 with the shortest duration of exposure time, $t_{exp,1} = 0.0213$ minutes on the spot 1 (shown by S_1 in the figure), to the maximum exposure of $t_{exp,15} = 30$ minutes on the 15th spot (S_{15}). We stopped the exposure during the movement between the two consecutive spots by closing a shutter in front of the source beam while we kept recording the outgassing molecules for some additional time corresponding to the scanning speed of the tool during the movement to the next spot. The reason is that although we stop the exposure, the reactions and outgassing process can persist for a while. The movement time between the two consecutive spots is equal to 2 minutes of additional integration time.

The background mass spectrum was recorded on each spot before launching the exposure. For each spot, we recorded the number of outgassing ions as the function of exposure time using the same temporal resolution.

6.2.2.3 Film thickness evolution as a function of exposure dose

To determine how the thickness of the resist film changes with exposure dose, 16 different spots were exposed to different dose values on a tin-cage coated 8-inch Si wafer. The thickness change at each of these spots was measured using ellipsometry before and after exposure. The determined initial film's thickness (before exposure) at these 16 spots was, on average, 23.3 nm with the refractive index of 1.61 at 633 nm from the ellipsometry measurement. Then the thin film was developed, and the corresponding induced thickness change was measured after development at the same spots and using the same Cauchy ellipsometry model.

6.2.2.4 Outgassing measurements: Data processing

In an RGA measurement, outgassing fragmented ions are detected in units of partial pressure (mbar), but they can be converted to molecules cm^{-2} s^{-1} using equation (6.1) [224, 225]:

$$R_i = S_{eff} \frac{(P_{res} - P_{bg})}{k_B T A} \tag{6.1}$$

Where R_i is the outgassing rate for a certain mass in molecules cm^{-2} s^{-1}, S_{eff} is the pumping speed and k_B is Boltzmann constant. T is the temperature (290 K). P_{res} and P_{bg} are the partial pressures measured for

resist and background, respectively, and A represents the area exposed to EUV photons (0.2 cm^2). The pumping speed for this system has been determined experimentally and calibrated to be 258 L s^{-1}.

The data from outgassing measurements will be presented in molecules cm^{-2} s^{-1} throughout this chapter. We used the NIST Mass Spectrometry library [226] as the reference to identify the outgassing molecular ions in the recorded mass spectrum and estimate each outgassing mass's contribution to the recorded mass spectrum.

6.3 Results

6.3.1 Mass spectrometry of the tin-oxo cage outgassing products

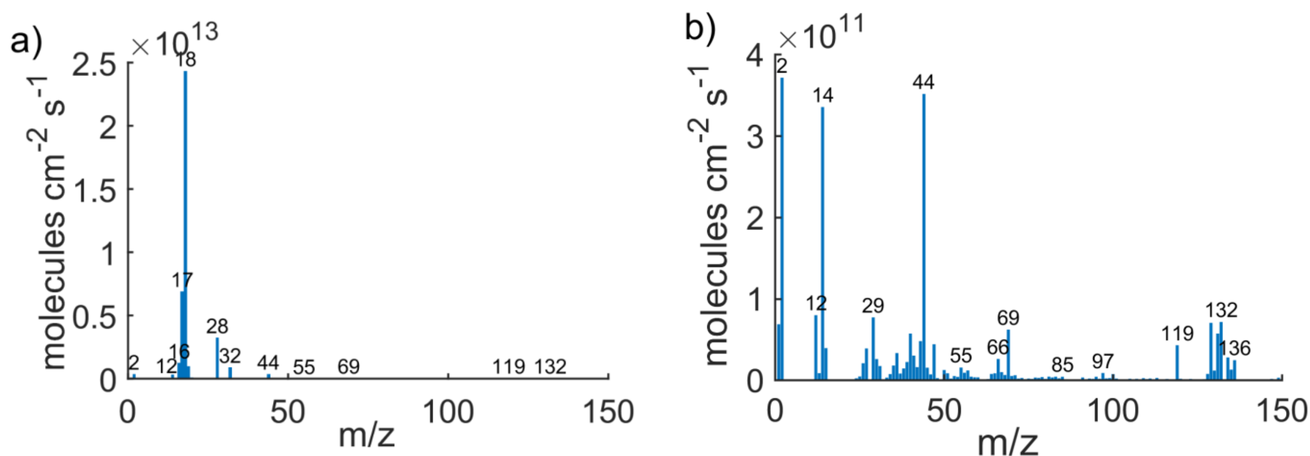

Figure 6.2. Background spectrum in RGA tool measured before exposing the sample. a) Background spectrum dominated by water (m/z 16-19) and air molecules (m/z 28 and 32); b) Remaining background after removing the peaks from water, nitrogen, and oxygen.

Figure 6.2 shows the recorded background spectrum from the gas molecules present inside the tool before the start of the exposure. As can be seen, there is a relatively high background from water molecules (m/z 16 to 19), hindering the detection of any possible outgassing ions from the resist in this range. The second highest peaks in the background belong to the penetrating air into the system with nitrogen and oxygen peaks at m/z 28 and 32, respectively. To be able to illustrate the contribution of other masses to the background spectrum which are much smaller than those of water and air, the peaks corresponding to water and air were removed from the background, simply by setting their values equal to zero, and the remaining spectrum is represented in Figure 6.2.b. In this figure, for instance, peaks from xenon gas (m/z

64 – 68 and 128 – 132) used in the EUV source, carbon dioxide (m/z 12 and 44), hydrogen (m/z 1 and 2) could be observed in the background as well.

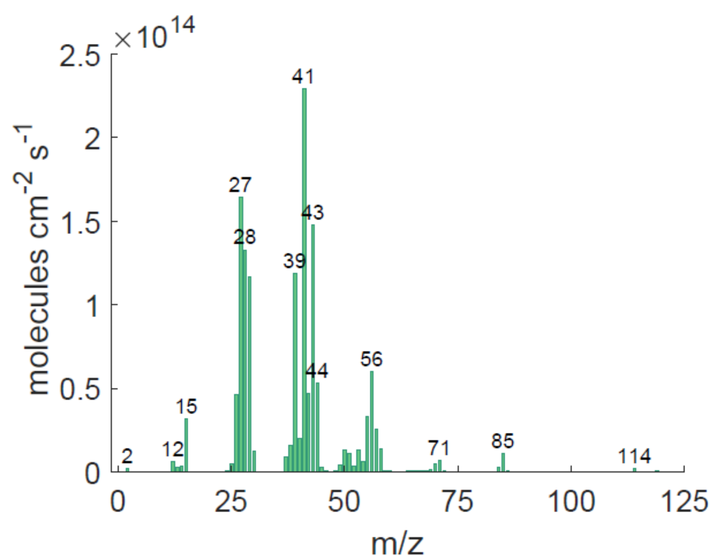

Figure 6.3. RGA data averaged over the 11 recorded mass spectra for different periods of exposure and after background subtraction.

Table 6.1. List of the main outgassing products from tin-oxo cage. In the second column of the table, some of the masses assigned to the outgassing molecules are given using the NIST database [226].

Outgassing molecule	characteristic peaks
Octane	69 – 72, 83 – 85, 86, 114 (M^+)
Butene	39, 41, 56 (M^+)
Butane	43, 58 (M^+)
Carbon dioxide	12, 44
Hydrogen	1, 2

All outgassing spectra recorded by the RGA tool for 11 exposure cycles are averaged together and the result is shown in Figure 6.3 after background subtraction. The measured spectrum is plotted just up to 125 amu since no ions from the resist could be seen above this mass. Comparing the obtained mass spectrum in Figure 6.3 and the NIST library (Figure 6.4), we could identify 1-butene, n-butane, n-octane, carbon dioxide, and hydrogen as the main outgassing products during the exposure with the corresponding characteristic masses as shown in Table 6.1.

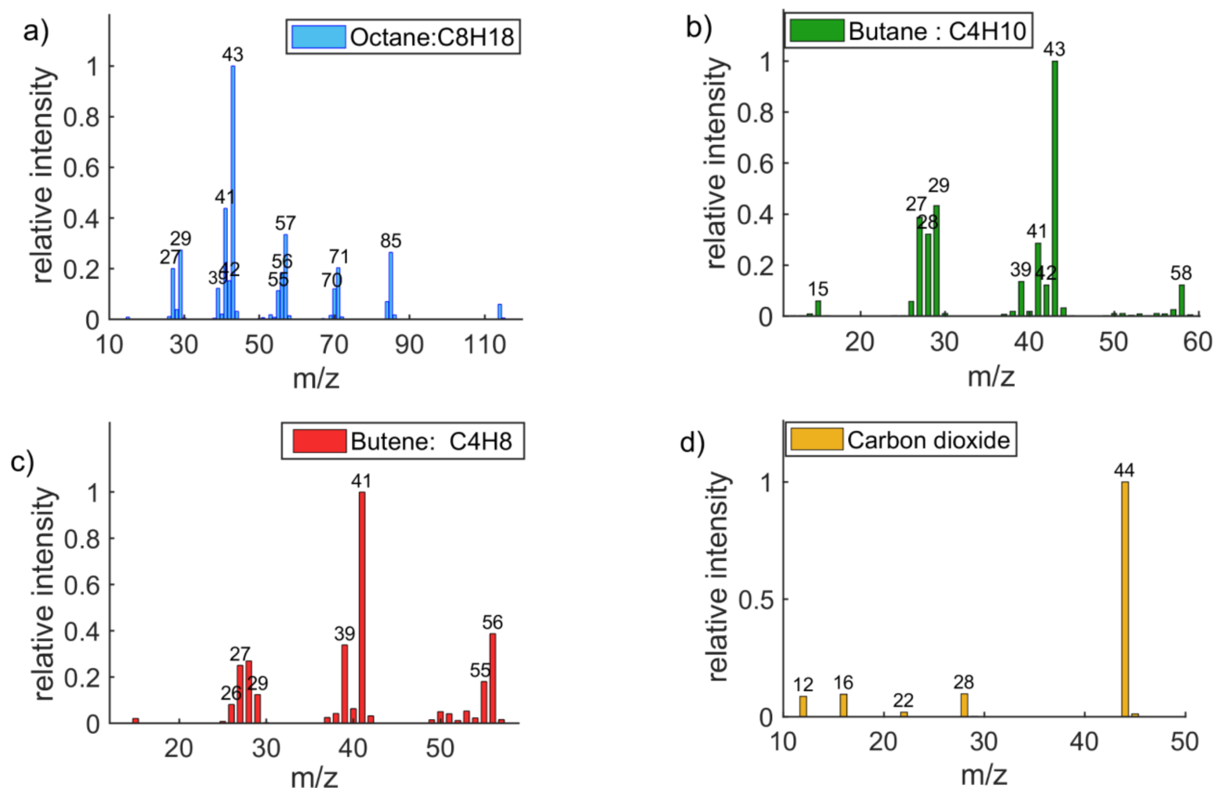

Figure 6.4. The mass spectra (electron impact ionization) of the main four detected outgassing hydrocarbon groups from the NIST database [226].

All outgassing spectra recorded individually per exposure period were summed over the detected ion intensity, and the result is plotted in Figure 6.5 in black, showing the outgassing rate of the material measured during each exposure period. Red, green, blue, and yellow curves show the calculated contributions from the outgassing butene, butane, octane, and carbon dioxide to the total value, respectively. The grey curve is the sum of the contributions from the four outgassing species showing that more than 70 percent of the outgassing material comes from the four mentioned molecules. To calculate the contribution of one outgassing species, for instance, octane, to the total measured values, one of its outstanding peaks which has the least possibility of overlap with the other outgassing species (m/z 114) is selected. The ratio between the measured value at m/z 114 and the corresponding one from NIST is calculated. This ratio is then multiplied by the whole octane mass spectrum from NIST, and it is considered as the contribution of octane (blue curve) to the total measured one (the black plot). After subtracting the octane spectrum from the total measured one, the same calculation was followed for the outstanding peaks at 58, 56, and 44 to estimate the contributions from butane, butene, and carbon dioxide, respectively. The remaining outgassing masses after subtraction of the four given contributions are plotted in Figure 6.6.

They, in total, contribute to around 71% to the total recorded RGA data (black curve in Figure 6.5). Of the detected carbon containing products, butene accounts for 30 ± 1 %, butane 26 ± 1 % and octane 11 ± 2 %. The CO_2 contribution is minimal with only accounting for 4.5 ± 0.58 % percent to the total detected masses. The given error bar points to the observed variations for the 11 recorded spectra.

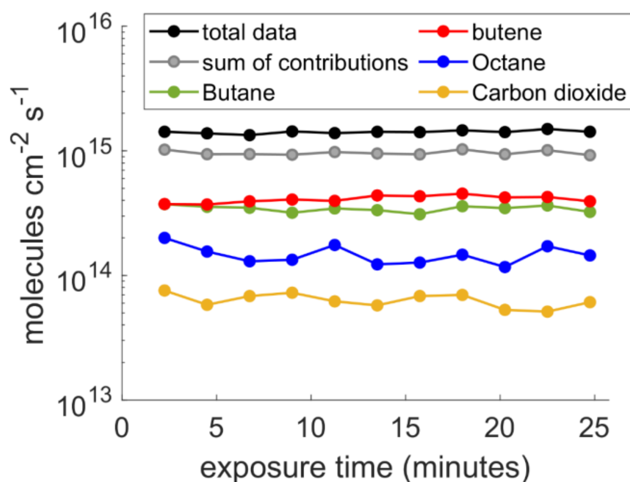

Figure 6.5. Calculated contributions from the main outgassing species to the total outgassing rate measured in each exposure period. The circles show the real data from the measurement. The outgassing rate was measured in 11 subsequent cycles with the sample being exposed to 30 mJ cm^{-2}.

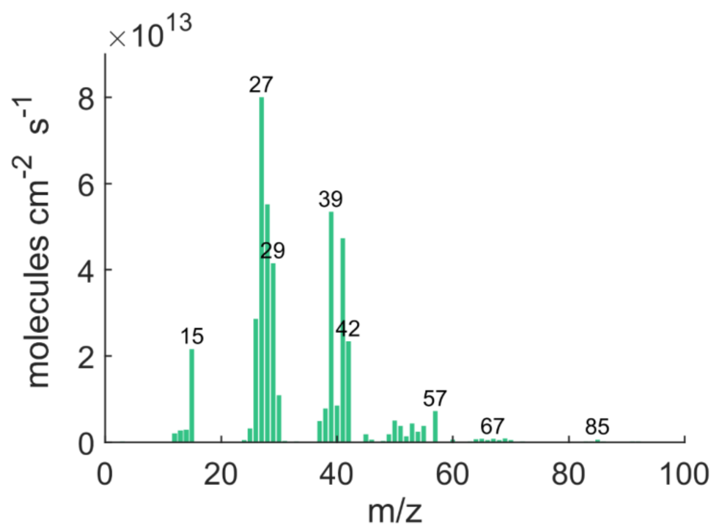

Figure 6.6. Remaining outgassing masses after subtracting the contributions of butene, butane, octane, and carbon dioxide from the spectrum in Figure 6.3.

6.3.2 Fast acquisition RGA of selected outgassing materials

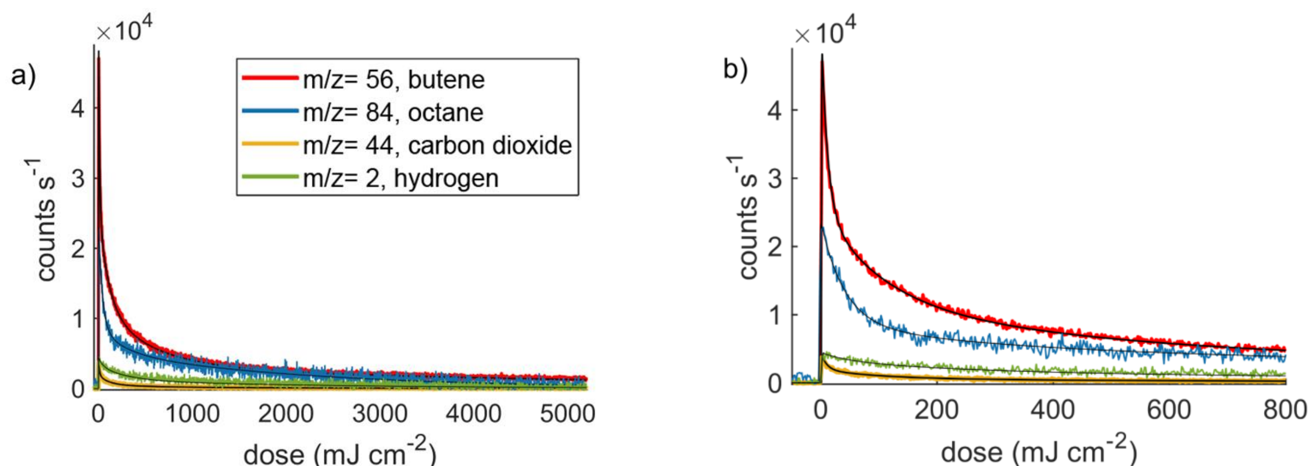

Figure 6.7. a) Measured counts per second (as detected) for the four selected outgassing masses at different exposure doses. b) zoom in the figure for the first 800 mJ cm^{-2}. The fit to the measured data is plotted in black.

The methodology of fast acquisition RGA was described in section 6.2.2.2. Amongst the recorded data for the 15 different exposure times, we only show the outgassing rate for the longest exposure time here. This corresponds to the 15th spot in Figure 6.1. We noticed that the results from the 15 spots perfectly agree with each other over the commonly measured time. The figure is zoomed-in in part b to see the rate of initially photon driven reactions at low exposure doses. The number of detected fragmented ions for the four selected masses are plotted over the acquisition time of $\Delta t_{15} = 32$ min with $t_{exp,15} = 30$ min or equivalently exposure dose up to 5400 mJ cm^{-2}. The measured curves do not show a simple exponential decay, but they can be modeled (shown in black color) with the convolution of a gaussian function and the sum of four decaying exponentials. For each plot in the figure, the background is subtracted. The ratio of the maximum detected count to the background is more than 95 and 61 for m/z = 56 and m/z = 84, while these ratios are only 2.1 and 1.5 for m/z = 44 and m/z = 2, respectively.

As we see, the four outgassing species peak at the beginning of the exposure, followed by a rapid decrease in the rate of reactions in the first 25 mJ cm^{-2}. The decaying trend in the outgassing rate of the hydrogen and carbon dioxide as the other two outgassing species suggests that they are possibly formed as the result of the resist's exposure, and they are not from the background. The outgassing rate in Figure 6.7 was integrated for the first 10 seconds (30 mJ cm^{-2}), which was then converted to the molecules cm^{-2} s^{-1} using the information in Figure 6.5 in which the sample has been exposed to the same dose.

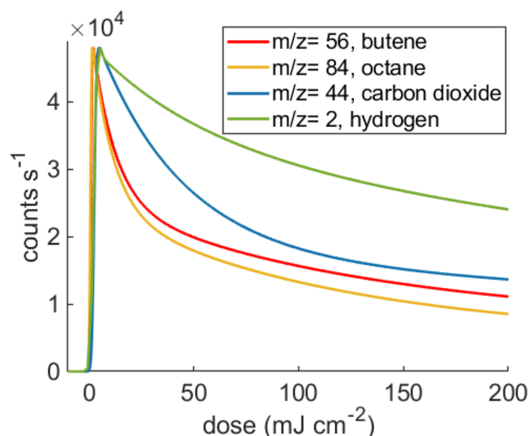

Figure 6.8. Comparison of the time profiles in Figure 6.7, normalized to the max of m/z = 56 (plotted for low doses).

In Figure 6.8, the measured ionic masses are normalized to the maximum count for m/z = 56 to compare their relative decaying rates. The outgassing rates of m/z = 56 and m/z = 84 change with dose in a very similar way. The counts decrease by 50 % at ~20.6 mJ cm^{-2} and 24.7 mJ cm^{-2} for m/z = 84 and m/z = 56. But, as can be seen in this figure, carbon dioxide and hydrogen show different dynamics and a slower decay than the hydrocarbons.

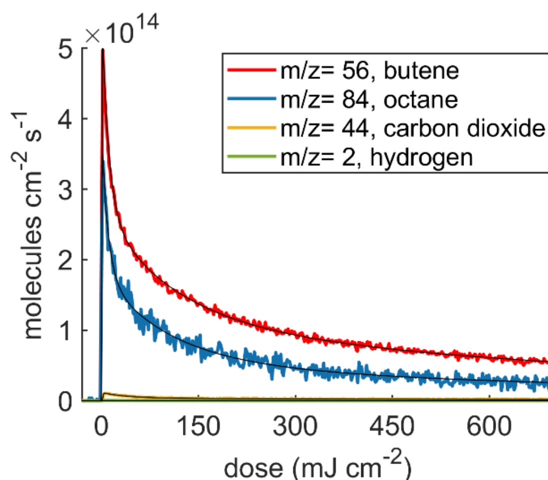

Figure 6.9. a) The decaying outgassing rate of the 4 selected masses after converting the counts in Figure 6.7 to molecules cm^{-2}, shown for the initial 700 mJ cm^{-2} exposure. The outgassing of hydrogen is negligible, as can also be seen from the intensity of m/z = 2 in Figure 6.3.

While in general, the ratio between the formation of butene to hydrogen and carbon dioxide reduces during the exposure, the outgassing of butene to octane undergoes a decaying growth with exposure. For example, the ratio for butene to hydrogen at the start of exposure is 12.5 which then decreases to almost

half of its initial value, while the initial fast growth of butene to octane slows down by the end of exposure to 800 mJ cm^{-2}, from 11 to 18.5 (Figure 6.10).

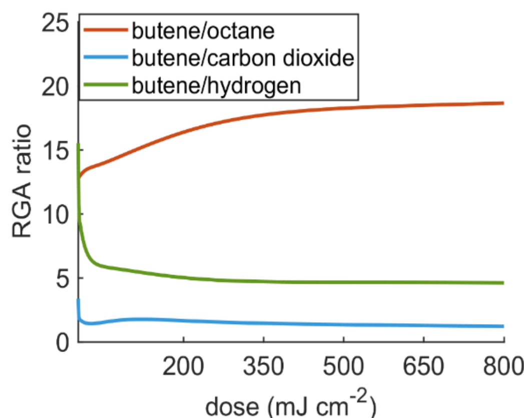

Figure 6.10. Ratio of the outgassing rate of butene to that of the other 3 measured species in Figure 6.7.

6.3.3 Film thickness evolution as a function of exposure dose

The resist thickness after exposure and development relative to the initial thickness as a function of exposure dose is known as a contrast curve in the lithography community [227]. The contrast curve indicates the resist's sensitivity, defined as the exposure dose per unit of area required for pattern formation, which impacts the lithography machine's throughput. In a contrast curve, the onset of the solubility switch is commonly called dose to gel in the case of negative tone resist. The contrast for a negative tone resist indicates how fast the transition to a fully insoluble resist occurs. To determine how the thickness or density of tin cage film changes with exposure dose and to obtain the contrast curve of the resist upon EUV beam irradiation, 16 different spots on a tin cage coated wafer were exposed to different dose values increasing from 0.1 to 5400 mJ cm^{-2}. The initial thickness of the film at each spot measured by means of ellipsometry before exposure is shown in Figure 6.11.a in green. The corresponding thickness values, measured at the same positions on the wafer but after exposure, are plotted in blue. The red plot shows the thickness of the same spots measured after the development of the exposed resist. To better visualize the exposure-induced changes (reduction) in the resist's thickness, the obtained thickness values after exposure and development are subtracted from the initial values and plotted in Figure 6.11.b. These thickness values are estimated by fitting a Cauchy model to the wavelength dependent refractive indices measured by ellipsometry. The difference between the refractive index of the exposed and developed areas with the fresh ones is shown in Figure 6.12.

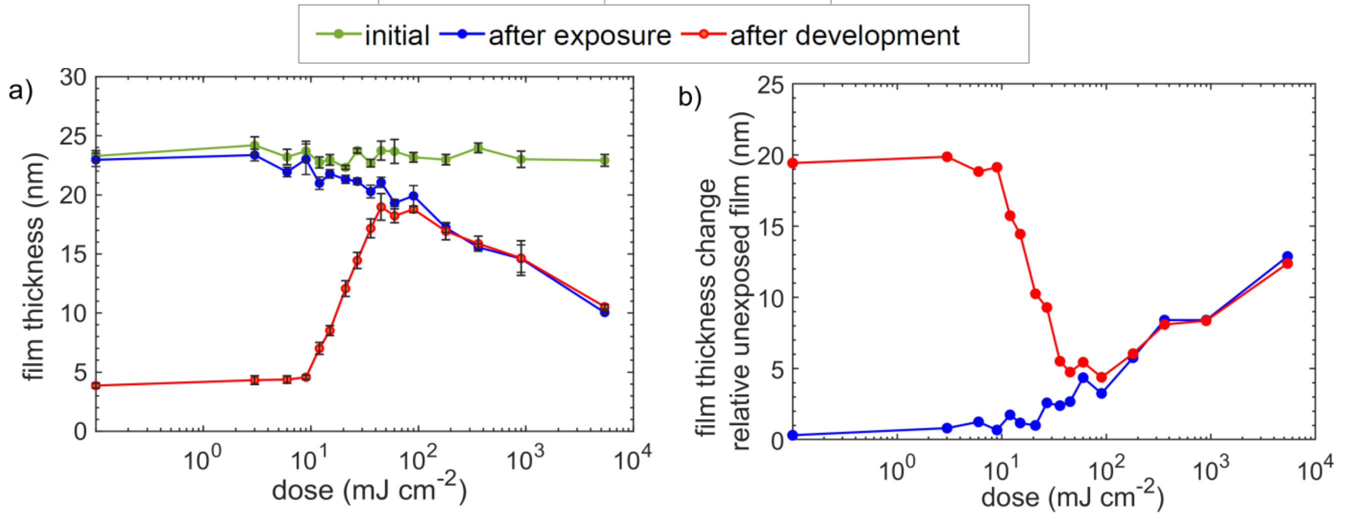

Figure 6.11. a) Thickness of tin cage resist film measured at 16 different positions with different exposure doses, before exposing the wafer, after exposure to EUV beam, and after development. b) Thickness difference relative to unexposed film; blue: exposed only; red: exposed and developed.

As can be seen in Figure 6.11, the film thickness shrinkage is triggered at the beginning of exposure, and it decreases smoothly by 8.5 nm when the exposure dose reaches almost 360 mJ cm^{-2}. In comparison, only a 4.5 nm further reduction in the thickness of resist was observed with extra exposure of the resist to the highest incident dose value (5400 mJ cm^{-2}). After development, the spots exposed to doses below 9 mJ cm^{-2} were washed away from the surface, corresponding to the behavior of negative tone resists as previously observed for tin-oxo cages. The retention of insoluble material starts at 9 mJ cm^{-2} and the resist becomes fully insoluble at doses >45 mJ cm^{-2}, which leads to a contrast of $\gamma \approx 1.44$ according to the definition in equation 6.2:

$$\gamma = \left[\log_{10}\left(\frac{D_{100}}{D_{10}}\right)\right]^{-1} \tag{6.2}$$

D_{100} and D_{10} are the minimum dose for full condensation and the dose to gel value, respectively. The development occurs at the rate of ~ 21 nm per decadic logarithm of incident dose, obtained from a linear fit to the resist transition region in red plot in Figure 6.11.

We should note that we did not bake the samples after exposure. The obtained sensitivity and contrast of the resist from Figure 6.11 are close to the values reported in the study by Haitjema et al. [70]. They obtained the onset of gelation at ~10 mJ cm^{-2} with a maximum film thickness at ~50 mJ cm^{-2} for TinOH and TinOAc films with an initial thickness of 40 nm. However, the same study showed that applying a post exposure bake can improve the sensitivity and the contrast of the resist by 2 and 4 times, respectively.

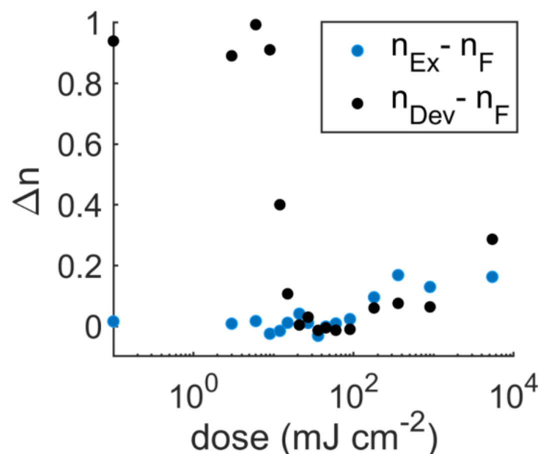

Figure 6.12. The difference between the refractive indices measured on the same spots for the fresh film (n_F) with the measured refractive indices after the exposure (n_{Ex}) and development (n_{Dev}).

A development time of 35 seconds was used. From Figure 6.11, it appears that the unexposed resist could not be completely removed, in contrast with earlier observations [70]. The reason for this discrepancy becomes clear when we look at the relative difference (Δn) between the fresh film's refractive indices (n_F) and those measured on the same spots after exposure (n_{Ex}) and development (n_{Dev}), as presented in Figure 6.12. The ellipsometry was performed over a broad wavelength range from 300 to 750 nm, and the refractive indices are reported at 633 nm. The fitting model for reporting the thicknesses in Figure 6.11 simply considers a resist layer on top of an infinite silicon layer. Therefore, the large Δn values for black color (n_{Dev} - n_F) for doses between zero to 9 mJ cm^{-2} can be attributed to the presence of HMDS and SiO_2; the resist has actually been washed away, and the apparent 4 nm initial thickness for the developed film can be safely ignored.

At higher doses (>100 mJ cm^{-2}), the blue and red curves in Figure 6.11 overlap, showing almost the same thickness values before and after development. The gradual densification due to further (slower) outgassing of hydrocarbons leads to a gradual increase in the refractive index upon prolonged exposure. Even at high doses, however, the refractive index does not get close to that of pure tin oxides because a substantial fraction of the hydrocarbon material is retained in the film.

6.4 Discussion

According to the RGA spectrum in Figure 6.3, we do not see any peak that could be assigned to tin-containing outgassing materials. Only side chains, alkyl groups, are photo-dissociated from the tin-cage core upon exposure. This observation is in agreement with the proposed condensation reaction by Cardineau [71] as the basis of the solubility switch in tin-oxo cage photoresists.

The observation of only organic carbon-containing products in the outgassing also aligns with previous studies in ref. [74, 95], in which the homolytic Sn-C dissociation was shown as the initial photon-driven reaction for the subsequent bridging between different cationic tin-oxo clusters. In these studies, the mass spectrum from the photo-fragmented products of the gas phase tin-oxo cage dication was measured during exposure to DUV radiation (4 – 14 eV). The detected masses were representative of the tin cage dication with the loss of one or more butyl side chains (up to 6 butyl loss at 13.5 eV), with the cleavage of butyls starting at 5 eV. The obtained results in this work also complement the XPS studies in ref. [73, 148] which indicated the Sn-C dissociation by observing a reduction in the ratio of the C(1s) peak to the Sn(3d) peaks for the exposed resist.

The proposed cross-linking mechanism and possible reaction pathways that could lead to the formation of the measured outgassing molecules are depicted in Figure 6.13.

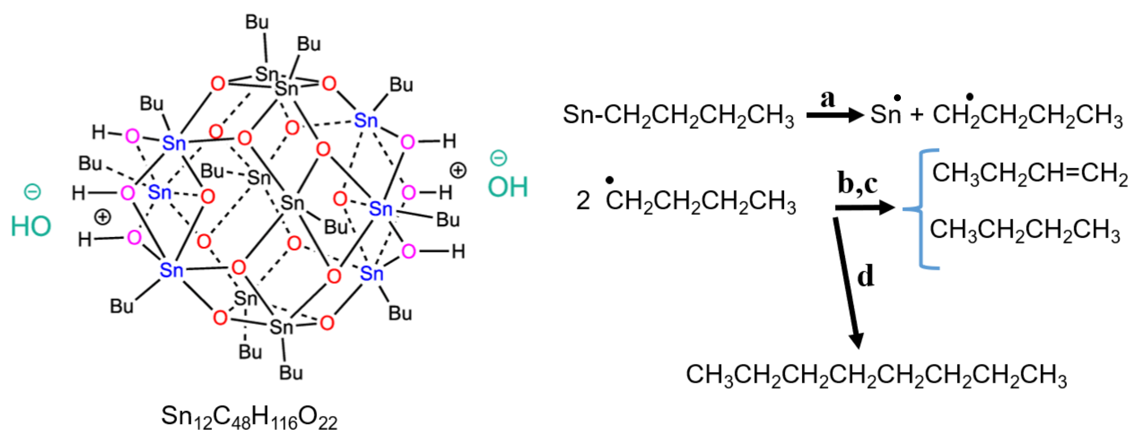

Figure 6.13. Possible mechanisms for the formation of the hydrocarbon outgassing molecules from tin-oxo cage photoresist upon exposure. a) tin carbon bond cleavage. Formation of b, c) Butene and butane (disproportionation), d): Octane (coupling between two butyl radicals).

Both mass spectrometry and RGA fast acquisition measurements revealed butene, butane as the main contributors to the resist's outgassing material with exposure, and reasonably could be explained through the reaction pathways in Figure 6.13 (b, c mechanisms) as these two products could be easily formed by

hydrogen atom transfer between two butyl radicals. Octane can also be created simply by a C-C coupling of two butyl radicals. The reactions between two butyl radicals can occur in the gas phase, but another possible mechanism involves the abstraction of a hydrogen atom by a butyl radical from a butyl group of a tin cage, leading to a radical that can subsequently decompose into butene and a tin-centered radical. The following reaction of these radicals with each other in the system could lead to the formation of butane and octane molecules during the exposure (steps c and d in the proposed reaction mechanisms). These reaction mechanisms could explain the lower rate of octane formation relative to butene (Figure 6.8) at higher doses. The octane formation is a bimolecular process, but butene could additionally be formed through the donation of a hydrogen atom from the butyl radical to the formed tin-centered radicals.

At present, we do not have an explanation for the formation of CO_2. If it would be formed by an oxidation reaction, with the butyl groups as the only possible carbon source, one would expect to find also other reaction products that can be intermediates along this pathway. Moreover, there is only a low background pressure of oxygen in the sample chamber. Another possible explanation is that CO_2 is embedded in the resist film [228] and released due to the chemical conversion or local heating of the film.

We also observed (Figure 6.11) that the thickness of the resist with exposure gradually decreases, with ~2.7 nm reduction occurring at the dose needed for full condensation (45 mJ cm^{-2}). This thickness change is attributed to the escape of the butyl groups from the resist structure, leading to the gradual shrinkage of the resist with exposure.

Assuming that at full exposure, all 12 butyls and all volatile molecules of water are dissociated from the cage structure, then the final product would be a mixture of 6 SnO_2 and 6 SnO, which has a density close to that of SnO_2 (~ 6.95 g cm^{-3}) and SnO (6.45 g cm^{-3}). The density of TinOH crystals has been reported as 1.839 g cm^{-3}, [229] giving a molecular volume of 1473.6 cm^3 mol^{-1}[173, 229]. Therefore, the full exposure is expected to lead to a volume loss of 83% due to the dissociation of organic shells. It is known, however, that the TinOH crystals easily lose the co-crystallized isopropanol. When all co-solvents are assumed to be lost from the film after post-application bake, the molecular volume can be estimated as ~1300 cm^3 mol^{-1}, and the contribution of the organic shell decreases to 80%. Thus, we expect a shrinkage of ~6.7% per butyl group lost.

From Figure 6.11, the initially averaged measured thickness is 23.3 nm, and therefore a full conversion is expected to lead to ~18.6 nm shrinkage. The thickness changes can be considered as a measure of the amount of butyl lost with exposure. Considering the beam diameter used for exposure (5 mm) and the

initial thickness of the resist, we can estimate the number of molecules (~2.12×10^{14}) inside the exposed area, knowing the molecular weight and the density of the resist.

At the dose of 45 mJ cm^{-2} where almost all remaining material has become insoluble in the development process, the film thickness has decreased by ~2.7 nm, which is ~14.5% of the predicted maximum shrinkage (18.6 nm). Thus, only on average ~1.7 of the 12 butyl groups need to be dissociated from the tin cages to render the film fully insoluble. The 14.5% butyl dissociation means escape of ~1.86×10^{15} butyls cm^{-2} from the material. Of the incident dose, 22% is absorbed by the resist film (based on its absorption coefficient of 10.9 μm^{-1}, [64]); therefore, the absorption of at least 0.61 photons per molecule is needed for conversion of the resist to fully insoluble. This corresponds to a quantum yield of ~2.8 Sn- C bond cleavages per absorbed EUV photon. Interestingly, the rapidly decreasing outgassing rate (fig. 6.9) shows that the quantum yield for the first butyl loss is higher than this value average over the dose of 45 mJ cm^{-2}. Zhang et al. [148, 230] reported a quantum yield of 0.55 at 92 eV radiation by counting the total change in the number of atoms in detected Sn-C and C-C bonds in the XPS spectrum for a tin-oxo cage resist exposed to 50 mJ cm^{-2}. They also reported the quantum yield of ~0.09 under DUV (5.5 eV) irradiation. We think the present value is more reliable because the thickness change is measured with fairly high accuracy, in contrast to the carbon loss in XPS spectra. Moreover, the XPS spectra were measured *ex-situ*, which can lead to surface contamination and underestimation of the carbon loss.

In Chapter 5, the total electron yield measurement (TEY) on the resist shows that ~3.5 electrons are generated per absorbed EUV photon. Each electron leaves a hole behind, and both electrons and holes can induce the bond cleavage. Thus, the TEY result suggests a maximum quantum yield of 7 Sn-C dissociations per absorbed photon. Assuming that resist can function with its total conversion efficiency (quantum yield of 7 bond cleavage per absorbed photon) and that the cross-linking mechanism stays the same with exposure, then the maximum resist's thickness in development could already be reached by exposure up to 15 mJ cm^{-2}. Possibly, weak Sn-C bonds can allow such conversion efficiency. Cardineau et al. [66, 71] showed that resist sensitivity correlates directly with the organic ligand bond energy, and enhanced sensitivity is possible using the weaker tin–alkyl bonds with alkyl groups forming more stable radicals.

At the dose value of around 45 mJ cm^{-2}, the maximum of the retained film thickness after development occurs. In one previous study from our laboratory, Haitjema et al. obtained the maximum retained thickness at a EUV dose of 50 mJ cm^{-2} for TinOH and TinOAc films with initial thicknesses of

~40 nm and with no post-exposure bake applied to the films. He also observed a reduction in the thickness of developed films for doses above 100 mJ cm^{-2} [70]. But in the current study by measuring the thickness before development, we could observe that the thickness of the film after exposure to 45 mJ cm^{-2} is already close to that of the developed film, meaning that almost no material is washed out by the development. Thus, the material is sufficiently cross-linked to prevent the escape of still intact tin-oxo cages. Further exposure leads to further hydrocarbon loss and densification, as is apparent from the gradually increasing refractive indices.

6.5 Conclusion

In this work, we used the residual gas analysis technique based on mass spectroscopy to investigate the photon-induced reactions in tin-oxo cage photoresist at 92 eV exposure by determining the outgassing products of the resists. The resist's outgassing rate was also traced at a few selected masses as a connection to the rate of photo-induced reactions. More than 70% of the detected ionic masses were attributed to butene, butane, octane, and carbon dioxide molecules, and we did not observe any tin- containing volatile photo-fragment products.

Based on the contribution percentage and the outgassing rate, we presented some possible reaction pathways that could result in the formation of the outgassing products above-mentioned.

The measurements with higher time resolution reveal that the rate of conversion, as detected via the outgassing ions, decreases rapidly after the first stage of conversion. This is not due to decreased absorption but must be an indication that the reaction products are much less sensitive to EUV than the intact tin cage.

The resist's contrast curve was measured, giving 9 mJ cm^{-2} and 45 mJ cm^{-2} as the dose values corresponding to dose-to-clear and full resist condensation. The observed thickness reduction in the developed resists after the full agglomeration was understood better by measuring the resist's thickness at the same exposed spots before development. Obtaining close thicknesses and refractive indices for the exposed and developed film ensures that the reduction is not due to the resist’s solubility in the developer. The thickness change in resist due to exposure was connected to the number of outgassing butyl groups and the estimated number of absorbed photons. This connection shows that the maximum thickness of resists at 45 mJ cm^{-2} occurs at the expense of 14.5 % cleavage of butyl groups and ~2.8 Sn-C bond dissociations per absorbed EUV photon.

References

[1] S. Tiku, and D. Biswas, *III-V integrated circuit fabrication technology*: CRC Press, (2016).
[2] J. H. Bruning, “Optical lithography: 40 years and holding,” *Proc. SPIE,* 6520, 62-74, (2007).
[3] V. Bakshi, *EUV lithography*, (2009).
[4] C. Mack, *Fundamental principles of optical lithography: the science of microfabrication*: John Wiley & Sons, (2007).
[5] B. Lin, *Optical Lithography: Here Is Why*: SPIE Press Books, (2010).
[6] H. J. Levinson, *Principles of lithography*: SPIE Press Books, (2005).
[7] M. Rothschild, T. Bloomstein, R. Kunz, V. Liberman, M. Switkes, S. Palmacci, J. Sedlacek, D. Hardy, and A. Grenville, “Liquid immersion lithography: Why, how, and when?,” *J. Vac. Sci. Technol. B,* 22, 2877-81, (2004).
[8] M. Switkes, R. Kunz, M. Rothschild, R. Sinta, M. Yeung, and S.-Y. Baek, “Extending optics to 50 nm and beyond with immersion lithography,” *J. Vac. Sci. Technol. B,* 21, 2794-9, (2003).
[9] Y. Wei, “Extendibility of 193 nm immersion lithography,” *SPIE newsroom,* 10, 0974, (2008).
[10] Y. Wei, and D. Back, “193 nm immersion lithography: Status and challenges,” *SPIE Newsroom,* (2007).
[11] J. de Klerk, C. Wagner, R. Droste, L. Levasier, L. Jorritsma, E. van Setten, H. Kattouw, J. Jacobs, and T. Heil, “Performance of a 1.35 NA ArF immersion lithography system for 40-nm applications,” *Proc. SPIE,* 6520, 742-55, (2007).
[12] S. Migura, *Optics for EUV Lithography*, Carl Zeiss SMT GmbH, EUVL Workshop in Berkeley, CA, USA, (2018).
[13] D. Z. Pan, L. Liebmann, B. Yu, X. Xu, and Y. Lin, “Pushing multiple patterning in sub-10nm: Are we ready?,” *2015 52nd ACM/EDAC/IEEE Design Automation Conference (DAC)*, 1-6, (2015).
[14] R. de Graaf, S. Weichselbaum, R. Droste, M. McLaren, B. Koek, and W. de Boeij, “NXT: 1980Di immersion scanner for 7 nm and 5 nm production nodes,” *Proc. SPIE,* 9780, 98-106, (2016).
[15] S. Owa, S. Wakamoto, M. Murayama, H. Yaegashi, and K. Oyama, “Immersion lithography extension to sub-10 nm nodes with multiple patterning,” *Proc. SPIE,* 9052, 179-87, (2014).
[16] C. Wagner, N. Harned, P. Kuerz, M. Lowisch, H. Meiling, D. Ockwell, R. Peeters, K. van Ingen-Schenau, E. van Setten, and J. Stoeldraijer, “EUV into production with ASML's NXE platform,” *Proc. SPIE,* 7636, 512-23, (2010).
[17] C. Wagner, J. Bacelar, N. Harned, E. Loopstra, S. Hendriks, I. De Jong, P. Kuerz, L. Levasier, M. van de Kerkhof, and M. Lowisch, “EUV lithography at chipmakers has started: performance validation of ASML's NXE: 3100,” *Proc. SPIE,* 7969, 499-510, (2011).
[18] B. Wu, and A. Kumar, *Extreme ultraviolet lithography*: McGraw-Hill Education, (2009).
[19] I. Fomenkov, “EUV source for lithography in HVM: performance and prospects,” *Proc. 2019 Source Workshop, S1*, (2019).
[20] T. Feigl, S. Yulin, N. Benoit, N. Kaiser, N. R. Böwering, A. I. Ershov, V. Khodykin, J. W. Viatella, K. Bruzzone, and I. V. Fomenkov, “High-temperature LPP collector mirror,” *Proc. SPIE,* 6151, 1122-30, (2006).
[21] H. Mizoguchi, J. Fujimoto, and T. Saitou, “LPP-EUV light source development for high volume manufacturing lithography,” *J. Laser Appl.*, 2012, 11-20, (2012).

[22] I. Fomenkov, D. Brandt, A. Ershov, A. Schafgans, Y. Tao, G. Vaschenko, S. Rokitski, M. Kats, M. Vargas, and M. Purvis, “Light sources for high-volume manufacturing EUV lithography: technology, performance, and power scaling,” *Adv. Opt. Technol,* 6, 173-86, (2017).

[23] O. Semprez, J. Jonkers, R. Apetz, and M. Yoshioka, “Making extreme-UV lightsources a reality,” *SPIE Newsroom,* (2012).

[24] J. Van Schoot, C. Zahlten, P. Gräupner, P. Kürz, J. Stoeldraijer, and W. Kaiser, “High-NA EUV lithography pushing the limits,” *Proc. SPIE*, 11177, 111770B, (2019).

[25] S. Wurm, “EUV lithography development and research challenges for the 22 nm half-pitch,” *J. Photopolym. Sci.Technol.,* 22, 31-42, (2009).

[26] S. Wurm, “EUV lithography: progress, challenges, and outlook,” *Proc. SPIE*, 9231, 15-21, (2014).

[27] S. Harilal, B. O’Shay, and M. S. Tillack, “Debris mitigation in a laser-produced tin plume using a magnetic field,” *J. Appl. Phys.,* (2005).

[28] M. Mastenbroek, “EUV industrialization high volume manufacturing with NXE3400B,” *Proc. SPIE*, 10809, 5-20, (2018).

[29] D. C. Brandt, I. Fomenkov, and J. Stewart, “Progress in availably of NXE: 3400B EUVL sources in the field and power scaling towards 500 W,” *Proc. SPIE*, 11323, 113230W, (2020).

[30] H. Song, L. Zavyalova, I. Su, J. Shiely, and T. Schmoeller, “Shadowing effect modeling and compensation for EUV lithography,” *Proc. SPIE*, 7969, 580-8, (2011).

[31] H. Kang, S. Hansen, J. van Schoot, and K. van Ingen Schenau, “EUV simulation extension study for mask shadowing effect and its correction,” *Proc. SPIE*, 6921, 978-88, (2008).

[32] W. Eschen, L. Loetgering, V. Schuster, R. Klas, A. Kirsche, L. Berthold, M. Steinert, T. Pertsch, H. Gross, and M. Krause, “Material-specific high-resolution table-top extreme ultraviolet microscopy,” *Light Sci. Appl,* 11, 1-10, (2022).

[33] M. Upadhyaya, V. Jindal, A. Basavalingappa, H. Herbol, J. Harris-Jones, I.-Y. Jang, K. A. Goldberg, I. Mochi, S. Marokkey, and W. Demmerle, “Evaluating printability of buried native EUV mask phase defects through a modeling and simulation approach,” *Proc. SPIE*, 9422, 204-17, (2015).

[34] J. Lee, J. Kim, S. Jeong, M. Lim, S. Koo, C.-M. Lim, and Y.-S. Kim, “Study on RLS trade-off resist upgrade for production ready EUV lithography,” *Proc. SPIE*, 9776, 612-7, (2016).

[35] B. Rice, "Extreme ultraviolet (EUV) lithography," *Nanolithography*, 42-79: Elsevier, (2014).

[36] T. G. Oyama, A. Oshima, and S. Tagawa, “Estimation of resist sensitivity for extreme ultraviolet lithography using an electron beam,” *AIP Advances,* 6, 085210, (2016).

[37] D. P. Sanders, “Advances in patterning materials for 193 nm immersion lithography,” *Chem. Rev.,* 110, 321-60, (2010).

[38] K. Furukawa, T. Kozawa, and S. Tagawa, “Evaluation of alcoholic hydroxyl derivatives for chemically amplified extreme ultraviolet resist,” *Proc. SPIE*, 7273, 555-66, (2009).

[39] T. Manouras, and P. Argitis, “High sensitivity resists for EUV lithography: A review of material design strategies and performance results,” *Nanomaterials,* 10, 1593, (2020).

[40] D. De Simone, A. M. Goethals, F. Van Roey, T. Zheng, P. Foubert, E. Hendrickx, G. Vandenberghe, and K. Ronse, “Progresses and challenges of EUV lithography materials,” *J. Photopolym. Sci.Technol.,* 27, 601-10, (2014).

[41] R. L. Brainard, P. Trefonas, J. H. Lammers, C. A. Cutler, J. F. Mackevich, A. Trefonas, and S. A. Robertson, “Shot noise, LER, and quantum efficiency of EUV photoresists,” *Proc. SPIE*, 5374, 74-85, (2004).

[42] J. Jiang, G. Giordano, R. Fallica, D. DeSimone, and G. Vandenberghe, "Sensitizer for EUV Chemically Amplified Resist: Metal versus Halogen," *J. Photopolym. Sci.Technol.,* 32, 21-5, (2019).

[43] S. Kruger, S. Revuru, C. Higgins, S. Gibbons, D. A. Freedman, W. Yueh, T. R. Younkin, and R. L. Brainard, "Fluorinated acid amplifiers for EUV lithography," *J. Am. Chem. Soc.,* 131, 9862-3, (2009).

[44] H. Yamamoto, T. Kozawa, S. Tagawa, H. Yukawa, M. Sato, and J. Onodera, "Enhancement of acid production in chemically amplified resist for extreme ultraviolet lithography," *Appl. Phys. Express,* 1, 047001, (2008).

[45] M. Echigo, and D. Oguro, "Development of new phenylcalix [4] resorcinarene: its application to positive-tone molecular resist for EB and EUV lithography," *Proc. SPIE*, 7273, 796-807, (2009).

[46] H. Kudo, N. Nina, T. Sato, H. Oizumi, T. Itani, T. Miura, T. Watanabe, and H. Kinoshita, "Extreme Ultraviolet (EUV)-Resist Material Based on Noria (Water Wheel-like Macrocycle) Derivatives with Pendant Alkoxyl and Adamantyl Ester Groups," *J. Photopolym. Sci.Technol.,* 25, 587-92, (2012).

[47] H. Kudo, Y. Suyama, H. Oizumi, T. Itani, and T. Nishikubo, "Novel extreme ultraviolet (EUV)-resist material based on noria (water wheel-like cyclic oligomer)," *J. Mater. Chem.,* 20, 4445-50, (2010).

[48] D. P. Green, V. Jain, B. Bailey, M. Wagner, M. Clark, D. Valeri, and S. Lakso, "Development of molecular resist derivatives for EUV lithography," *Proc. SPIE*, 8679, 269-81, (2013).

[49] R. Fallica, J. Haitjema, L. Wu, S. Castellanos, F. Brouwer, and Y. Ekinci, "Absorption coefficient and exposure kinetics of photoresists at EUV," *Proc. SPIE*, 10143, 29-39, (2017).

[50] C. Luo, C. Xu, L. Lv, H. Li, X. Huang, and W. Liu, "Review of recent advances in inorganic photoresists," *RSC Adv.,* 10, 8385-95, (2020).

[51] S. Castellanos, L. Wu, M. Baljozovic, G. Portale, D. Kazazis, M. Vockenhuber, Y. Ekinci, and T. Jung, "Ti, Zr, and Hf-based molecular hybrid materials as EUV photoresists," *Proc. SPIE*, 10583, 58-69, (2018).

[52] J. Jiang, S. Chakrabarty, M. Yu, and C. K. Ober, "Metal oxide nanoparticle photoresists for EUV patterning," *J. Photopolym. Sci.Technol.,* 27, 663-6, (2014).

[53] L. Li, S. Chakrabarty, K. Spyrou, C. K. Ober, and E. P. Giannelis, "Studying the mechanism of hybrid nanoparticle photoresists: effect of particle size on photopatterning," *Chem. Mater.,* 27, 5027-31, (2015).

[54] J. Passarelli, M. Murphy, R. Del Re, M. M. Sortland, J. Hotalen, L. Dousharm, R. Fallica, Y. Ekinci, M. Neisser, and D. A. Freedman, "Organometallic carboxylate resists for extreme ultraviolet with high sensitivity," *J. Micro/Nanolith. MEMS MOEMS,* 14, 043503, (2015).

[55] A. Grenville, J. T. Anderson, B. L. Clark, P. De Schepper, J. Edson, M. Greer, K. Jiang, M. Kocsis, S. T. Meyers, and J. K. Stowers, "Integrated fab process for metal oxide EUV photoresist," *Proc. SPIE*, 9425, 225-32, (2015).

[56] W. D. Hinsberg, and S. Meyers, "A numeric model for the imaging mechanism of metal oxide EUV resists," *Proc. SPIE*, 10146, 14-24, (2017).

[57] N. Thakur, M. Vockenhuber, Y. Ekinci, B. Watts, A. Giglia, N. Mahne, S. Nannarone, S. Castellanos, and A. M. Brouwer, "Fluorine-Rich Zinc Oxoclusters as Extreme Ultraviolet Photoresists: Chemical Reactions and Lithography Performance," *ACS Materials Au,* 2, 343-55, (2022).

[58] N. Thakur, R. Bliem, I. Mochi, M. Vockenhuber, Y. Ekinci, and S. Castellanos, "Mixed-ligand zinc-oxoclusters: efficient chemistry for high resolution nanolithography," *J. Mater. Chem. C,* 8, 14499-506, (2020).

[59] A. Narasimhan, S. Grzeskowiak, B. Srivats, H. C. Herbol, L. Wisehart, C. Kelly, W. Earley, L. E. Ocola, M. Neisser, and G. Denbeaux, "Studying secondary electron behavior in EUV resists using experimentation and modeling," *Proc. SPIE*, 9422, 27-38, (2015).

[60] R. Gronheid, T. R. Younkin, M. J. Leeson, C. Fonseca, J. S. Hooge, K. Nafus, J. J. Biafore, and M. D. Smith, "EUV secondary electron blur at the 22 nm half pitch node," *Proc. SPIE*, 7969, 40-50, (2011).

[61] S. T. Meyers, J. T. Anderson, B. Cardineau, J. B. Edson, K. Jiang, D. A. Keszler, and A. J. Telecky, *Organotin oxide hydroxide patterning compositions, precursors, and patterning*, US Patent 0371439 A1, (2020).

[62] S. T. Meyers, J. T. Anderson, J. B. Edson, K. Jiang, D. A. Keszler, M. K. Kocsis, A. J. Telecky, and B. Cardineau, *Organometallic solution based high resolution patterning compositions and corresponding methods*, US Patent 0116839 A1, (2015).

[63] S. T. Meyers, D. A. Keszler, K. Jiang, J. T. Anderson, and A. Grenville, *Organometallic solution based high resolution patterning compositions*, US Patent 0056542 A1, (2013).

[64] R. Fallica, J. Haitjema, L. Wu, S. Castellanos, A. M. Brouwer, and Y. Ekinci, "Absorption coefficient of metal-containing photoresists in the extreme ultraviolet," *J. Micro/Nanolith. MEMS MOEMS,* 17, 023505, (2018).

[65] R. T. Frederick, S. Saha, J. T. Diulus, F. Luo, J. M. Amador, M. Li, D.-H. Park, E. L. Garfunkel, D. A. Keszler, and G. S. Herman, "Thermal and radiation chemistry of butyltin oxo hydroxo: A model inorganic photoresist," *Microelectron. Eng.,* 205, 26-31, (2019).

[66] B. Cardineau, R. Del Re, H. Al-Mashat, M. Marnell, M. Vockenhuber, Y. Ekinci, C. Sarma, M. Neisser, D. A. Freedman, and R. L. Brainard, "EUV resists based on tin-oxo clusters," *Proc. SPIE*, 9051, 335-46, (2014).

[67] R. Del Re, M. Sortland, J. Pasarelli, B. Cardineau, Y. Ekinci, M. Vockenhuber, M. Neisser, D. Freedman, and R. L. Brainard, "Low-LER tin carboxylate photoresists using EUV," *Proc. SPIE*, 9422, 654-63, (2015).

[68] J. H. Ma, C. Needham, H. Wang, A. Neureuther, D. Prendergast, and P. Naulleau, "Mechanistic Advantages of Organotin Molecular EUV Photoresists," *ACS Appl. Mater. Interfaces,* 14, 5514-24, (2022).

[69] M. C. Sharps, R. T. Frederick, M. L. Javitz, G. S. Herman, D. W. Johnson, and J. E. Hutchison, "Organotin carboxylate reagents for nanopatterning: chemical transformations during direct-write electron beam processes," *Chem. Mater.,* 31, 4840-50, (2019).

[70] J. Haitjema, Y. Zhang, M. Vockenhuber, D. Kazazis, Y. Ekinci, and A. M. Brouwer, "Extreme ultraviolet patterning of tin-oxo cages," *J. Micro/Nanolith. MEMS MOEMS,* 16, 033510, (2017).

[71] B. Cardineau, R. Del Re, M. Marnell, H. Al-Mashat, M. Vockenhuber, Y. Ekinci, C. Sarma, D. A. Freedman, and R. L. Brainard, "Photolithographic properties of tin-oxo clusters using extreme ultraviolet light (13.5 nm)," *Microelectron. Eng.,* 127, 44-50, (2014).

[72] R. Fallica, J. K. Stowers, A. Grenville, A. Frommhold, A. P. Robinson, and Y. Ekinci, "Dynamic absorption coefficients of chemically amplified resists and nonchemically amplified resists at extreme ultraviolet," *J. Micro/Nanolith. MEMS MOEMS,* 15, 033506, (2016).

[73] J. Haitjema, Y. Zhang, N. Ottosson, and A. M. Brouwer, "Photoreactions of tin oxo cages, model EUV photoresists," *J. Photopolym. Sci.Technol.,* 30, 99-102, (2017).

[74] J. Haitjema, L. Wu, A. Giuliani, L. Nahon, S. Castellanos, and A. M. Brouwer, "UV and VUV-induced fragmentation of tin-oxo cage ions," *Phys. Chem. Chem. Phys.,* 23, 20909-18, (2021).

[75] Y. Zhang, J. Haitjema, M. Baljozovic, M. Vockenhuber, D. Kazazis, T. A. Jung, Y. Ekinci, and A. M. Brouwer, "Dual-tone application of a tin-oxo cage photoresist under E-beam and EUV exposure," *J. Photopolym. Sci.Technol.,* 31, 249-55, (2018).

[76] I. Bespalov, Y. Zhang, J. Haitjema, R. M. Tromp, S. J. van der Molen, A. M. Brouwer, J. Jobst, and S. Castellanos, "Key role of very low energy electrons in tin-based molecular resists for extreme ultraviolet nanolithography," *ACS Appl. Mater. Interfaces,* 12, 9881-9, (2020).

[77] J. Li, J. Lu, A. Chew, S. Han, J. Li, Y. Wu, H. Wang, S. Ghimire, and Z. Chang, "Attosecond science based on high harmonic generation from gases and solids," *Nat. Commun.,* 11, 1-13, (2020).

[78] J. Marangos, "Development of high harmonic generation spectroscopy of organic molecules and biomolecules," *J. Phys. B: At. Mol. Opt. Phys.,* 49, 132001, (2016).

[79] B. E. Saleh, and M. C. Teich, *Fundamentals of photonics*: John Wiley & sons, (2019).

[80] S. Witte, and K. S. Eikema, "Ultrafast optical parametric chirped-pulse amplification," *IEEE Journal of Selected Topics in Quantum Electronics,* 18, 296-307, (2011).

[81] P. B. Corkum, "Plasma perspective on strong field multiphoton ionization," *Phys. Rev. Lett.,* 71, 1994, (1993).

[82] J. L. Krause, K. J. Schafer, and K. C. Kulander, "High-order harmonic generation from atoms and ions in the high intensity regime," *Phys. Rev. Lett.,* 68, 3535, (1992).

[83] V. E. Gruzdev, "Laser-induced ionization of solids: back to Keldysh," *Proc. SPIE*, 5647, 480-92, (2005).

[84] C. Heyl, *Scaling and gating attosecond pulse generation*: Lund University, (2014).

[85] D. B. Khuong, and D. Van Lap, "Phase-matched High Order Harmonic Generation and Application," Nova Science Publishers, Incorporated, (2013).

[86] M. Lewenstein, P. Balcou, M. Y. Ivanov, A. L'huillier, and P. B. Corkum, "Theory of high-harmonic generation by low-frequency laser fields," *Phys. Rev. A,* 49, 2117, (1994).

[87] R. Santra, and A. Gordon, "Three-step model for high-harmonic generation in many-electron systems," *Phys. Rev. Lett.,* 96, 073906, (2006).

[88] W. Hong, P. Lu, P. Lan, Z. Yang, Y. Li, and Q. Liao, "Broadband XUV supercontinuum generation via controlling quantum paths by a low-frequency field," *Phys. Rev. A,* 77, 033410, (2008).

[89] E. Georgiadou, "Study of harmonic generation with a two-color field," *Lund Reports in Atomic Physics,* (2007).

[90] T. Popmintchev, M.-C. Chen, A. Bahabad, M. Gerrity, P. Sidorenko, O. Cohen, I. P. Christov, M. M. Murnane, and H. C. Kapteyn, "Phase matching of high harmonic generation in the soft and hard X-ray regions of the spectrum," *PNAS, Appl. Phys.,* 106, 10516-21, (2009).

[91] S. Kazamias, S. Daboussi, O. Guilbaud, K. Cassou, D. Ros, B. Cros, and G. Maynard, "Pressure-induced phase matching in high-order harmonic generation," *Phys. Rev. A,* 83, 063405, (2011).

[92] C.-D. Lin, C. Jin, A.-T. Le, and H. Wei, *Attosecond and strong-field physics: principles and applications*: Cambridge University Press, (2018).

[93] S. D. C. Roscam Abbing, F. Campi, F. S. Sajjadian, N. Lin, P. Smorenburg, and P. M. Kraus, "Divergence control of high-harmonic generation," *Phys. Rev. Appl,* 13, 054029, (2020).

[94] S. D. C. Roscam Abbing, F. Campi, A. Zeltsi, P. Smorenburg, and P. M. Kraus, "Divergence and efficiency optimization in polarization-controlled two-color high-harmonic generation," *Sci. Rep.,* 11, 1-11, (2021).

[95] J. Haitjema, L. Wu, A. Giuliani, L. Nahon, S. Castellanos, and A. M. Brouwer, "Photo-induced fragmentation of a Tin-oxo cage compound," *J. Photopolym. Sci.Technol.,* 31, 243-7, (2018).

[96] B. L. Henke, E. M. Gullikson, and J. C. Davis, "X-ray interactions: photoabsorption, scattering, transmission, and reflection at E= 50-30,000 eV, Z= 1-92," *At. Data Nucl. Data Tables,* 54, 181-342, (1993).

[97] H. Wang, M. Chini, S. Chen, C.-H. Zhang, F. He, Y. Cheng, Y. Wu, U. Thumm, and Z. Chang, "Attosecond time-resolved autoionization of argon," *Phys. Rev. Lett.,* 105, 143002, (2010).

[98] R. Verma, and A. Chanda, "Technique to study Rydberg states by multiphoton ionization spectroscopy," *JOSA B,* 5, 86-90, (1988).

[99] H. Lefebvre-Brion, *Perturbations in the spectra of diatomic molecules*: Elsevier, (2012).

[100] T. Luke, "Autoionization states in the photoionization of neon," *J. Phys. B: At. Mol. Opt. Phys.,* 6, 30, (1973).

[101] J. McConkey, and J. Preston, "Autoionizing states in argon (Electron scattering)," *J. Phys. B: At. Mol. Opt. Phys.,* 6, L138, (1973).

[102] P. Lambropoulos, and P. Zoller, "Autoionizing states in strong laser fields," *Phys. Rev. A,* 24, 379, (1981).

[103] R. Madden, D. Ederer, and K. Codling, "Resonances in the photo-ionization continuum of Ar I (20-150 eV)," *Physical Review,* 177, 136, (1969).

[104] X. Wang, M. Chini, Y. Cheng, Y. Wu, and Z. Chang, "In situ calibration of an extreme ultraviolet spectrometer for attosecond transient absorption experiments," *Appl. Opt,* 52, 323-9, (2013).

[105] L. Rading, "An intense attosecond light source-from generation to application," Lund University, Doctoral thesis, (2016).

[106] F. Frassetto, S. Coraggia, S. Dziarzhytski, N. Gerasimova, and L. Poletto, "Extreme-ultraviolet compact spectrometer for the characterization of the harmonics content in the free-electron-laser radiation at FLASH," *J. Synchrotron Rad.,* 19, 596-601, (2012).

[107] F. Scholze, H. Rabus, and G. Ulm, "Mean energy required to produce an electron-hole pair in silicon for photons of energies between 50 and 1500 eV," *J. Appl. Phys.,* 84, 2926-39, (1998).

[108] M. Newberry. "Pixel Response Effects on CCD Camera Gain Calibration," Technical Note (Mirametrics, 1998); http://www.mirametrics.com/tech_note_ccdgain.htm.

[109] M. Newberry, "Tech note: pixel response effects on CCD camera gain calibration," *Mirametrics Inc., Copy right,* (1998).

[110] F. de Groot, and A. Kotani, *Core level spectroscopy of solids*: CRC press, (2008).

[111] A. P. Hitchcock, and J. J. Neville, *Photoionization dynamics from inner-shell mass-spectrometry*: World Scientific: Singapore, (2002).

[112] J. Stöhr, *NEXAFS spectroscopy*: Springer Science & Business Media, (1992).

[113] J. M. Sturm, F. Liu, E. Darlatt, M. Kolbe, A. A. Aarnink, C. J. Lee, and F. Bijkerk, "Extreme UV secondary electron yield measurements of Ru, Sn, and Hf oxide thin films," *J. Micro/Nanolith. MEMS MOEMS,* 18, 033501, (2019).

[114] B. Yakshinskiy, R. Wasielewski, E. Loginova, and T. E. Madey, "Carbon accumulation and mitigation processes, and secondary electron yields of ruthenium surfaces," *Proc. SPIE*, 6517, 875-85, (2007).

[115] G. Akgül, F. Aksoy, A. Bozduman, O. Ozkendir, Y. Ufuktepe, and J. Lüning, "Study of the L2, 3 edges of 3d transition metals by X-ray absorption spectroscopy," *Thin Solid Films,* 517, 1000-4, (2008).

[116] A. Erbil, G. Cargill Iii, R. Frahm, and R. Boehme, "Total-electron-yield current measurements for near-surface extended x-ray-absorption fine structure," *Phys. Rev. B,* 37, 2450, (1988).

[117] M. Pompa, A. Flank, P. Lagarde, J. Rife, I. Stekhin, M. Nakazawa, H. Ogasawara, and A. Kotani, "Experimental and theoretical comparison between absorption, total electron yield, and fluorescence spectra of rare-earth M 5 edges," *Phys. Rev. B,* 56, 2267, (1997).
[118] T. Sham, and R. Carr, "Total electron yield measurements of extended x-ray absorption fine structures (EXAFS) of Ni and Fe thin foils, and adsorption of Ni on polycrystalline Fe substrates," *J. Chem. Phys.,* 83, 5914-22, (1985).
[119] B. Thole, G. Van der Laan, J. Fuggle, G. Sawatzky, R. Karnatak, and J.-M. Esteva, "3d x-ray-absorption lines and the $3d^9\ 4f^{n+1}$ multiplets of the lanthanides," *Phys. Rev. B,* 32, 5107, (1985).
[120] M. Abbate, J. Goedkoop, F. De Groot, M. Grioni, J. Fuggle, S. Hofmann, H. Petersen, and M. Sacchi, "Probing depth of soft x-ray absorption spectroscopy measured in total-electron-yield mode," *Surf. Interface Anal.,* 18, 65-9, (1992).
[121] R. Nakajima, J. Stöhr, and Y. U. Idzerda, "Electron-yield saturation effects in L-edge x-ray magnetic circular dichroism spectra of Fe, Co, and Ni," *Phys. Rev. B,* 59, 6421, (1999).
[122] A. Ruosi, C. Raisch, A. Verna, R. Werner, B. Davidson, J. Fujii, R. Kleiner, and D. Koelle, "Electron sampling depth and saturation effects in perovskite films investigated by soft x-ray absorption spectroscopy," *Phys. Rev. B,* 90, 125120, (2014).
[123] J. Vogel, and M. Sacchi, "Experimental estimate of absorption length and total electron yield (TEY) probing depth in dysprosium," *J. Electron Spectrosc. Relat. Phenom.,* 67, 181-8, (1994).
[124] S. Zheng, S. Hayakawa, and Y. Gohshi, "An experimental comparison of the total-electron-yield and conversion-electron-yield modes for near-surface characterization using X-ray excitation," *J. Electron Spectrosc. Relat. Phenom.,* 87, 81-9, (1997).
[125] W. Gudat, and C. Kunz, "Close similarity between photoelectric yield and photoabsorption spectra in the soft-x-ray range," *Phys. Rev. Lett.,* 29, 169, (1972).
[126] Y. Ufuktepe, G. Akgül, and J. Lüning, "X-ray photoabsorption and total electron yield of Fe thin films at the L2, 3 edge," *J. Alloys Compd.,* 401, 193-6, (2005).
[127] S. Hofmann, *Auger-and X-ray photoelectron spectroscopy in materials science: a user-oriented guide*: Springer Science & Business Media, (2012).
[128] J. M. Hollander, and W. L. Jolly, "X-ray photoelectron spectroscopy," *Acc. Chem. Res.,* 3, 193-200, (1970).
[129] P. Van der Heide, *X-ray photoelectron spectroscopy: an introduction to principles and practices*: John Wiley & Sons, (2011).
[130] "https://www.elettra.trieste.it/it/lightsources/elettra/elettra-beamlines/bear/beamline-description.html."
[131] M. Tyona, "A theoretical study on spin coating technique," *J. Adv. Mater. Res,* 2, 195, (2013).
[132] Y. Yan, J. Li, Q. Liu, and P. Zhou, "Evaporation Effect on Thickness Distribution for Spin-Coated Films on Rectangular and Circular Substrates," *Coatings,* 11, 1322, (2021).
[133] L. J.A. Woollam Co. Inc., "CompleteEASE™ Data Analysis Manual, Version 4.63," *N.E. , 2011, 45*.
[134] H. Fujiwara, *Spectroscopic ellipsometry: principles and applications*: John Wiley & Sons, (2007).
[135] H.-J. Butt, K. Graf, and M. Kappl, *Physics and chemistry of interfaces*: John Wiley & Sons, (2013).
[136] G. Harland, and A. Tompinks, "A User's Guide to Ellipsometry," Academic Press: San Diego, (1993).
[137] B. Johs, J. A. Woollam, C. M. Herzinger, J. N. Hilfiker, R. A. Synowicki, and C. L. Bungay, "Overview of variable-angle spectroscopic ellipsometry (VASE): II. Advanced applications," *Proc. SPIE* 10294, 1029404, (1999).

[138] J. A. Woollam, B. D. Johs, C. M. Herzinger, J. N. Hilfiker, R. A. Synowicki, and C. L. Bungay, "Overview of variable-angle spectroscopic ellipsometry (VASE): I. Basic theory and typical applications," *Proc. SPIE* 10294, 1029402, (1999).

[139] Y. Zhang, J. Haitjema, S. Castellanos, O. Lugier, N. Sadegh, R. Ovsyannikov, E. Giangrisostomi, F. O. Johansson, E. Berggren, and A. Lindblad, "Extreme ultraviolet photoemission of a tin-based photoresist," *Appl. Phys. Lett,* 118, 171903, (2021).

[140] A. Lio, "EUV photoresists: A progress report and future prospects," *Synchrotron Rad. News,* 32, 9-14, (2019).

[141] J. Stowers, and D. A. Keszler, "High resolution, high sensitivity inorganic resists," *Microelectron. Eng.,* 86, 730-3, (2009).

[142] M. E. Krysak, J. M. Blackwell, S. E. Putna, M. J. Leeson, T. R. Younkin, S. Harlson, K. Frasure, and F. Gstrein, "Investigation of novel inorganic resist materials for EUV lithography," *Proc. SPIE,* 9048, 904805, (2014).

[143] R. P. Oleksak, R. E. Ruther, F. Luo, J. M. Amador, S. R. Decker, M. N. Jackson, J. R. Motley, J. K. Stowers, D. W. Johnson, and E. L. Garfunkel, "Evaluation of Thermal and Radiation Induced Chemistries of Metal Oxo–Hydroxo Clusters for Next-Generation Nanoscale Inorganic Resists," *ACS Appl. Nano Mater.,* 1, 4548-56, (2018).

[144] N. Thakur, L.-T. Tseng, M. Vockenhuber, Y. Ekinci, and S. Castellanos, "Stability studies on a sensitive EUV photoresist based on zinc metal oxoclusters," *J. Micro/Nanolith. MEMS MOEMS,* 18, 043504, (2019).

[145] L. Wu, M. Baljozovic, G. Portale, D. Kazazis, M. Vockenhuber, T. Jung, Y. Ekinci, and S. C. Ortega, "Mechanistic insights in Zr-and Hf-based molecular hybrid EUV photoresists," *J. Micro/Nanolith. MEMS MOEMS,* 18, 013504, (2019).

[146] F. Banse, F. Ribot, P. Toledano, J. Maquet, and C. Sanchez, "Hydrolysis of monobutyltin trialkoxides: Synthesis and characterizations of $\{(BuSn)_{12}O_{14}(OH)_6\}(OH)_2$," *Inorg. Chem.,* 34, 6371-9, (1995).

[147] C. Eychenne-Baron, F. Ribot, and C. Sanchez, "New synthesis of the nanobuilding block {(BuSn) 12O14 (OH)6}2+ and exchange properties of {(BuSn)12O14 (OH)6}(O3SC6H4CH3)2," *J. Organomet. Chem.,* 567, 137-42, (1998).

[148] Y. Zhang, J. Haitjema, X. Liu, F. Johansson, A. Lindblad, S. Castellanos, N. Ottosson, and A. M. Brouwer, "Photochemical conversion of tin-oxo cage compounds studied using hard x-ray photoelectron spectroscopy," *J. Micro/Nanolith. MEMS MOEMS,* 16, 023510, (2017).

[149] J. T. Diulus, R. T. Frederick, M. Li, D. C. Hutchison, M. R. Olsen, I. Lyubinetsky, L. Árnadóttir, E. L. Garfunkel, M. Nyman, and H. Ogasawara, "Ambient-Pressure X-ray Photoelectron Spectroscopy Characterization of Radiation-Induced Chemistries of Organotin Clusters," *ACS Appl. Mater. Interfaces,* 11, 2526-34, (2018).

[150] J. Haitjema, Y. Zhang, M. Vockenhuber, D. Kazazis, Y. Ekinci, and A. Brouwer, "Tin-oxo cages for use as photoresists in EUV lithography," *J. Micro/Nanolith. MEMS MOEMS,* 16, 033510, (2017).

[151] P. M. Kraus, M. Zürch, S. K. Cushing, D. M. Neumark, and S. R. Leone, "The ultrafast X-ray spectroscopic revolution in chemical dynamics," *Nat. Rev. Chem.,* 2, 82-94, (2018).

[152] C. J. Kaplan, P. M. Kraus, A. D. Ross, M. Zürch, S. K. Cushing, M. F. Jager, H.-T. Chang, E. M. Gullikson, D. M. Neumark, and S. R. Leone, "Femtosecond tracking of carrier relaxation in germanium with extreme ultraviolet transient reflectivity," *Phys. Rev. B,* 97, 205202, (2018).

[153] D. Dakternieks, H. Zhu, E. R. Tiekink, and R. Colton, "Synthesis, structure and reactions of [(BuSn) 12O14 (OH) 6] Cl2· 2H2O: Solution studies using 119Sn NMR and electrospray mass spectrometry," *J. Organomet. Chem.,* 476, 33-40, (1994).
[154] Y.-J. Kwark, J. P. Bravo-Vasquez, M. Chandhok, H. Cao, H. Deng, E. Gullikson, and C. K. Ober, "Absorbance measurement of polymers at extreme ultraviolet wavelength: correlation between experimental and theoretical calculations," *J. Vac. Sci. Technol. B,* 24, 1822-6, (2006).
[155] F. H. Dill, W. P. Hornberger, P. S. Hauge, and J. M. Shaw, "Characterization of positive photoresist," *IEEE Trans. Electron Devices,* 22, 445-52, (1975).
[156] J. Yeh, and I. Lindau, "Atomic subshell photoionization cross sections and asymmetry parameters: $1 \leqslant Z \leqslant 103$," *Atomic data and nuclear data tables,* 32, 1-155, (1985).
[157] "https://vuo.elettra.trieste.it/services/elements/WebElements.html,"
[158] K. D. Closser, D. F. Ogletree, P. Naulleau, and D. Prendergast, "The importance of inner-shell electronic structure for enhancing the EUV absorption of photoresist materials," *J. Chem. Phys.,* 146, 164106, (2017).
[159] A. V. Pret, M. Kocsis, D. De Simone, G. Vandenberghe, J. Stowers, A. Giglia, P. de Schepper, A. Mani, and J. J. Biafore, "Characterizing and modeling electrical response to light for metal-based EUV photoresists," *Proc. SPIE*, 9779, 977906, (2016).
[160] P. M. Kraus, and H. J. Wörner, "Perspectives of attosecond spectroscopy for the understanding of fundamental electron correlations," *Angew. Chem. Int. Ed.,* 57, 5228-47, (2018).
[161] H. J. Wörner, C. A. Arrell, N. Banerji, A. Cannizzo, M. Chergui, A. K. Das, P. Hamm, U. Keller, P. M. Kraus, and E. Liberatore, "Charge migration and charge transfer in molecular systems," *Struct. Dyn.,* 4, 061508, (2017).
[162] N. Saito, H. Sannohe, N. Ishii, T. Kanai, N. Kosugi, Y. Wu, A. Chew, S. Han, Z. Chang, and J. Itatani, "Real-time observation of electronic, vibrational, and rotational dynamics in nitric oxide with attosecond soft x-ray pulses at 400 eV," *Optica,* 6, 1542-6, (2019).
[163] K. Zhang, R. Ash, G. S. Girolami, and J. Vura-Weis, "Tracking the Metal-Centered Triplet in Photoinduced Spin Crossover of $Fe(phen)_3^{2+}$ with Tabletop Femtosecond M-Edge X-ray Absorption Near-Edge Structure Spectroscopy," *J. Am. Chem. Soc.,* 141, 17180-8, (2019).
[164] M. Zürch, H.-T. Chang, L. J. Borja, P. M. Kraus, S. K. Cushing, A. Gandman, C. J. Kaplan, M. H. Oh, J. S. Prell, and D. Prendergast, "Direct and simultaneous observation of ultrafast electron and hole dynamics in germanium," *Nat. Commun.,* 8, 1-11, (2017).
[165] S. K. Cushing, M. Zürch, P. M. Kraus, L. M. Carneiro, A. Lee, H.-T. Chang, C. J. Kaplan, and S. R. Leone, "Hot phonon and carrier relaxation in Si (100) determined by transient extreme ultraviolet spectroscopy," *Struct. Dyn.,* 5, 054302, (2018).
[166] M. Volkov, S. A. Sato, F. Schlaepfer, L. Kasmi, N. Hartmann, M. Lucchini, L. Gallmann, A. Rubio, and U. Keller, "Attosecond screening dynamics mediated by electron localization in transition metals," *Nat. Phys.,* 15, 1145-9, (2019).
[167] N. Sadegh, M. van der Geest, J. Haitjema, F. Campi, S. Castellanos, P. M. Kraus, and A. M. Brouwer, "XUV induced bleaching of a tin oxo cage photoresist studied by high harmonic absorption spectroscopy," *J. Photopolym. Sci.Technol.,* 33, 145-51, (2020).
[168] L. Van Lokeren, R. Willem, D. Van Der Beek, P. Davidson, G. A. Morris, and F. Ribot, "Probing the anions mediated associative behavior of tin-12 oxo-macrocations by pulsed field gradient NMR spectroscopy," *J. Phys. Chem. C,* 114, 16087-91, (2010).
[169] J. A. Bearden, and A. Burr, "Reevaluation of X-ray atomic energy levels," *Reviews of Modern Physics,* 39, 125, (1967).
[170] M. Cardona, and L. Ley, *Photoemission in solids I*, (1978).

[171] J. C. Fuggle, and N. Mårtensson, “Core-level binding energies in metals,” *J. Electron Spectrosc. Relat. Phenom.,* 21, 275-81, (1980).

[172] D. Dakternieks, H. Zhu, E. R. Tiekink, and R. Colton, “Synthesis, structure and reactions of $[(BuSn)_{12}O_{14}(OH)_6]Cl_2{\cdot}2H_2O$: Solution studies using ^{119}Sn NMR and electrospray mass spectrometry,” *J. Organomet. Chem.,* 476, 33-40, (1994).

[173] C. Eychenne-Baron, F. Ribot, and C. Sanchez, “New synthesis of the nanobuilding block $\{(BuSn)_{12}O_{14}(OH)_6\}^{2+}$ and exchange properties of $\{(BuSn)_{12}O_{14}(OH)_6\}(O_3SC_6H_4CH_3)_2$,” *J. Organomet. Chem.,* 567, 137-42, (1998).

[174] C. L. Henderson, S. Pancholi, S. A. Chowdhury, C. G. Willson, and R. R. Dammel, “Photoresist characterization for lithography simulation: II. Exposure parameter measurements,” *Proc. SPIE*, 3049, 816-28, (1997).

[175] A. Sekiguchi, Y. Matsumoto, T. Harada, T. Watanabe, and H. Kinoshita, “Study of Dill's B parameter measurement of EUV resist,” *Proc. SPIE*, 9422, 781-94, (2015).

[176] J. Haitjema, *Exciting tin-oxo cages: Light-induced chemistry for nanopatterning*, (2020).

[177] O. Kitamura, S. Terakado, S. Suzuki, M. Nakao, T. Sekitani, and K. Tanaka, “Synchrotron-radiation-excited etching and total electron yield measurement of silicon and silicon nitride,” *J. Vac. Sci. Technol,* 13, 2451-5, (1995).

[178] A. Pirati, R. Peeters, D. Smith, S. Lok, M. van Noordenburg, R. van Es, E. Verhoeven, H. Meijer, A. Minnaert, and J.-W. van der Horst, “EUV lithography performance for manufacturing: status and outlook,” *Proc. SPIE*, 9776, 97760A, (2016).

[179] C. Wagner, J. Bacelar, N. Harned, E. Loopstra, S. Hendriks, I. De Jong, P. Kuerz, L. Levasier, M. van de Kerkhof, and M. Lowisch, “EUV lithography at chipmakers has started: performance validation of ASML's NXE: 3100,” *Proc. SPIE*, 7969, 499-510, (2011).

[180] A. Yen, H. Meiling, and J. Benschop, “Enabling manufacturing of sub-10nm generations of integrated circuits with EUV lithography,” *IEEE, EDTM*, 475-7, (2019).

[181] H. Xu, V. Kosma, K. Sakai, E. P. Giannelis, and C. K. Ober, “EUV photolithography: resist progress in metal–organic complex photoresists,” *J. Micro/Nanolith. MEMS MOEMS,* 18, 011007, (2018).

[182] J. Stowers, J. Anderson, B. Cardineau, B. Clark, P. De Schepper, J. Edson, M. Greer, K. Jiang, M. Kocsis, and S. Meyers, “Metal oxide EUV photoresist performance for N7 relevant patterns and processes,” *Proc. SPIE*, 9779, 977904, (2016).

[183] D. De Simone, I. Pollentier, and G. Vandenberghe, “Metal-containing materials as turning point of EUV lithography,” *J. Photopolym. Sci.Technol.,* 28, 507-14, (2015).

[184] W. D. Hinsberg, F. A. Houle, M. I. Sanchez, and G. M. Wallraff, “Chemical and physical aspects of the post-exposure baking process used for positive-tone chemically amplified resists,” *IBM J Res Dev,* 45, 667-82, (2001).

[185] Y. Wei, and R. L. Brainard, *Advanced processes for 193-nm immersion lithography*: SPIE press, (2009).

[186] J. Torok, R. Del Re, H. Herbol, S. Das, I. Bocharova, A. Paolucci, L. E. Ocola, C. Ventrice Jr, E. Lifshin, and G. Denbeaux, “Secondary electrons in EUV lithography,” *J. Photopolym. Sci.Technol.,* 26, 625-34, (2013).

[187] R. L. Brainard, G. G. Barclay, E. H. Anderson, and L. E. Ocola, “Resists for next generation lithography,” *Microelectron. Eng.,* 61, 707-15, (2002).

[188] A. Narasimhan, S. Grzeskowiak, B. Srivats, H. C. Herbol, L. Wisehart, C. Kelly, W. Earley, L. E. Ocola, M. Neisser, and G. Denbeaux, “Studying secondary electron behavior in EUV resists using experimentation and modeling,” *Proc. SPIE*, 9422, 942208, (2015).

[189] I. Pollentier, Y. Vesters, J. Jiang, P. Vanelderen, and D. de Simone, "Unraveling the role of secondary electrons upon their interaction with photoresist during EUV exposure," *Proc. SPIE*, 10450, 104500H, (2017).
[190] A. Narasimhan, S. Grzeskowiak, C. Ackerman, T. Flynn, G. Denbeaux, and R. L. Brainard, "Mechanisms of EUV exposure: electrons and holes," *Proc. SPIE*, 10143, 195-203, (2017).
[191] D. De Simone, Y. Vesters, and G. Vandenberghe, "Photoresists in extreme ultraviolet lithography (EUVL)," *Adv. Opt. Technol,* 6, 163-72, (2017).
[192] R. Fallica, J. Haitjema, L. Wu, S. Castellanos, F. Brouwer, and Y. Ekinci, "Absorption coefficient and exposure kinetics of photoresists at EUV," *Proc. SPIE*, 10143, 101430A, (2017).
[193] J. H. Ma, C. Needham, H. Wang, A. Neureuther, D. Prendergast, and P. Naulleau, "Mechanistic Advantages of Organotin Molecular EUV Photoresists," *ACS Appl. Mater. Interfaces,* (2022).
[194] E. W. Abel, J. Labinger, J. A. Labinger, F. G. A. Stone, M. J. Winter, and G. Wilkinson, "Comprehensive organometallic chemistry II: a review of the literature 1982-1994," (1995).
[195] H. Ebel, R. Svagera, M. F. Ebel, and N. Zagler, "Total electron yield (TEY) a new approach for quantitative x-ray analysis," *Advances in X-Ray Analysis,* 38, 325-35, (1994).
[196] J. Stöhr, C. Noguera, and T. Kendelewicz, "Auger and photoelectron contributions to the electron-yield surface extended X-ray-absorption fine-structure signal," *Phys. Rev. B,* 30, 5571, (1984).
[197] S. L. Schroeder, "Towards a 'universal curve' for total electron-yield XAS," *Solid State Commun.,* 98, 405-9, (1996).
[198] M. P. Seah, and W. Dench, "Quantitative electron spectroscopy of surfaces: A standard data base for electron inelastic mean free paths in solids," *Surf. Interface Anal.,* 1, 2-11, (1979).
[199] H. Henneken, F. Scholze, and G. Ulm, "Lack of proportionality of total electron yield and soft x-ray absorption coefficient," *J. Appl. Phys.,* 87, 257-68, (2000).
[200] A. Owens, S. Bayliss, G. Fraser, and S. Gurman, "On the relationship between total electron photoyield and X-ray absorption coefficient," *Nucl. Instrum. Methods Phys. Res.,* 385, 556-8, (1997).
[201] B. L. Henke, J. Knauer, and K. Premaratne, "The characterization of x-ray photocathodes in the 0.1–10-keV photon energy region," *J. Appl. Phys.,* 52, 1509-20, (1981).
[202] A. Jablonski, and C. J. Powell, "Electron effective attenuation lengths in electron spectroscopies," *J. Alloys Compd.,* 362, 26-32, (2004).
[203] C. T. Chantler, "Theoretical form factor, attenuation, and scattering tabulation for Z= 1–92 from E= 1–10 eV to E= 0.4–1.0 MeV," *JPCRD,* 24, 71-643, (1995).
[204] J. H. Hubbell, H. Gerstenberg, and E. Saloman, *Bibliography of photon total cross section (attenuation coefficient) measurements 10 eV to 13. 5 Gev*, National Bureau of Standards, Washington, DC (USA), (1986).
[205] G. S. Henderson, F. M. De Groot, and B. J. Moulton, "X-ray absorption near-edge structure (XANES) spectroscopy," *Rev Mineral Geochem.,* 78, 75-138, (2014).
[206] B. L. Henke, E. M. Gullikson, and J. C. Davis, "X-ray interactions: photoabsorption, scattering, transmission, and reflection at E= 50-30,000 eV, Z= 1-92," *Atomic data and nuclear data tables,* 54, 181-342, (1993).
[207] J. Dahn, B. Way, E. Fuller, W. Weydanz, J. Tse, D. Klug, T. Van Buuren, and T. Tiedje, "X-ray diffraction and x-ray absorption studies of porous silicon, siloxene, heat-treated siloxene, and layered polysilane," *J. Appl. Phys.,* 75, 1946-51, (1994).
[208] R. Thomas, "Interference Effects in the Reflection of Low-Energy Electrons from Thin Films of Au on Ir," *J. Appl. Phys.,* 41, 5330-4, (1970).

[209] W. Pong, R. Sumida, and G. Moore, “Attenuation Length for Photoelectrons in Metal Films,” *J. Appl. Phys.,* 41, 1869-70, (1970).

[210] L.-L. Chua, M. Dipankar, S. Sivaramakrishnan, X. Gao, D. Qi, A. T. Wee, and P. K. Ho, “Large damage threshold and small electron escape depth in X-ray absorption spectroscopy of a conjugated polymer thin film,” *J. Am. Chem. Soc.,* 22, 8587-94, (2006).

[211] M. Huttula, E. Kukk, S. Heinäsmäki, M. Jurvansuu, S. Fritzsche, H. Aksela, and S. Aksela, “Effects of the open-shell electronic structure in 4 d photoionization and Auger decay of atomic Sn,” *Phys. Rev. A,* 69, 012702, (2004).

[212] J. H. Ma, H. Wang, D. Prendergast, A. Neureuther, and P. Naulleau, “Excitation selectivity in model tin-oxo resist: a computational chemistry perspective,” *Proc. SPIE*, 11323, 113231F, (2020).

[213] W. D. Hinsberg, and S. Meyers, “A numeric model for the imaging mechanism of metal oxide EUV resists,” *Proc. SPIE*, 10146, 1014604, (2017).

[214] J. Haitjema, “Exciting tin-oxo cages: Light-induced chemistry for nanopatterning,” PhD Thesis, University of Amsterdam, (2020).

[215] I. Pollentier, Y. Vesters, J. S. Petersen, P. Vanelderen, A. Rathore, D. De Simone, and G. Vandenberghe, “Unraveling the role of photons and electrons upon their chemical interaction with photoresist during EUV exposure,” *Proc. SPIE*, 10586, 105860C, (2018).

[216] S. Graham Jr, C. A. Steinhaus, W. M. Clift, L. E. Klebanoff, and S. Bajt, “Atomic hydrogen cleaning of EUV multilayer optics,” *Proc. SPIE*, 5037, 460-9, (2003).

[217] H. Oizumi, H. Yamanashi, I. Nishiyama, K. Hashimoto, S. Ohsono, A. Masuda, A. Izumi, and H. Matsumura, “Contamination removal from EUV multilayer using atomic hydrogen generated by heated catalyzer,” *Proc. SPIE*, 5751, 1147-54, (2005).

[218] E. Shiobara, Y. Kikuchi, S. Mikami, T. Sasami, T. Kamizono, S. Minegishi, T. Kimoto, T. Fujimori, T. Watanabe, and T. Harada, “EUV resist outgassing analysis for the new platform resists at EIDEC,” *Proc. SPIE*, 9776, 674-85, (2016).

[219] I. Pollentier, “Study of EUV Resist Outgassing/Contamination for device integration using EUVL processes,” *J. Photopolym. Sci.Technol.,* 23, 605-12, (2010).

[220] I. Pollentier, A. T. Venkata, and R. Gronheid, “Relationship between resist outgassing and EUV witness sample contamination in NXE outgas qualification using electrons and EUV photons,” *Proc. SPIE*, 9048, 90481B, (2014).

[221] G. Denbeaux, R. Garg, J. Waterman, C. Mbanaso, J. Netten, R. Brainard, Y.-J. Fan, L. Yankulin, A. Antohe, and K. DeMarco, “Quantitative measurement of EUV resist outgassing,” *23rd European Mask and Lithography Conference*, 1-5, (2007).

[222] I. Pollentier, I. Neira, and R. Gronheid, “Assessment of resist outgassing related EUV optics contamination for CAR and non-CAR material chemistries,” *Proc. SPIE*, 7972, 73-84, (2011).

[223] I. Pollentier, M. Berger, R. Gronheid, A. Goethals, and M. Leeson, “Characterization of EUV resist related outgassing and contamination,” *EUVL Symposium Prague*, (2009).

[224] A. Balzers, “Partial pressure measurement in vacuum technology,” *Balzers Instruments, FL-9496 Balzers, Liechtenstein,* (1983).

[225] P. Vacuum, "Vacuum technology know how," Pfeiffer Vacuum GmbH, (2009).

[226] P. Linstorm, “NIST chemistry webbook, NIST standard reference database number 69,” *J. Phys. Chem. Ref. Data, Monograph,* 9, 1-1951, (1998).

[227] C. Mack, *Fundamental Principles of Optical Lithography: The Science of Microfabrication*: John Wiley & Sons, (2007).

[228] N. Kenane, and D. A. Keszler, "High-Resolution Lithographic Patterning with Organotin Films: Role of CO2 in Differential Dissolution Rates," *ACS Appl. Mater. Interfaces,* 13, 18974-83, (2021).

[229] F. Banse, F. Ribot, P. Tolédano, J. Maquet, and C. Sanchez, "Hydrolysis of monobutyltin trialkoxides: Synthesis and characterizations of $\{(BuSn)_{12}O_{14}(OH)_6\}(OH)_2$," *Inorg. Chem.,* 34, 6371-9, (1995).

[230] Y. Zhang, "Organotin photoresists for extreme ultraviolet lithography," PhD Thesis, University of Amsterdam, Chapter 7, (2019).

Summary

The main objective of this thesis is to gain a better understanding of the photon-driven reactions in organotin molecular compounds which are considered promising photoresists for Extreme UltraViolet (EUV) photolithography. EUV technology is state-of-the-art in the manufacturing of integrated circuits because it allows for printing sub-20-nm features on semiconductor substrates in a single exposure. The pattern is transferred onto the substrate through the photoinduced solubility switch of the photoresist material, demanding an adequate understanding of these reactions for the resist's performance optimization. In our studies, we focus on tin-oxo cages as a prototype of the tin-based molecular compounds. The dense structure of the molecular cage, with 12 tin atoms and 22 oxygens, turns the tin-oxo cage compounds into strong photon absorbers at the EUV energy of 92 eV. The 12 tin atoms of the cage are linked to butyl groups via Sn-C bonds and their cleavage upon exposure plays the primary role in the solubility switch of the resist.

In the experimental research described in this thesis, we used different spectroscopic techniques to investigate the photoconversion of the resist and the rates of reactions induced by different exposure wavelengths, including 13.5 nm (92 eV).

Chapter 1 gives an overview of the photolithography technique and the challenges on the development track toward EUV lithography. We describe some efforts so far on developing new generations of the resist that could meet the EUV patterning requirements, such as high sensitivity for EUV radiation, and it is explained why organotin-based molecular compounds are among the most interesting types of EUV photoresists. Building and developing a source of broadband XUV photons based on higher-harmonic generation from a near-infrared femtosecond laser was an important goal of our project. Hence, Chapter 1 contains a short introduction to the principle of high harmonic generation and phase-matching conditions for optimizing the generation efficiency.

In Chapter 2, we describe the experimental setups and methodology used to investigate the resist's photoreactivity and the main approaches utilized for data analysis. The HHG setup built in our laboratory is described in detail. Total Electron Yield (TEY) and X-ray Photoelectron Spectroscopy are introduced

as the other two main spectroscopic techniques used to gain insight into the resist's reactivity, performed at the Elettra synchrotron in Trieste, Italy. Finally, we present the ellipsometry procedure for the measurement of the resist film thickness.

Chapter 3 presents the results of XUV broadband absorption spectroscopy performed on TinOH (tin-oxo cage with hydroxide counterions) using the homemade HHG setup. The resist was exposed to high harmonics generated from Ar, with a broad incident energy of 25 – 40 eV, and the induced photobleaching (changes in the absorption spectra) of the resist was studied. The bleaching decreases continuously with exposure until it saturates, which was assigned to the photon-induced outgassing of butyl groups (and water) with the estimation of ~60% dissociation of butyl groups in our measurement. A good agreement was found between the obtained absorption cross-sections and the predicted values from the CXRO database.

In Chapter 4, we report the results of XUV broadband absorption spectroscopy on TinOAc resist, with extended exposure energy up to 70 eV after further development of the HHG setup. The high harmonics with energies of 21 – 41 and 41 – 70 eV from argon and neon were used as the exposure source. The induced photobleaching of the resist decreases with increasing photon energy due to the cleavage of butyl groups which absorb the most at lower energies. We found a good agreement between the absorption spectrum of the resist with the predicted one from the CXRO database over the 21 – 70 eV energy range. The changes in the optical absorption of the resist with exposure dose show that complete conversion of the resist to tin oxide does not occur, and it ends up on a plateau after a rapid decay at the initial exposure. This observation matches the decreasing outgassing rate reported in Chapter 6 for 92 eV irradiation. We estimate that ~70% and 55% of the butyl groups are cleaved by the end of the exposure using photon energies of 21 – 40 eV and 40 – 70 eV, respectively.

Chapter 5 presents the result of XPS and TEY measurements on tin-oxo cages. We recorded the XPS spectra of the electrons emitted from the Sn(4d) orbitals at selected photon energies from 50 to 135 eV. The detected electron count follows the predicted ionization cross-section values and gradually decreases for exposure energies above 60 eV. We measured TEY spectra for the three tin-oxo cage derivatives: TinOH, TinOAc and TinB, in the XUV range of 5 to 150 eV. All show an ionization onset at 8 eV, and the spectra are similar over the whole energy range. We estimate that 3.5 – 4 electrons are generated per absorbed EUV photon, based on a simple linear relation between TEY yield and the product of the absorption coefficient and photon energy. Considering that 20 – 30 eV is the typical maximum in the

Electron Energy Loss function for most materials, we can expect the emission of at most 4 electrons following one EUV photon absorption.

In chapter 6, we investigated the photoinduced conversion of TinOH under EUV exposure using ellipsometry and outgassing (residual gas analysis) measurements. A mass spectrum of the outgassing mixture was measured while exposing the resist to the EUV beam. Four major outgassing molecules were identified: butene, butane, octane and CO_2, with ratios of approximately 0.3, 0.25, 0.11 and 0.046 to the total detected mass, and we suggested reaction mechanisms that could lead to their formation. There was no indication of outgassing of tin-containing molecular ions. The outgassing rate of butane, octane, CO_2, and hydrogen was monitored as a function of exposure dose. The outgassing rate showed a rapid decay at early exposure reaching 50% of its initial value after a dose of 25 mJ cm^{-2}. The induced thickness change after exposure and after development was measured using ellipsometry. The obtained contrast curve of the resist shows that the material is completely washed away at doses below 9 mJ cm^{-2} and reaches its maximum retained thickness at 45 mJ cm^{-2}. Relating the exposure induced thickness change with the resist's conversion gives us 14.5% butyl dissociation as the minimum required value for the full solubility switch of the resist, which means ~1.7 Sn-C bond cleavage per molecule and a quantum yield of ~3 bond dissociations per absorbed photon.

Samenvatting

Het hoofddoel van dit proefschrift is een beter begrip te krijgen van de chemische reacties in moleculaire organotinverbindingen die worden beschouwd als veelbelovende fotoresisten voor Extreem UltraViolet (EUV) fotolithografie. EUV-technologie is de *state-of-the-art* in de fabricage van geïntegreerde schakelingen omdat hiermee in één enkele belichting structuren kleiner dan 20 nm op halfgeleidersubstraten kunnen worden geprint. Een lichtpatroon wordt op het substraat overgebracht door de verandering van de oplosbaarheid van het fotolakmateriaal die een gevolg is van chemische veranderingen onder invloed van het EUV licht. Om de werking van de fotoresist te verbeteren is het belangrijk om deze reacties te kennen en te begrijpen. In onze studies richten wij ons op tin-oxokooien als prototype van op tin gebaseerde moleculaire fotoresistverbindingen. De 12 tinatomen zorgen ervoor dat de tin-oxokooien de EUV-energie van 92 eV goed absorberen. Elk van de 12 tinatomen van de kooi is verbonden met een butylgroep. De splitsing van de tin-koolstofbindingen bij belichting is de eerste stap in de oplosbaarheidsverandering van de fotoresist, wat uiteindelijk leidt tot de overdracht van het lichtpatroon als een masker op het substraat.

In het experimentele onderzoek dat in dit proefschrift wordt beschreven, hebben we verschillende spectroscopische technieken gebruikt om de fotoconversie van de tin-oxokooien en de reactiesnelheid bij verschillende belichtingsgolflengten, waaronder 13.5 nm (92 eV), te onderzoeken.

Hoofdstuk 1 geeft een overzicht van de fotolithografietechniek en de uitdagingen op het ontwikkelingspad van EUV-lithografie. We beschrijven enkele inspanningen tot nu toe om nieuwe generaties van fotolakken te ontwikkelen die kunnen voldoen aan de vereisten voor EUV-patroonvorming, zoals een hoge gevoeligheid voor EUV-straling. De belangrijkste verschillen tussen conventionele diep-ultraviolet materialen op basis van organische polymeren en metaalhoudende fotoresisten worden kort besproken, waarbij moleculaire verbindingen op basis van tin worden beschreven als een van de meest interessante soorten EUV-fotoresisten.

Het ontwikkelen van een bron van breedbandige XUV-fotonen op basis van hogere-harmonische generatie van een nabij-infrarode femtoseconde laser was een belangrijk doel van ons project. Daarom

bevat hoofdstuk 1 een korte inleiding in het principe van hogere harmonische generatie vanuit de semi-klassieke beschrijving op atomair niveau en *phase matching* voorwaarden voor het optimaliseren van de efficiëntie op macroscopische schaal.

In hoofdstuk 2 beschrijven we de experimentele opstellingen en methodologie die zijn gebruikt om de reactiviteit van de fotoresist te onderzoeken. De in ons laboratorium gebouwde HHG-opstelling wordt in detail beschreven. *Total Electron Yield* (TEY) en *X-ray Photoelectron Spectroscopy* (XPS) worden geïntroduceerd als de andere twee belangrijke spectroscopische technieken die zijn gebruikt om inzicht te krijgen in de reactiviteit van de tin-oxokooien. Ten slotte beschrijven we de ellipsometrieprocedure die is gebruikt om de dikte van de film van de resist te meten.

Hoofdstuk 3 beschrijft de resultaten van XUV breedband-absorptiespectroscopie uitgevoerd op dunne lagen van TinOH (tin-oxo kooi met hydroxide tegenionen) met behulp van de zelfgebouwde HHG opstelling. De fotoresist werd blootgesteld aan hogere harmonischen gegenereerd met behulp van argon, met een breed energiespectrum van 25 tot 40 eV, en de veranderingen in de absorptiespectra van de resistfilm werden bestudeerd. De absorptie neemt geleidelijk af gedurende de blootstelling maar de veranderingen worden steeds kleiner naarmate de tijd voorschrijdt. De veranderingen in de absorptie werden toegeschreven aan het verlies van de organische butylgroepen (en water). We schatten dat ongeveer 60% van alle butylgroepen tijdens de blootstelling wordt afgesplitst door de eerste en de laatst gemeten absorptiespectra te vergelijken met het theoretische absorptiespectrum van $Sn_{12}O_{18}$ als het uiteindelijke hypothetische product. De verkregen absorptiedoorsneden (α) bleken goed overeen te komen met de voorspelde waarden uit de CXRO-databank.

In hoofdstuk 4 presenteren we de resultaten van XUV-breedbandabsorptiespectroscopie aan TinOAc. Deze tin-oxokooi met acetaat-tegenionen biedt een betere chemische stabiliteit dan TinOH. Het energiebereik van het licht werd uitgebreid na verdere ontwikkeling van de HHG-opstelling. De hogere harmonischen met energieën van 21 tot 41 en 41 tot 70 eV met respectievelijk argon en neon als HHG-opwekkend gasmedium werden gebruikt als belichtingsbron. De afname van de absorptie werd gevolgd gedurende de belichting, en we constateerden dat de mate van afname aan het eind van de belichtingsperiode kleiner is bij hogere fotonenergie. Het fotobleken neemt af met toenemende fotonenergie omdat het wordt veroorzaakt door de splitsing van butylgroepen die het meest absorberen bij lagere energieën. Wij vonden een goede overeenkomst tussen het absorptiespectrum van de fotoresist en het voorspelde spectrum van de CXRO-database over het gehele energiebereik van 21 tot 70 eV. De

veranderingen in de optische absorptie met de lichtdosis laten zien dat een volledige omzetting van de fotoresist tot anorganische tinoxides niet plaatsvindt, en dat deze eindigt op een plateau na een snel verval na de eerste blootstelling. Deze waarneming komt overeen met de in hoofdstuk 6 gerapporteerde afnemende snelheid van de vorming van gasvormige fotoprodukten bij 92 eV. Wij schatten dat ~70% en 55% van de butylgroepen aan het eind van de blootstelling zijn afgesplitst bij fotonenergieën van respectievelijk 21 tot 40 eV en 40 tot 70 eV.

Hoofdstuk 5 presenteert de resultaten van XPS- en TEY-metingen aan verschillende tin-oxokooien. We hebben de XPS spectra gemeten van de elektronen afkomstig uit Sn(4d) orbitalen bij geselecteerde fotonenergieën van 50 tot 135 eV. Het aantal gedetecteerde elektronen volgt de voorspelde waarden van de ionisatiedoorsnede en neemt geleidelijk af voor belichtingsenergieën boven 60 eV. TEY-spectra in het XUV-bereik van 5 tot 150 eV zijn gemeten van drie tin-oxo kooiderivaten. De spectra van de drie verbindingen verschillen nauwelijks, en laten zien dat in alle gevallen fotoionisatie plaatsvindt bij een energie van 8 eV en hoger. We schatten dat 3,5 tot 4 elektronen worden gegenereerd per geabsorbeerd EUV-foton, uitgaande van een eenvoudige lineaire relatie tussen de TEY-opbrengst en het product van de absorptiecoëfficiënt en de fotonenergie. Helaas beschikken wij ten tijde van dit project niet over de *Electron Energy Loss Functions* (ELF) voor de tin-oxokooien die nodig zijn voor meer kwantitatieve modellering van de waarnemingen. Als we echter uitgaan van 20 tot 30 eV als de typische maximale ELF-waarde voor de meeste materialen, kunnen we de emissie van maximaal 4 elektronen verwachten na één EUV-fotonabsorptie.

In hoofdstuk 6 onderzochten we de foto-geïnduceerde omzetting van TinOH onder EUV-blootstelling met behulp van ellipsometrie en restgasanalyse (*outgassing*) metingen. Een massaspectrum van de vrijkomende moleculen werd gemeten terwijl de resistlaag werd blootgesteld aan de EUV-bundel. Door de gemeten massaspectra te vergelijken met die uit de NIST-database, identificeerden wij de belangrijkste vluchtige reactieproducten: 1-buteen, butaan, octaan en CO_2, met verhoudingen van ongeveer 0,3, 0,25, 0,11 en 0,046 tot de totale gedetecteerde massa's. We stellen enkele reactiemechanismen voor die tot hun vorming zouden kunnen leiden. In de opgenomen spectra waren geen aanwijzingen voor het uitgassen van tin-bevattende moleculen. De uitgassnelheid van butaan, octaan, CO_2 en waterstof werd selectief gevolgd met de toename van de blootstellingsdosis. De uitgassnelheid neemt snel af van zijn beginwaarde tot ongeveer 50% daarvan na blootstelling aan de eerste 25 mJ cm^{-2}. De dikteverandering van de film na bestraling met EUV en na ontwikkeling werd gemeten met behulp van ellipsometrie. Zo verkregen we de contrastcurve van de fotoresist, waaruit blijkt dat het belichte materiaal nog volledig wordt weggespoeld

bij doses beneden 9 mJ cm^{-2} en dat het zijn maximale behouden dikte bereikt bij 45 mJ cm^{-2}. De dikteverandering bij blootstelling werd in verband gebracht met de chemische omzetting van de TinOH moleculen. Hieruit blijkt dat 14.5% dissociatie van de butylgroepen voldoende is voor het volledig onoplosbaar worden van de resists, wat neerkomt op de splitsing van ~1.7 Sn-C-binding per molecuul en een kwantumrendement van ~3 bindingsdissociaties per geabsorbeerd foton.

Publication list

1. **N. Sadegh**, M. van der Geest, J. Haitjema, F. Campi, S. Castellanos, P.M. Kraus, and A.M. Brouwer, "XUV Induced Bleaching of a Tin Oxo Cage Photoresist Studied by High Harmonic Absorption Spectroscopy", *J. Photopolym. Sci.Technol*, 33, 145-151, (2020). [Chapter 3]

2. Y. Zhang, J. Haitjema, S. Castellanos, O. Lugier, **N. Sadegh**, R. Ovsyannikov, E. Giangrisostomi, F. O. L. Johansson, E. Berggren, A. Lindblad, A. M. Brouwer, "Extreme Ultraviolet Photoemission of a Tin-based Photoresist", *Appl. Phys. Lett*, 118, 171903, (2021).

3. M. van der Geest, **N. Sadegh**, T.M. Meerwijk, E.I. Wooning, L. Wu, R. Bloem, S. Castellanos Ortega, A.M. Brouwer, and P.M. Kraus, "Extreme-Ultraviolet Exciting Time- and Frequency-resolved Luminescence Spectroscopy Using an Ultrafast Table-Top High-harmonic-generation Source", *Rev. Sci. Instrum*, 92, 113004, (2021).

4. Q.Evrard, **N.Sadegh**, Y. Ekinci, M.Vockenhuber, N.Mahne, A.Giglia, S.Nannarone, T.Goya, T.Sugioka, and A.M. Brouwer, "Influence of counteranions on the performance of tin-based EUV photoresist", *J. Photopolym. Sci.Technol*, 35, 95-100, (2022).

5. Q. Evrard, **N. Sadegh**, C. C. Hsu, N. Mahne, A. Giglia, S. Nannarone, Y. Ekinci, M. Vockenhuber, A. Nishimura, T. Goya, T. Sugioka, and A. M. Brouwer, "Influence of the anion in tin-based EUV photoresists properties ", *Proc. SPIE*, 12498, 164-169 (2023).

6. **N. Sadegh**, Q. Evrard, N. Mahne, A. Giglia, S. Nannarone, A. M. Brouwer, "Electron Generation in Tin-oxo Cage Extreme Ultraviolet Photoresists", *J. Photopolym. Sci.Technol*, 36, 373-378, (2023). [Chapter 5]

Acknowledgement

I want to express my gratitude to all the individuals who helped and supported me throughout this research; without their help, it would have been impossible.

First, I would like to thank my supervisor, Prof. Fred Brouwer, whose support and guidance (specifically in Nanochemistry) have been invaluable throughout my research journey. Beyond being a supervisor, I believe you are a great teacher who always cherishes sharing your extensive knowledge and expertise with your students. I genuinely appreciate your commitment to education. You accompanied us in many synchrotron measurements to provide technical expertise and mentally support us in conducting lengthy measurements. Although my PhD contract was over, I sought your guidance in shaping my next career, and you scheduled a meeting the very next day despite your busy schedule.

I want to extend my gratitude to my co-supervisor, dr. Peter Kraus, for granting me the opportunity to work with his team. This collaboration was crucial in accomplishing the optical metrology aspects of my PhD project. I am grateful for your invaluable support throughout this journey. You often joined us in the lab, sharing your experiences and guiding us in solving experimental challenges. I was consistently amazed by the depth of your passion for your field of expertise, which was evident from the joy on your face when discussing topics related to Attosecond Physics. Your enthusiasm has been inspiring not only for me but for the entire team.

Working on the intricate chemistry of tin-oxo cages and photoresists was only possible with the aid of my colleagues in the Nanophotochemistry team. I appreciate their support while learning the complexities of working with cleanroom facilities. I am grateful to dr.Quentin Ervard for his assistance in preparing the samples for synchrotron measurements and for answering with any inquiries regarding AFM measurements. We performed many synchrotron measurements together, as accomplishing them individually would have been impossible.

I would like to express my appreciation to my colleagues in the HHG team who have been with me throughout this journey, especially dr.Filippo Campi, the team's postdoc for sharing his experience and expertise in building the HHG line.

During my research study, I had the privilege of being a member of the ELENA network, which focused on studying low-energy electrons, specifically for EUV lithography and FEBID applications. This network not only offered engaging technical training but also provided valuable opportunities for the development of soft skills. I am grateful for Prof. Oddur Ingólfsson's dedication to managing the network and his relentless efforts to transform it into an excellent platform for our professional development and training.

I performed multiple measurements at the BEAR beamline in Trieste, Italy. I want to thank the scientists at the BEAR beamline: prof. Stefano Nannarone, Nicola Mahne, dr.Angelo Giglia, for their collaboration and support throughout the process. During the pandemic, they provided a platform for remote measurements, enabling us to continue our research and overcome the challenges posed by pandemic restrictions.

As part of the ELENA project, I completed a 5-month internship in the nanopatterning department of Imec, where I had the opportunity to conduct outgassing measurements and utilize advanced cleanroom equipment. I would like to express my gratitude to the team at Imec for welcoming me into their department. In particular, I extend my thanks to Ivan Pollentier for his assistance in conducting the outgassing measurements and addressing my inquiries.

I would also like to express my gratitude to the committee board for accepting my invitation and dedicating their time to review the manuscript.

Lastly, I am thankful to dr. Nataliia Kuzkova and Feng-Chun Hsia for agreeing to be my paranymphs.